A global apparent polar wander path for the last 320 Ma calculated from site-level paleomagnetic data

Bram Vaes [a,*], Douwe J.J. van Hinsbergen [a], Suzanna H.A. van de Lagemaat [a], Erik van der Wiel [a], Nalan Lom [a], Eldert L. Advokaat [a,b], Lydian M. Boschman [a], Leandro C. Gallo [c], Annika Greve [a], Carl Guilmette [d], Shihu Li [e], Peter C. Lippert [f], Leny Montheil [g], Abdul Qayyum [a], Cor G. Langereis [a]

[a] Department of Earth Sciences, Faculty of Geosciences, Utrecht University, Utrecht, the Netherlands
[b] School of Geography, Earth and Environmental Sciences, University of Birmingham, United Kingdom
[c] Centre for Earth Evolution and Dynamics (CEED), University of Oslo, Oslo, Norway
[d] Géologie et Génie Géologique, Université Laval, Québec City, Quebec, Canada
[e] State Key Laboratory of Lithospheric Evolution, Institute of Geology and Geophysics, Chinese Academy of Sciences, Beijing, 100029, China
[f] Department of Geology and Geophysics, University of Utah, Salt Lake City, United States of America
[g] Géosciences Montpellier, CNRS-Université de Montpellier-Université des Antilles, F-34095 Montpellier, France

ARTICLE INFO

ABSTRACT

Apparent polar wander paths (APWPs) calculated from paleomagnetic data describe the motion of tectonic plates relative to the Earth's rotation axis through geological time, providing a quantitative paleogeographic framework for studying the evolution of Earth's interior, surface, and atmosphere. Previous APWPs were typically calculated from collections of paleomagnetic poles, with each pole computed from collections of paleomagnetic sites, and each site representing a spot reading of the paleomagnetic field. It was recently shown that the choice of how sites are distributed over poles strongly determines the confidence region around APWPs and possibly the APWP itself, and that the number of paleomagnetic data used to compute a single paleomagnetic pole varies widely and is essentially arbitrary. Here, we use a recently proposed method to overcome this problem and provide a new global APWP for the last 320 million years that is calculated from simulated site-level paleomagnetic data instead of from paleopoles, in which spatial and temporal uncertainties of the original datasets are incorporated. We provide an updated global paleomagnetic database scrutinized against quantitative, stringent quality criteria, and use an updated global plate motion model. The new global APWP follows the same trend as the most recent pole-based APWP but has smaller uncertainties. This demonstrates that the first-order geometry of the global APWP is robust and reproducible. Moreover, we find that previously identified peaks in APW rate disappear when calculating the APWP from site-level data and correcting for a temporal bias in the underlying data. Finally, we show that a higher-resolution global APWP frame may be determined for time intervals with high data density, but that this is not yet feasible for the entire 320–0 Ma time span. Calculating polar wander from site-level data provides opportunities to significantly improve the quality and resolution of the global APWP by collecting large and well-dated paleomagnetic datasets from stable plate interiors, which may contribute to solving detailed Earth scientific problems that rely on a paleomagnetic reference frame.

1. Introduction

Paleomagnetism provides one of the principal tools for the quantitative reconstruction of Earth's paleogeography. Paleomagnetic data are used to construct apparent polar wander paths (APWPs) that describe the apparent motion of the paleomagnetic pole relative to a fixed continent or tectonic plate through time (e.g., Creer et al., 1954). Assuming that the time-averaged geomagnetic pole coincides with the Earth's spin axis allows the translation of an APWP into the motion of a continent or plate relative to the geographic pole. By rotating

paleomagnetic data from all major plates to a common reference plate using independent constraints on relative plate motions, a global APWP may be constructed that places a global model of relative plate motions into an 'absolute' reference frame (e.g., Phillips and Forsyth, 1972; Besse and Courtillot, 1991, 2002; Torsvik et al., 2008, 2012). Such a paleomagnetic reference frame is widely used by paleomagnetists to determine relative paleolatitudinal motions or vertical-axis rotations (e.g., Demarest, 1983; Butler, 1992) and also allows the estimation of the paleolatitude (through time) of any given location on Earth (e.g., van Hinsbergen et al., 2015), providing key input for paleoclimate, paleoenvironment, and paleobiology interpretation. These applications rely on the quality of the underlying global APWP and the robust quantification of its confidence limits. However, there is increasing recognition that the standard pole-based approach used to calculate widely used (global) APWPs and their uncertainty, which has changed little over the last >60 years, has several shortcomings.

First, the paleomagnetic poles (or paleopoles) that are used as input for APWP construction are commonly assigned equal weight, regardless of the uncertainties in the position of the paleopole or in the age of the rocks from which they were derived. Second, such paleopoles are calculated from widely different, and essentially arbitrary numbers of paleomagnetic sites (Vaes et al., 2022), whereby each site is interpreted to represent a 'spot reading' of the past geomagnetic field (e.g., McElhinny and McFadden, 2000). In previous APWPs, each input paleopole was assumed to have averaged 'out' the paleosecular variation (PSV) of the geomagnetic field, but Vaes et al. (2022) showed that the dispersion of input paleopoles around the most recent global APWP becomes larger with a smaller number of sites, creating a bias towards poles based on smaller datasets with larger uncertainty. Thus, the classical approach allows the calculation of non-unique APWPs with different uncertainties using the same underlying data depending on the subjective choice of how to distribute data over paleopoles (Vaes et al., 2022).

To overcome these problems, APWPs may instead be computed from site-level paleomagnetic data, that is, from virtual geomagnetic poles (VGPs) (e.g., McElhinny et al., 1974; Hansma and Tohver, 2020; van Hinsbergen et al., 2017; Vaes et al., 2022; Gallo et al., 2023), or by weighting paleopoles against the number of sites (McFadden and McElhinny, 1995). In these approaches, equal weight is assigned to each 'spot reading' of the past geomagnetic field (that is, a site) rather than to each paleopole based on some collection of site-level data (Fig. 1). However, building a database with site-level data for the many hundreds of studies that reported relevant input data is not straightforward as paleomagnetic data is not always reported at the site-level, particularly in older publications, and it would require an enormous effort to compile those that are only listed in the original publication and not in databases such as MagIC (Jarboe et al., 2012). While an ultimate goal would be to use actual site-level data, Vaes et al. (2022) recently introduced an alternative approach: they showed that when site-level data are parametrically re-sampled from a collection of reported paleopoles and their statistical parameters, a distribution of simulated VGPs may be obtained that provides an accurate approximation of the original data. This approach thus provides a promising avenue to use published paleomagnetic poles to compute APWPs from site-level data, allowing the incorporation of key uncertainties in the construction of APWPs as well as the weighting of datasets against the number of sites. Although recent studies have incorporated key sources of uncertainty, such as spatial and age uncertainties, in the computation of an APWP (e. g., Swanson-Hysell et al., 2019; Hansma and Tohver, 2020; Gallo et al., 2021; Wu et al., 2021; Gallo et al., 2023), this has not yet been applied to the computation of a global APWP.

In this study, we compute the first global apparent polar wander from site-level paleomagnetic data, for the last 320 Ma, in which the key uncertainties in the underlying paleomagnetic datasets, in position and age, are incorporated and weighted. To transfer paleomagnetic data to a common reference plate, we use an updated global plate circuit that includes the most recent marine geophysics-based ocean basin reconstructions. We also provide an updated paleomagnetic database that updates the compilation of Torsvik et al. (2012). We have filtered that
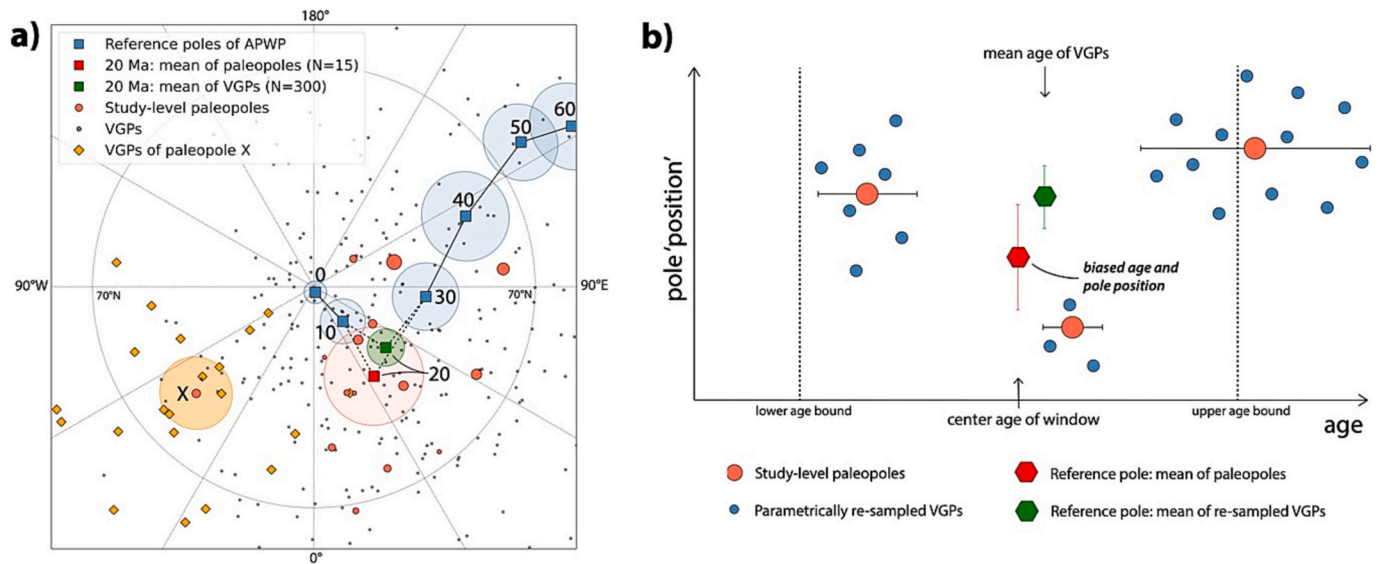

Fig. 1. a) Example of an apparent polar wander path for the last 60 Ma (blue squares, with 95% confidence regions). The 20 Ma reference pole is computed in two ways: by taking the mean of the 15 paleopoles (light red circles) – as done in the conventional approach to calculating APWPs – or by taking the mean of 300 VGPs (grey dots) that were used to calculate those paleopoles. Note the difference in the reference pole position (green versus red square) and the size of its 95% confidence region. The size of the paleopoles corresponds to the number of VGPs from which that paleopole is derived, ranging between 5 and 60. Paleopole X and the 20 VGPs from which it was calculated are highlighted in orange. **b)** Schematic comparison between the pole-based approach to calculating APWPs and the VGP-based approach developed by Vaes et al. (2022). Note that the oldest study-level paleopole does not contribute to the reference pole in the pole-based approach but that nearly half of its VGPs are used in the calculation of the reference pole in the VGP-based approach. This way, both the number of sites behind each paleopole and its spatial and temporal uncertainties are taken into account in the computation of the reference poles of an APWP. In the VGP-based approach used in this study, the mean age of the (re-sampled) VGPs is used for the reference pole, rather than the center age of the time window. (For interpretation of the references to colour in this figure legend, the reader is referred to the web version of this article.)

database using stringent, statistics-based, quantitative quality criteria and have extended the database with new, high-quality paleomagnetic datasets from stable plate interiors that have been published in the last decade. We also compiled data from regions that were previously not incorporated, such as the China Blocks, Iberia, and the Antarctic Peninsula, for the time period during which their motions relative to major tectonic plates are determined independently of paleomagnetism. We compute a global APWP from parametrically re-sampled VGPs at a 10 Ma resolution using a 20 Ma time window. We first evaluate whether there is reason to suspect that the obtained distributions of simulated VGPs are affected by biases in the underlying data (e.g., due to overlooked tectonic rotations or plate reconstruction errors). Next, we compare the new APWP with previous global APWPs that were based on paleopoles and highlight differences between them. In addition, we evaluate how the geometry of the new global APWP, and the rates of apparent polar wander, are influenced by the chosen temporal resolution of the path. Finally, we provide an outlook for the future construction of APWPs and highlight opportunities for improving the quality and resolution of the paleomagnetic reference frame.

2. Background

2.1. History of APWP computation

The paleogeographic and tectonic applications of paleomagnetism rely on the key assumption that the Earth's time-averaged magnetic field closely resembles that of a geocentric axial dipole (GAD) field, such that the position of the geomagnetic pole coincides with the Earth's rotation axis (e.g., Runcorn, 1959; Butler, 1992; Johnson and McFadden, 2007). The GAD hypothesis was already applied by Hospers (1954) and Creer et al. (1954) to determine the position of the past paleomagnetic pole relative to the sampling locations of rocks from different geological periods. One of the main advantages of assuming a dipolar field structure is that it provides a simple relationship between the paleomagnetic inclination and the paleolatitude of the location from which the paleomagnetic samples are derived: the so-called dipole formula (e.g., Runcorn, 1959; Irving, 1964). Most studies that investigated the nature of the past geomagnetic field find that the Earth's magnetic field is not a perfect geocentric axial dipole, and non-dipolar contributions to the past geomagnetic field have been estimated to be on the order of up to 5% (e.g., Butler, 1992; Besse and Courtillot, 2002; Bono et al., 2020). However, the axial dipole contribution to the field is considered to be dominant, and it has now been widely accepted that the time-averaged geomagnetic field is well-approximated by a GAD field since at least mid-Carboniferous times (e.g., Butler, 1992; McElhinny and McFadden, 2000; Johnson and McFadden, 2007; Biggin et al., 2020).

The application of the GAD assumption allows the determination of the position of the geographic pole relative to a fixed plate or continent. When the position of the time-averaged paleomagnetic pole, as a proxy for the geographic pole, is plotted for different moments in the geological past, it seems to 'wander' relative to the present-day geographic pole position, as first observed by Creer et al. (1954). This 'apparent' polar wander reflects the motion of the plate or continent relative to the Earth's rotation axis, providing an 'absolute' frame of reference for past plate tectonic motions. This motion is the combined result of two processes: plate tectonic motion relative to the rotation axis and the rotation of the entire crust-mantle system relative to the rotation axis; the latter known as true polar wander (TPW, e.g., Goldreich and Toomre, 1969; Gordon and Livermore, 1987; Evans, 2003). It is important to note that while APWPs provide quantitative constraints on the paleolatitude and azimuthal orientation of tectonic and plates and continents through geological time, they do not provide any constraints on paleolongitude, due to the symmetrical structure of the assumed GAD field.

Apparent polar wander paths are constructed as a time series of paleomagnetic reference poles relative to the coordinate frame of a chosen reference plate (Fig. 1). Calculating an APWP requires a method

to compute these reference poles by combining, averaging, or fitting available paleomagnetic data derived from rocks of different ages (e.g., McElhinny and McFadden, 2000; Tauxe et al., 2010). Creer et al. (1954) constructed the first APWP by connecting a sequence of individual paleomagnetic poles derived from rocks of different geological epochs sampled on the British Isles. But with the publication of an increasing number of 'study mean' paleopoles from rocks with overlapping ages in the following decades, reference poles were calculated by averaging available paleopoles from a given geological period (e.g., Irving, 1964; Phillips and Forsyth, 1972; Van der Voo and French, 1974). Since the late 1970s, the continuous increase in the amount of data allowed the construction of APWPs at a higher resolution by averaging paleopoles that fall within a chosen time window that was shorter than (most) geological time periods using a running mean (or sliding window) (e.g., Irving, 1977, 1979; Van Alstine and De Boer, 1978; Harrison and Lindh, 1982). This approach is appealing because of its simplicity and reproducibility (e.g., Torsvik et al., 2008), and was also used to compute the most widely used global APWPs of the last two decades (Besse and Courtillot, 2002; Kent and Irving, 2010; Torsvik et al., 2008, 2012). These APWPs were calculated at a 10 Ma interval by averaging paleopoles whose mean rock age falls within a 20 Ma sliding window centered on that age. The paleomagnetic data used to compute an APWP may be derived either from a single continent, tectonic plate, or geological terrane, or from multiple continents or plates. The advent of high-resolution global plate tectonic reconstructions, based on independent geophysical constraints, enabled paleomagnetists to rotate paleomagnetic data from all the major tectonic plates and continents into a common reference plate, providing a 'global' APWP that describes the motion of all plates and geological terranes that are linked by the plate motion model relative to a fixed rotation axis (e.g., Phillips and Forsyth, 1972; Besse and Courtillot, 1991, 2002; Torsvik et al., 2008, 2012). South Africa, or the African plate, is typically used as reference plate for the computation of a global APWP (Besse and Courtillot, 2002; Torsvik et al., 2008, 2012), because it is considered to have been relatively stationary in both latitude and longitude for the last few 100 Ma, as it has been surrounded mostly by spreading ridges since the breakup of Pangea (e.g., Torsvik et al., 2008).

2.2. Shortcomings of conventional approaches, and alternatives

The conventional approach to calculating APWPs has several important limitations. First, known sources of uncertainty, such as uncertainties in the position or age of the input paleopoles, are typically not taken into account during the calculation of the APWP (Fig. 1b). In standard paleomagnetic procedures, directional uncertainties are quantified firstly at the level of individual paleomagnetic directions (often expressed as the maximum angular deviation; see e.g., Tauxe et al., 2010), secondly, at the level of individual site-mean directions (with an α_{95} confidence cone around the Fisher (1953) mean direction), and thirdly, at the level of paleomagnetic poles (with an A_{95} confidence cone around the Fisher (1953) mean of the input VGPs). However, these uncertainties are traditionally not propagated through this hierarchical framework (Heslop and Roberts, 2016, 2020). By computing an APWP from paleopoles without error propagation, it is implicitly assumed that the uncertainties and random biases in the individual paleomagnetic poles are effectively averaged 'out' by averaging up to a few dozen coeval paleopoles in the calculation of the reference poles of the APWP (e.g., Irving, 1964; Torsvik et al., 2008, 2014).

Vaes et al. (2022) showed that the assumption that paleopoles used to compute recently published (global) APWPs average 'out' PSV is invalid. In fact, the dispersion of paleopoles around an APWP increases with a decreasing number of sites underpinning each paleopole. Despite the fact that the number of VGPs that underlie each input paleopole varies substantially (Vaes et al., 2022), each input paleopole is assigned equal weight in the classical running mean approach. Hence, the position and statistical properties of pole-based APWPs may be strongly

affected by subjective choices in how data are distributed over poles. For example, site-level paleomagnetic data from multiple paleomagnetic studies of the same volcanic or sedimentary sequence may either be included in the computation of an APWP as a single paleopole (after combining the data on the site-level) or as separate entries. Hansma and Tohver (2020) explained that there is, in fact, no phenomenological basis for first averaging a certain number of VGPs to a 'study mean' pole

to average PSV, and to then average the resulting poles again in the determination of an APWP.

It is important to note that there have been many previous efforts to propagate or weight uncertainties in the computation of apparent polar wander, for instance using a weighted running mean, spherical spline or paleomagnetic Euler pole inversion (e.g., Thompson and Clark, 1981; Harrison and Lindh, 1982; Torsvik et al., 1996; Schettino and Scotese,
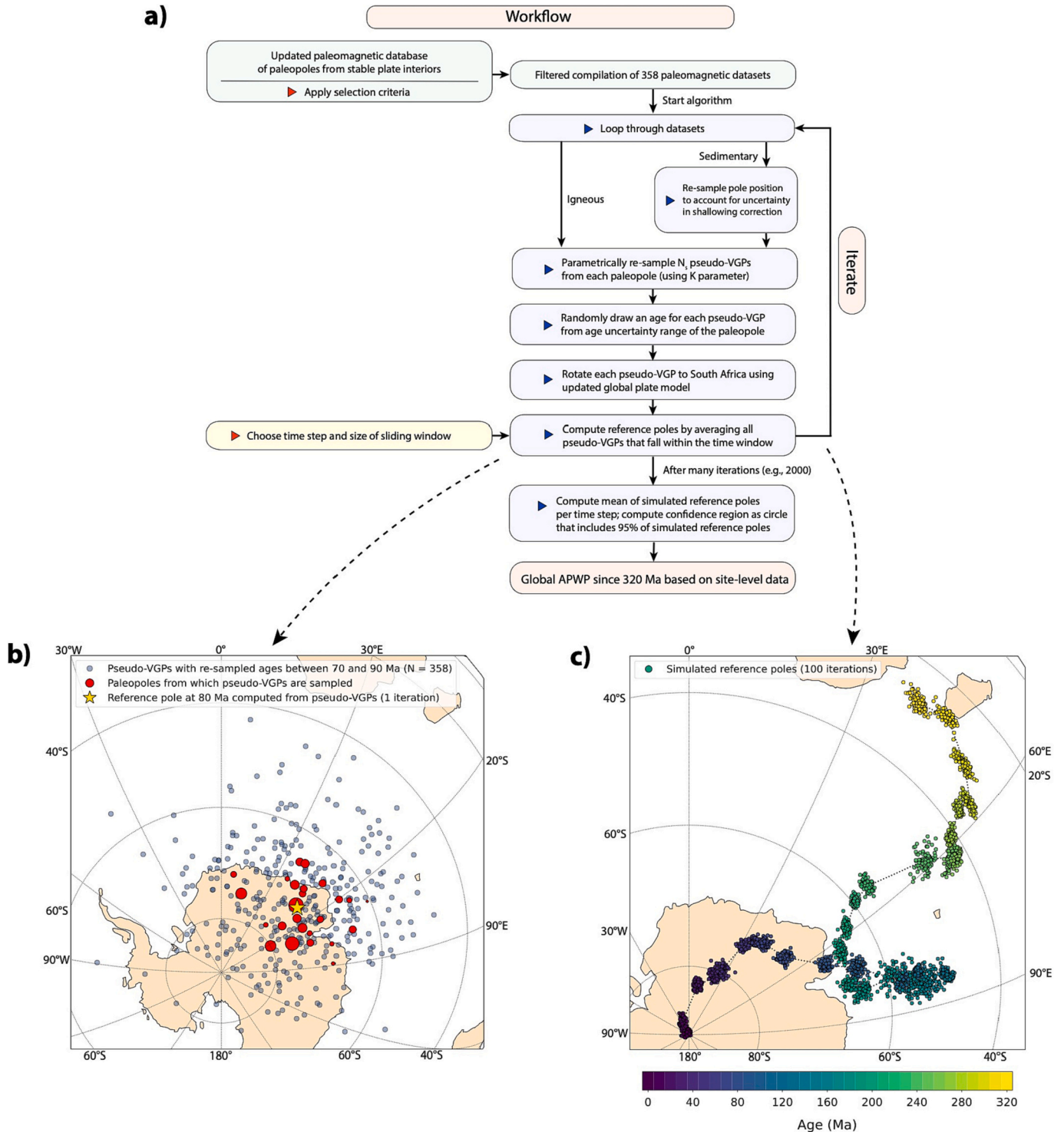
Fig. 2. a) Workflow for the computation of the new global APWP. **b)** Orthographic plot of the parametrically re-sampled VGPs with ages between 70 and 90 Ma (blue circles), which are derived from the paleopoles (red circles, size corresponds to number of VGPs sampled from pole) and used to compute a reference pole at 80 Ma. **c)** Orthographic plot showing the simulated reference poles obtained by 100 iterations. (For interpretation of the references to colour in this figure legend, the reader is referred to the web version of this article.)

2005; Swanson-Hysell et al., 2019; Wu et al., 2021; Gallo et al., 2021; Rose et al., 2022). However, the majority of the APWPs computed in these studies were still derived from paleopole-level data, and these weighting methods did not explicitly account for the subjectivity in the choice of the number of data underpinning each paleopole.

The approach chosen in this paper is aimed at overcoming these problems: we compute an APWP from simulated site-level paleomagnetic data instead of from paleopoles (e.g., McElhinny et al., 1974; Hansma and Tohver, 2020; Vaes et al., 2022; Gallo et al., 2023). In this approach, equal weight is given to each VGP that is simulated for a single 'site'. We here define a paleomagnetic 'site' as a geological unit that was formed in a short period of time relative to the time scale over which the geomagnetic field changes, such that the site mean direction represents a 'spot reading' of the paleomagnetic field (e.g., the site-mean direction from a lava flow, or a thin dyke) (see e.g., McElhinny and McFadden, 2000). Although it is often difficult to estimate the amount of geological time contained in a single sedimentary bed, individual samples obtained from sedimentary rocks may also provide independent readings of the past geomagnetic field (Tauxe and Kent, 2004; Bilardello and Kodama, 2010b). Demonstrating this may be challenging for small sediment-based datasets, but Vaes et al. (2021) recently formulated a stringent set of criteria to determine whether large paleomagnetic datasets ($n > 80$ directions) derived from sediments represent collections of paleomagnetic spot readings. *Site-level data* referred to hereafter in this manuscript thus includes site-mean directions from lavas flows or thin dykes, as well as individual directions obtained from a single sedimentary horizon or bed. The use of site-level data rather than paleopoles better reflects the underlying paleomagnetic data by assigning larger weight to larger datasets of independent measurements of the past geomagnetic field and avoids the subjectivity surrounding the definition of a paleopole.

3. Methods

We developed an approach to compute a global APWP for the last 320 Ma from simulated site-level paleomagnetic data. To obtain a paleomagnetic dataset at the site-level, we use an iterative, parametric re-sampling approach (Fig. 2). Although it would be possible to calculate a global APWP directly from published site-level data, compiling these from the many hundreds of studies with relevant input data would require a major effort and is complicated by the fact that not all these studies have reported their data at the site-level. Recent analysis, however, showed that parametric re-sampling of VGPs from a set of reported paleopoles and their statistical parameters provides an accurate approximation of the original distribution of VGPs, albeit with a slightly larger dispersion (Vaes et al., 2022). To generate a simulated site-level dataset, we first compiled a database of 'classical' paleomagnetic poles as reported in literature, with statistical properties that describe the number of underlying paleomagnetic sites and their dispersion, the sampling location, uncertainties associated with inclination shallowing correction, and age (see section 5). Using this database, we generate simulated site-level paleomagnetic data from each paleopole included in our compilation and repeat this procedure 2000 times (Fig. 2). This large number of iterations allows the propagation of both spatial and temporal uncertainties in the confidence bounds of the APWP. For each iteration, we parametrically re-sample a set of *pseudo*-VGPs from a Fisher (1953) distribution that is centered around the paleopole and defined by its precision parameter K. We generate the same number of VGPs as the number of sites that was included in the calculation of the paleopole (or grand mean paleomagnetic direction) reported in the original publication. In our approach, equal weight is thus assigned to each (*pseudo*-) VGP rather than to each paleopole, and the weight of each paleomagnetic dataset directly depends on its number of sites.

In our workflow, we also address the important source of uncertainty in the computation of APWPs that is known as 'inclination shallowing', which affects paleomagnetic datasets derived from sedimentary rocks. A 'blanket' correction factor (of $f = 0.6$ in Torsvik et al., 2012) has often been used in the computation of APWPs (e.g., Torsvik et al., 2012; Wu et al., 2021; Kulakov et al., 2021) but this underestimates the natural variation in the magnitude of inclination shallowing and assumes that all sediments are affected by shallowing which is not always the case (e. g., Bilardello and Kodama, 2010a; Bilardello et al., 2011; Kodama, 2012; Gallo et al., 2017; Kent and Muttoni, 2020; Vaes et al., 2021; Pierce et al., 2022). In the computation of our global APWP, we only include datasets from sedimentary rocks to which an inclination shallowing correction has been applied and whereby the uncertainty in the correction is quantified. Except for two datasets that were corrected using an anisotropy-based correction technique (Kodama, 2009; Brandt et al., 2019), all sedimentary datasets were corrected for inclination shallowing using the elongation-inclination (E/I) method of Tauxe and Kent (2004).

To incorporate the uncertainty in the shallowing correction in our workflow, we build upon the recent work of Pierce et al. (2022). These authors developed a way to express the uncertainty of the E/I correction as an uncertainty in paleomagnetic pole position along the great-circle between the paleopole and the sampling locality, i.e., in the co-latitude direction. Using the ensemble of flattening factor obtained from the bootstrapped ensemble of paleomagnetic directions, they computed the ensemble of possible paleomagnetic pole positions, each with a different paleomagnetic paleo- and co-latitude. Pierce et al. (2022) noted that the distribution of estimated paleolatitudes approximates that of a normal distribution. Here, we assume that the distribution of paleolatitudes, and thus the co-latitudes, approximates a normal distribution, and use this to incorporate the extra uncertainty in the co-latitude direction resulting from inclination shallowing. To this end, we compute the standard deviation of the colatitude distribution for every inclination shallowing corrected dataset in our compilation. We obtain this value either by applying the E/I correction to the individual paleomagnetic directions that were published in the original paper or provided to us by the authors. If we were unable to obtain the directional dataset, we derived the standard deviation from the reported 95% confidence regions on the inclination or paleolatitude by taking these confidence regions as two standard deviations. For the two datasets corrected by an anisotropy-based approach, we use the reported confidence regions on the correction to obtain this value. For each iteration in our workflow, we first re-sample the paleomagnetic co-latitude from a normal distribution with a mean corresponding to the co-latitude of the shallowing-corrected pole and the listed standard deviation. We then compute a new position of the paleopole – along the great-circle between the sampling location and the reported shallowing-corrected paleopole – using this re-sampled co-latitude and the paleomagnetic declination computed from the original shallowing-corrected pole. This procedure yields a new position of each sediment-derived paleopole, thereby incorporating the additional uncertainty in the co-latitude direction resulting from inclination shallowing. Next, *pseudo*-VGPs are generated from this new paleopole position, following the workflow outlined above (Fig. 2a).

The second step in our workflow is to propagate the uncertainties in the age of the sampled rocks. To this end, we randomly draw an age for each *pseudo*-VGP from a uniform distribution that corresponds to the age uncertainty range listed for each paleopole in the database. Quantifying the age uncertainty by a uniform distribution is intuitive for sediment-derived datasets, whose age uncertainty range is often determined by bio- and/or magnetostratigraphy, and a uniform distribution may straightforwardly be defined by the upper and lower age limit of the geological time period or interpreted magnetozones. The age of igneous rocks, on the other hand, is often based on radiometric dating, for which the uncertainty on individual age determinations is often reported as one or two standard deviation(s), and a Gaussian distribution could thus be used to quantify the uncertainty in age (see e.g., Swanson-Hysell et al., 2019; Wu et al., 2021; Gallo et al., 2021; Rose et al., 2022; Gallo et al., 2023). However, because the age of sampled igneous rocks is

typically determined by multiple radiometric ages, either from multiple dated samples or determined for the regional magmatic activity (e.g., for a large igneous province (LIP)), it is difficult to use a Gaussian distribution for the age uncertainty for all igneous datasets. We therefore choose a slightly more conservative approach and also use a uniform distribution between the upper and lower limit of the age range determined for the paleomagnetic datasets that were derived from igneous rocks.

In the third step of our workflow, we transfer the obtained collection of *pseudo*-VGPs to the same coordinate frame, for which we use an updated global model of relative plate motions (see section 4 and Tables 1 and S1). For each tectonic plate included in the plate circuit, we computed the Euler rotation poles per million years relative to a given reference plate, interpolating between reported total reconstruction poles assuming constant rotation rates. Here, we use South Africa as our

main reference plate, as is commonly done in the construction of global APWPs (e.g., Besse and Courtillot, 2002; Torsvik et al., 2008, 2012). We use this plate model to rotate each individual *pseudo*-VGP to South African coordinates after rounding its assigned age to the nearest integer. In this approach, we do not explicitly incorporate the uncertainties with the Euler rotation poles included in the global plate model, which were not always reported. On the other hand, this procedure propagates the effect of uncertainties in age on the relative plate motion and position of the tectonic plates from which the paleomagnetic data is derived.

In the fourth step, we determine a reference pole of the global APWP at a chosen interval and with a chosen sliding window. We use an interval of 10 Ma and a window of 20 Ma, which is the same as used for previously published global APWPs (e.g., Besse and Courtillot, 2002; Kent and Irving, 2010; Torsvik et al., 2008, 2012). In section 7.3, we explore the effects of using a smaller time interval and window. Because

Table 1

Overview of the global plate circuit used to transfer paleomagnetic data to a single reference plate. See Fig. 3 for a graphical overview. Full rotation parameters, chrons and references per Euler rotation pole are listed in Table S1. * = fit in Pangea same as in Torsvik et al. (2012), ^ = maximum age to which plate is connected to South Africa (701) in plate circuit.

Plate	ID	Moves relative to	Age range (Ma)	References	Notes
North America	101	Northwest Africa	0–203	DeMets et al. (2015),Müller et al. (1999, 2008) Gürer et al. (2022), Van Hinsbergen et al. (2020), Sahabi et al. (2004), Labails et al. (2010)	Fixed to Northwest Africa from 203 to 330 Ma*
Greenland	102	North America	0–125	Gaina and Jakob (2019), Torsvik et al. (2008), Roest and Srivastava (1989), Torsvik et al. (2012)	Fixed to North America from 125 to 330 Ma*
South America	201	South Africa	0–133.6	DeMets and Merkouriev (2019), Müller et al. (1999), Granot and Dyment (2015), Gaina et al. (2013), Torsvik et al. (2009)	Fixed to South Africa from 133.6 to 330 Ma*
Parana	202	South America	0–150	Torsvik et al. (2009)	Fixed to South America from 150 to 330 Ma*
Colorado	290	South America	0–150	Torsvik et al. (2009)	Fixed to South America from 150 to 330 Ma*
Patagonia	291	South America	0–190	Torsvik et al. (2009)	Fixed to South America from 190 to 330 Ma*
Eurasia	301	North America	0–220	DeMets et al. (2015), Vissers and Meijer (2012a, 2012b), Srivastava and Roest, 1996, 1989), Torsvik et al. (2008a), Alvey (2009)	Fixed to North America from 220 to 330 Ma*
Iberia	304	Eurasia	0–83.65^	Vissers and Meijer (2012a, 2012b)	
India	501	Somalia	0–59.237	DeMets and Merkouriev (2021)	
		Capricorn	59.237–83.65	Bull et al. (2010)	Correction for motion since ~16 Ma between Capricorn plate and India (see DeMets and Merkouriev, 2021)
		Madagascar	83.65–126.51	Gibbons et al. (2013)	
		Antarctica	126.51–160	Gibbons et al. (2013)	Fixed to Antarctica from 160 to 330 Ma
Arabia	503	Somalia	0–35	DeMets and Merkouriev (2016), Fournier et al. (2010)	Fixed to Northeast Africa from 35 to 330 Ma
Capricorn	511	India	0–59.237	Bull et al. (2010)	Fixed to India between ~16 to ~59 Ma
		Antarctica	59.237–83.65^	Cande and Patriat (2015)	
North China	601	Eurasia	0–130^	Torsvik and Cocks (2016)	Assumed fixed to Eurasia
South China	602	North China	0–130^	Replumaz and Tapponnier (2003)	Fixed to North China from 10 to 130 Ma
Madagascar	702	Somalia	0–170	Gaina et al. (2013)	Fixed to Somalia from 170 to 330 Ma
Moroccan Meseta	707	Northwest Africa	0–50	Van Hinsbergen et al. (2020)	Fixed to Northwest Africa from 50 to 330 Ma
Somalia	709	South Africa	0–19.535	DeMets and Merkouriev (2016)	Fixed to South Africa from ~20 to 330 Ma
Northwest Africa	714	South Africa	120–133.565	Torsvik et al. (2009)	Fixed to South Africa after 120 Ma and before 133.565 Ma*
Northeast Africa	715	South Africa	83.65–121.4	Torsvik et al. (2004)	Fixed to South Africa after 83.65 Ma and before 121.4 Ma*
Australia	801	Antarctica	0–136.657	Cande and Stock (2004), Whittaker et al. (2007, 2013), Williams et al. (2011)	Fixed to Antarctica from ~136 to 330 Ma
Antarctica	802	South Africa	0–51.724	DeMets et al. (2021)	
		Somalia	51.724–182	Cande and Patriat (2015), Mueller and Jokat (2019)	Fixed to Somalia from 182 to 330 Ma
Antarctic Peninsula	803	Antarctica	0–140	Van de Lagemaat et al. (2021)	Fixed to Antarctica from ~140–0 Ma
Marie Byrd Land	804	Antarctica	0–83.65^	Granot and Dyment (2018), Granot et al. (2013a, b), Cande and Stock (2004)	Fixed to Antarctica from ~62 Ma to 83.65 Ma (Van de Lagemaat et al., 2021)
Pacific	901	Marie Byrd Land	0–83.65^	Croon et al. (2008), Wright et al. (2015, 2016)	
Nazca	911	Pacific	0–22.34^	Tebbens and Cande (1997), Wright et al. (2016)	
Caribbean	2007	North America	0–38^	Leroy et al. (2000), Boschman et al. (2014)	Relative motion of Caribbean plate to Southern Cuba (North America) constrained by Cayman Trough anomalies

datasets cannot constrain variations that are smaller than the uncertainties of that dataset, we only include data collections in the analysis with an age uncertainty that is smaller than the chosen sliding window. The reference pole is computed based on all *pseudo*-VGPs whose assigned age falls within the chosen age window of the pole (Fig. 2b). In cases where the age uncertainty of a paleopole overlaps only partially with the time window of a reference pole, only the *pseudo*-VGPs are used that were assigned an age that falls in that time window. The contribution of each paleomagnetic dataset to a given reference pole of the APWP is thus weighted against the overlap between the age range of the dataset and the time window of the reference pole. Because in each iteration, the *pseudo*-VGPs are redrawn and are assigned a new random age, the number of VGPs that falls within the chosen time window will differ between iterations. So, although the total number of *pseudo*-VGPs that are generated for the entire APWP is equal for each iteration, the exact number of *pseudo*-VGPs that is used to compute each reference pole will vary due to the re-sampling of ages.

We compute each reference pole by taking the Fisher mean of the *pseudo*-VGPs that fall within the time window, yielding a reference *pseudo*-pole that provides an estimate of the time-averaged paleomagnetic pole position – and thus the rotation axis – in a South African coordinate frame. In addition, we compute a range of statistical parameters from the distribution of *pseudo*-VGPs, including the number of VGPs (N), the Fisher precision parameter (K), the 95% confidence region (A_{95}), the circular standard deviation (S) and the elongation parameter (E, computed as the ratio of eigenvalues τ_2/τ_3, see Tauxe et al., 2010). We use these statistical parameters to assess the robustness and identify potential biases in the distributions of the simulated VGPs that underlie the reference poles.

Finally, we repeat the above procedure 2000 times to average the variation in the obtained reference poles resulting from parametric resampling and to allow the determination of confidence regions for the global APWP (see Fig. 2c). We compute the final reference poles of the APWP by taking the Fisher mean of the 2000 reference *pseudo*-poles for each time step. We empirically calculate the 95% confidence region of the reference poles of the global APWP as the circle that includes 95% of the 2000 reference *pseudo*-poles, which we refer to as the P_{95}.

In this approach to calculating global apparent polar wander and its confidence, we thus incorporate a number of key uncertainties, including spatial and temporal uncertainties in the paleomagnetic datasets, the uncertainty associated with the E/I correction for inclination shallowing of sedimentary rocks, as well as uncertainties in the rotation of the VGPs to the reference coordinate system that results from uncertainties in age. All these uncertainties are reflected in the dispersion of the simulated VGPs, which is largely controlled by the between-pole dispersion of the coeval paleopoles and their K values that are used to parametrically re-sample the VGPs. Other incidental errors in the dataset, such as incorrect age assignments, unrecognized regional vertical-axis rotations, or unrecognized magnetic overprints, cannot be explicitly taken into account or corrected for, but such errors would likely lead to increased dispersion in the simulated VGPs per time window. We will compare the average scatter, elongation, and Fisher precision parameter of the simulated VGPs with values expected from PSV to assess whether and which reference poles may suffer from such errors.

4. Global plate model

The global apparent polar wander path is computed from paleomagnetic data from all stable plate interiors after rotating them relative to a single tectonic plate using a global model of relative plate motions. These relative plate motions are quantitatively described by Euler rotation poles that are mostly derived from marine magnetic anomaly identifications and fracture zone data. In the global plate model, each tectonic plate is linked – either directly or via a chain of neighboring plates – to the reference plate South Africa. We only include the major plates and continental blocks whose motions relative to South Africa are well-established, such that the available paleomagnetic data may be reliably combined to construct a global APWP. A schematic representation of the global plate circuit is shown in Fig. 3.

In our global plate model, we incorporate recently published Euler rotation poles based on the highest-resolution marine geophysical records. The original sources of the rotation poles for each tectonic plate are listed in Table 1, and we provide all rotation poles in Table S1. We note that many of these rotation poles were already used for the construction of previous global APWPs (e.g., Kent and Irving, 2010; Torsvik et al., 2008, 2012), as well as in global plate models (Seton et al., 2012; Torsvik and Cocks, 2016; Müller et al., 2016, 2019). The latest updates have mostly added more detail to the plate motion histories (e.g., DeMets and Merkouriev, 2021), but do not significantly change the long-term motions. Importantly, we have converted the ages of all the interpreted magnetic anomalies to the most recent geological time scale of Gradstein et al. (2020), which may shift the age of anomalies by up to a few million years compared to the ages assigned by the original authors.

Our global APWP uses data from the following tectonic plates or lithospheric fragments (with plate identification number) whose relative motions are constrained for the entire time period from which data were compiled for our global APWP, i.e., the last 330 Ma (Fig. 3): North America (101), Greenland (102), South America/Amazonia (201), Parana (202), Colorado (290), Patagonia (291), Eurasia (301), India (501), Arabia (503), South Africa (701), Madagascar (702), Moroccan Meseta (707), Somalia (709), Northwest Africa (714), Northeast Africa (715), Australia (801), and East Antarctica (802).

In addition, we have added several tectonic plates and blocks to our plate circuit, which were not included in the previous data compilation of Torsvik et al. (2012). The motions of these plates relative to South Africa are not sufficiently well-constrained (e.g., by marine geophysical data) for the entire time period covered by our global APWP but are well-constrained for a more limited time period. We thus include them for the period for which their motions relative in the global plate model are determined independently from paleomagnetic data (Table 1).

We have included paleomagnetic data from Iberia (304) for times after chron 34n (~83.65 Ma, the end of the Cretaceous Normal Superchron; CNS). Although marine magnetic anomaly-based Euler rotations are available for Iberian motion before the superchron, we do not incorporate data from this time because the interpretation and robustness of the underlying anomalies are under debate (e.g., Bronner et al., 2011; Tucholke and Sibuet, 2012). We have included data from the North and South China Blocks (601, 602) for times younger than 130 Ma, corresponding to the youngest age estimates for the cessation of significant motion along the Mongol-Okhotsk suture zone (e.g., van der Voo et al., 2015; Yang et al., 2015). We have included paleomagnetic data from the Antarctic Peninsula and neighboring islands (803) for the last 140 Ma, for which time it was rigidly attached to East Antarctica (van de Lagemaat et al., 2021). We include the Caribbean plate (2007) back to 38 Ma, for which time there is no relative motion of the Cuba segment relative to North America and relative Caribbean-North America motions are constrained by marine magnetic anomalies on the oceanic crust that underlies the Cayman Trough (Leroy et al., 2000; Boschman et al., 2014). Finally, we have included the Pacific (901) and Nazca (911) Plates in our plate circuit (for which marine magnetic anomaly data are available for times after 83.65 and 22.34 Ma, respectively), allowing us to rotate the paleomagnetic data obtained from young volcanic rocks (<10 Ma) to South Africa. The Nazca Plate is reconstructed relative to the Pacific Plate using the Euler rotation poles from Tebbens and Cande (1997) that were updated by Wright et al. (2016). The Pacific Plate (901) is linked to the 'main' plate circuit of the major continent-hosting plates via a relative plate motion chain through Marie Byrd Land (using rotation poles of Croon et al., 2008; Wright et al., 2016) and East Antarctica (Cande and Stock, 2004; Granot et al., 2013; Granot and Dyment, 2018).
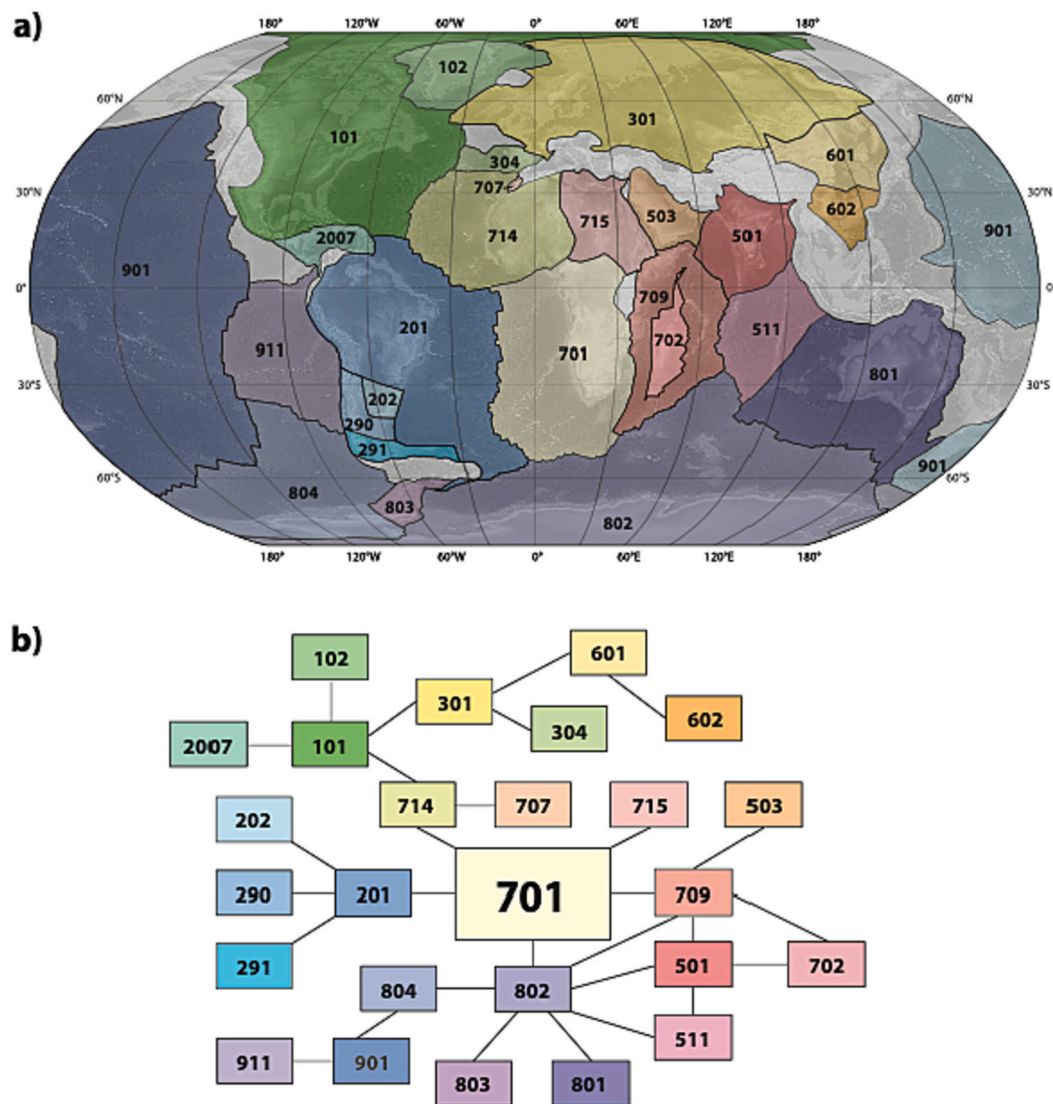
Fig. 3. a) Simplified global map of the tectonic plates from which the paleomagnetic data used for the global APWP is derived. **b)** Schematic representation of the global plate circuit used in this study. See Table 1 and S1 for more details. *Modified from* Van Hinsbergen et al. (2015).

In contrast to Torsvik et al. (2012), we have excluded data from the Colorado Plateau from North America for times before 40 Ma. After 40 Ma, widespread extension affected the western USA forming the Basin and Range province, but a detailed kinematic restoration of this extension of McQuarrie and Wernicke (2005) showed that the rotation of the Colorado Plateau relative to North America in this time window was no more than ~1°, which we consider negligible. For times prior to 40 Ma, the Colorado Plateau moved relative to North America during shortening in the Laramide and Sevier fold-thrust belts (Yonkee and Weil, 2015; Arkula et al., 2023), and these motions have only been quantified based on paleomagnetically determined rotations, with an estimated rotation of the Colorado Plateau relative to North America ranging from ~5 to ~13° (e.g., Bryan and Gordon, 1990; Molina-Garza et al., 1998; Steiner, 2003; Kent and Witte, 1993). Including data from this block using a paleomagnetism-based rotation correction would thus introduce circular reasoning.

Adria has often been proposed to be part of stable Africa and is rich in paleomagnetic data, which has led several authors to use Adria-derived paleomagnetic data as input for APWP computation (e.g., Muttoni et al., 2013; Kent and Muttoni, 2020; Channell et al., 2022). However, there is unequivocal evidence for rotation in GPS measurements today, and Adria must have experienced both a Neogene rotation during the

extension in the Sicily Channel, as well as a Triassic-Jurassic rotation during the opening of the oceanic eastern Mediterranean basin whose ocean floor is preserved in the Ionian Sea today (Van Hinsbergen et al., 2020, and references therein). While these rotations of Adria relative to Africa may have been small (5–10° in the reconstruction of Van Hinsbergen et al., 2020), the arguments for and against inclusion of Adria are based on the paleomagnetic data itself (Channell et al., 2022; Van Hinsbergen et al., 2014), and using this data would thus introduce circular reasoning. Data for Adria are therefore not used in our compilation.

Finally, for times prior to ~270 Ma, there is an ongoing debate about whether Pangea may be considered a single continent (e.g., Domeier et al., 2012) or was cut by an enigmatic and unpreserved megashear (e.g., Muttoni and Kent, 2019). The latter model is based on paleomagnetic arguments, and its predicted relative plate motions can therefore not be used as an independent basis for computing a global APWP from paleomagnetic data from all major plates. For this reason, we compute a global APWP for the 330–270 Ma time period under the assumption of a Pangea A configuration (i.e., a single plate from ~320 Ma, following Torsvik et al., 2008, 2012), which is obtained by closing the oceanic basins between the major continents using marine geophysical constraints. In section 7, we evaluate whether the data from the northern

and southern continents, or from the mobile belts that formed during Pangea formation as recently suggested by Pastor-Galán (2022), display systematic mismatches. Similar to the Pangea debate, Cogné et al. (2013) suggested that Asia and Europe moved in Cenozoic time over ~10° or more back and forth along enigmatic faults in the Ural and eastern Europe, to explain differences in paleomagnetic data from East Asia and the global APWP of Besse and Courtillot (2002). However, in absence of geological evidence for major Cenozoic cross-cutting fault zones, we treat Eurasia as a single plate in the Cenozoic.

5. Paleomagnetic database

5.1. Updated global reference database

We present here an updated database of paleomagnetic datasets for the tectonic plates and continental blocks described in the previous section (see Fig. 4, Table 2). Our compilation builds upon the efforts of the many paleomagnetists that collected, evaluated, and tabulated paleomagnetic results from hundreds of paleomagnetic studies of the last ~60 years, overviews of which have been published in a series of seminal papers (e.g., Irving, 1964, 1977; Irving and Irving, 1982; Van der Voo, 1990b; Lock and McElhinny, 1991; Torsvik et al., 2008, 2012) and compiled in the global paleomagnetic database. In this study, we used the data compilation presented in Torsvik et al. (2012) as a starting point. We have expanded this database by adding high-quality paleomagnetic results from undeformed or mildly folded regions that may be considered part of the stable plate interior, and that were published from 2012 to 2022, i.e., after the database of Torsvik et al. (2012) was compiled, as well as newly compiled datasets from the additional regions. We have also included datasets that were published prior to 2012 that were not incorporated by Torsvik et al. (2012), but that were included in recent compilations of 'cratonic' paleopoles (e.g., Gallo et al., 2021; Kulakov et al., 2021; González et al., 2022). For transparency, we have included all paleomagnetic data that were published

from stable plate interiors and that fit the basic criteria for inclusion (primary magnetization, modern demagnetization techniques, principal component analysis). When these data were subsequently excluded based on the selection criteria outlined in section 5.2, this is indicated in the database (Table S2).

For the last 10 Ma, we have limited our data compilation to the paleomagnetic datasets that were included in the PSV10 database (Cromwell et al., 2018). This database consists of 83 paleomagnetic datasets that are obtained from volcanic rocks that formed in the last 10 Ma. Not all of these datasets were used for the calculation of the global APWP, however, as some do not satisfy the selection criteria described in the next section. We note that not all of these datasets are obtained from regions that would be considered as 'stable' plate interiors. Following Cromwell et al. (2018), we assume that regional deformation has not significantly influenced the paleomagnetic results from these young rocks (predominantly <3 Ma) and assign each dataset to the most appropriate tectonic plate that is included in the global plate circuit as described in section 4 (e.g., a PSV10 dataset from Alaska is considered to be derived from North America). The paleomagnetic data in the PSV10 database is compiled on the site-level and contains 2401 VGPs. Instead of using the published site-level data, we have calculated the paleomagnetic poles from each dataset and generate simulated VGPs from those poles, to ensure consistency in our parametric re-sampling approach. We note that the application of this approach to the PSV10 database yields a distribution of simulated VGPs that mimics that of the published VGPs, as recently shown by Vaes et al. (2022).

We have compiled metadata and statistical parameters for each paleomagnetic dataset (Table 2), based on the information provided in the original publications. For the application of our selection criteria, we have classified the lithology of the sampled rocks as either igneous or sedimentary. We have listed the paleopole (latitude, longitude) for each entry in our database in south pole coordinates. When available, we used the paleopole from the original publication (if provided) or computed the pole by taking the Fisher mean of the reported site-level VGPs. If the
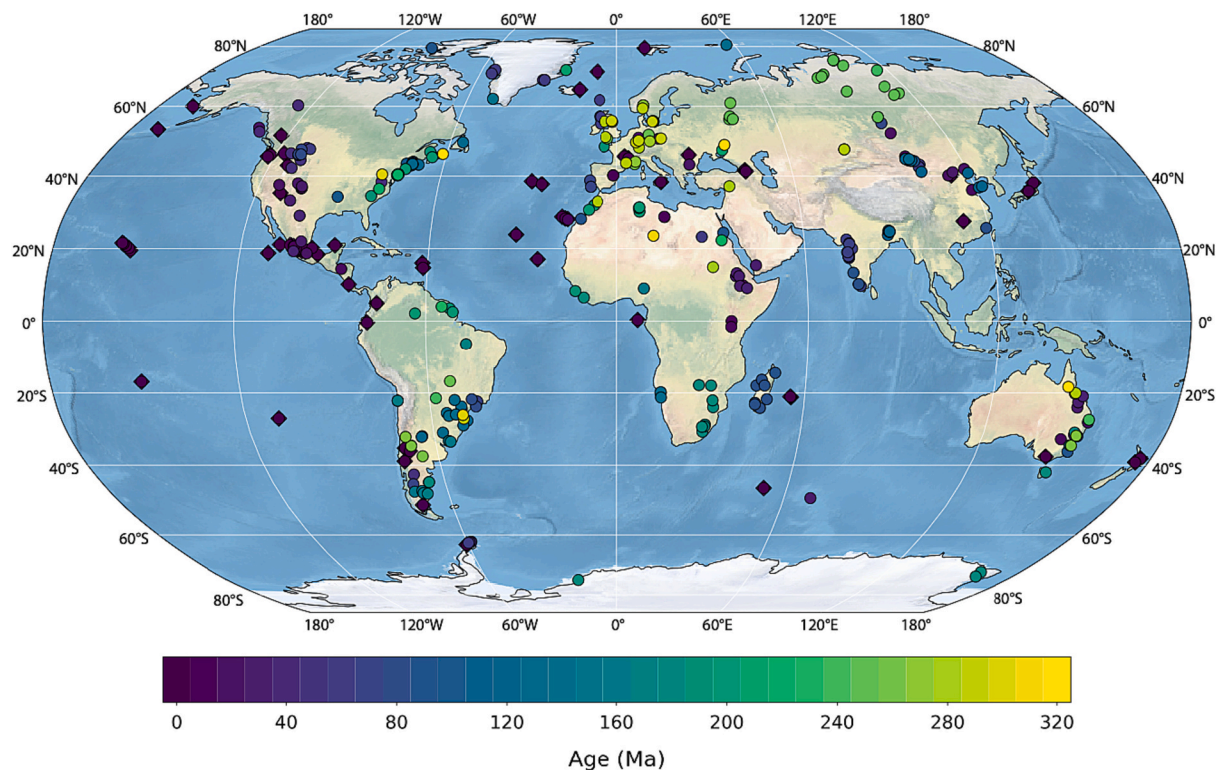

Fig. 4. Sampling locations of the 350 paleomagnetic datasets used for the calculation of the global APWP. Locations are colored by the mean age of the rocks. Diamonds indicate datasets from the PSV10 database (Cromwell et al., 2018).

Table 2

Paleomagnetic database used to compute the global APWP for the last 320 Ma. NB: data for the last 10 Ma from the PSV10 database are not included in this table. For the complete database, see Table S2. *Abbreviations*: Age_{min} and Age_{max} = lower and upper boundaries of age uncertainty range; Slat/Slon = latitude and longitude of (mean) sampling location; N = number of paleomagnetic sites used to compute the paleopole; A_{95} = radius of the 95% confidence circle about the mean of the distribution of VGPs; K = Fisher precision parameter of the distribution of VGPs; Plat/Plon = paleopole latitude and longitude (south pole); PlateID = plate identification number (see Fig. 2, Table 1); Rlat/Rlon = paleopole latitude and longitude in coordinate frame of South Africa; f = flattening factor (only for sedimentary data), p_{std} = standard deviation of the assumed normal distributed co-latitudes, obtained from E/I correction (only for sedimentary data); DB = database in which entry is listed (T12 = Torsvik et al. (2012), PSV10 = Cromwell et al. (2018) or added in this study).

Name	Age_{min}	Age_{max}	Age	Slat	Slon	N	K	A_{95}	Plat	Plon	PlateID	Rlat	Rlon	Lithology	f	p_{std}	Authors	Refno	DB
Prado section, Teruel, Spain	9.1	10.3	9.7	40.3	−1.1	246	16.5	2.3	−84.4	341.0	304	−84.3	350.9	sedimentary	0.5	6.5	Abels et al. (2009)		T12
Cascante, Spain	9.4	10.6	10.0	40.2	−1.1	81	15.4	4.1	−79.0	293.9	304	−79.7	297.9	sedimentary	0.9	4.34	Abdul Aziz et al. (2004)		T12
Jesus Maria and Atotonilco lavas	9.2	11.9	10.6	20.6	257.0	29	39.7	4.3	−80.7	292.3	101	−81.0	293.5	igneous			Goguitchaichvili et al. (2011)		this study
Volcanics, Jebel Soda, Libya	10.0	13.0	11.5	28.7	15.6	12	35.4	7.4	−78.4	16.1	715	−78.4	16.1	igneous			Schult and Soffel (1973)	50	T12
Volcanics, Jebel Soda, Libya	10.0	13.0	11.5	28.8	15.5	9	47.0	6.8	−69.0	4.0	715	−69.0	4.0	igneous			Ade-Hall et al. (1975)	60	T12
East African volcanics, Kenya and Tanzania	11.0	13.0	12.0	0.0	36.0	22	28.8	6.1	−86.5	6.6	709	−86.5	12.1	igneous			Reilly et al. (1976)	774	T12
Taatsyn Gol 3, Mongolia	12.1	13.3	12.7	45.5	101	7	14.5	16.4	−71.6	358.0	301	−71.2	1.8	igneous			Hankard et al. (2007a)		this study
Ethiopian traps, Debre Sina	10.6	14.9	12.8	9.9	39.8	30	27.7	5.1	−83.8	26.9	715	−83.8	26.9	igneous			Lhuillier and Gilder (2019)		this study
Miocene volcanics, Canary Islands	5.0	21.0	13.0	28.0	344.0	99	16.0	3.5	−81.9	294.4	714	−81.9	294.4	igneous			Watkins (1973)	25	T12
Volcanics, Kenya	12.0	15.0	13.5	−1.6	35.9	14	20.8	8.9	−80.1	214.3	709	−80.3	211.7	igneous			Patel and Raja (1979)	1517	T12
Padre Miguel Ignimbrite Suite, Honduras	14.3	16.3	15.3	14.4	272.9	33	24.5	5.2	−80.0	322.9	2007	−80.4	329.7	igneous			Molina-Garza et al. (2012)		this study
Hongshiya	14.0	18.0	16.0	36.2	118.5	9	57.8	6.8	−84.3	53.5	601	−82.7	58.1	igneous			Zhao et al. (1994)		this study
Leucitite	15.0	17.2	16.1	−32.84	146.45	17	20.5	8.6	−80.2	95.4	801	−82.8	33.6	igneous			Hansma and Tohver (2018)		this study
Trosky volcano, Czech Republic	15.7	17.3	16.5	50.52	15.23	11	21.5	10.1	−76.9	261.1	301	−78.6	263.0	igneous			Petronis et al. (2015)		this study
Hannuoba	15.0	24.0	19.5	40.2	112.7	16	36.3	6.2	−83.7	52.3	601	−81.5	57.7	igneous			Pan et al. (2005)		this study
Ust-Bokson, Mongolia	19.5	20.3	19.9	52.1	100.3	9	32.1	9.2	−69.8	6.5	301	−68.7	12.6	igneous			Hankard et al. (2007a)		this study
Jantetelco granodiorites and Tepexco volcanics	18.8	22.8	20.8	18.7	261.3	26	17.4	7.0	−78.4	4.28	101	−78.7	15.2	igneous			Duarte et al. (2015)		this study
Stoddard Mountain laccolith	20.0	22.0	21.0	37.6	246.6	19	54.3	4.6	−82.9	346.2	101	−83.5	359.7	igneous			Petronis et al. (2004)		T12
Suhindol volcanics	19.4	23.5	21.5	43.23	25.15	11	25.2	9.3	−84.1	242.1	301	−86.5	236.7	igneous			Van Hinsbergen et al. (2008a)		this study
Dinan Bay lavas	18.9	24.4	21.7	53.7	227.3	13	19.0	9.8	−82.7	301.7	101	−83.8	309.1	igneous			Irving et al. (2000)		T12
Younger plutons	22.0	23.0	22.5	36.6	254.5	11	34.8	7.8	−87.1	189.5	101	−86.6	176.2	igneous			Hagstrum and Johnson (1986)	1402	T12
Pingzhuang	22.0	23.0	22.5	42.0	119.2	17	49.9	5.1	−88.0	300.0	601	−88.0	22.1	igneous			Shi et al. (2002)		this study
Lake City Caldera	22.0	24.0	23.0	38.0	252.7	17	9.2	12.4	−76.4	30.3	101	−76.2	41.5	igneous			Reynolds et al. (1986)	1300	T12
Main Range Volcano and Tweed Volcano	20.2	26.7	23.5	−28.20	153.00	56	22.5	4.1	−74.2	74.8	801	−74.4	24.2	igneous			Wellman (1975)		this study
Latir volcanics	21.0	26.0	23.5	36.8	254.6	43	14.2	6.0	−80.9	331.2	101	−81.9	342.8	igneous			Hagstrum and Lipman (1986)	1299	T12
Volcanics Germany	18.0	30.0	24.0	50.8	8.0	40	15.4	6.0	−77.8	310.8	301	−78.9	323.9	igneous			Schreiber and Rotsch (1998)	3282	T12

Table 2 (*continued*)

Name	Age$_{min}$	Age$_{max}$	Age	Slat	Slon	N	K	A$_{95}$	Plat	Plon	PlateID	Rlat	Rlon	Lithology	f	p$_{std}$	Authors	Refno	DB
Zhangjiakou	17.0	33.0	25.0	41.1	114.7	8	9.0	19.5	−84.4	223.2	601	−86.6	201.3	igneous			Zheng et al. (1991)		this study
Conejos and Hinsdale Formation	23.0	29.0	26.0	37.2	254.4	23	15.2	8.0	−79.7	342.6	101	−80.5	356.4	igneous			Brown and Golombek (1997)	3130	T12
Kerguelen islands (Antarctic Plate)	24.0	30.0	27.0	−49.3	69.5	233	16.5	2.3	−85.5	9.3	802	−81.9	33.3	igneous			Camps et al. (2007)		T12
Springsure Volcano	27.3	28.9	28.1	−24.10	148.10	18	13.7	9.7	−70.5	120.6	801	−82.4	70.6	igneous			Hansma and Tohver (2019)		this study
Ignimbrita Panalillo Superior	24.8	31.3	28.1	22.0	259.0	41	27.4	3.6	−68.6	338.1	101	−69.5	349.6	igneous			González-Naranjo et al. (2012)		this study
Afro-Arabian flood volcanic province, Yemen	27.0	31.0	29.0	15.4	44.1	48	33.6	3.6	−74.2	69.1	503	−78.4	42.9	igneous			Riisager et al. (2005)		T12
Peak Range	28.2	31.2	29.7	−22.66	147.97	29	10.1	8.8	−64.6	111.8	801	−75.9	73.0	igneous			Hansma and Tohver (2019)		this study
Ethiopian traps, Belessa	29.2	30.5	29.9	12.4	37.7	42	44.9	3.3	−80.5	60.6	715	−80.5	60.6	igneous			Lhuillier and Gilder (2019))		this study
Lima Limo section, Ethiopian Traps	29.4	30.4	29.9	13.2	37.9	79	22.7	3.4	−78.2	33.0	715	−78.2	33.0	igneous			Ahn et al. (2021)		this study
Mongollon–Datil volcanics	24.0	36.0	30.0	33.3	252.1	61	17.6	4.5	−81.9	323.6	101	−83.1	343.5	igneous			Diehl et al. (1988)	1315	T12
Mongollon–Datil volcanics	24.0	36.0	30.0	33.3	252.2	39	21.0	5.1	−82.8	316.2	101	−84.2	336.4	igneous			McIntosh et al. (1992)	2631	T12
Ethiopian Traps, Ethiopia	29.0	31.0	30.0	12.4	38.6	53	28.9	3.7	−77.0	28.0	715	−77.0	28.0	igneous			Rochette et al. (1998)	3209	T12
Ethiopian Flood basalts, Abbay and Kessen gorges, Ethiopia	29.0	31.0	30.0	9.7	38.8	16	17.8	9.0	−83.0	13.3	715	−83.0	13.3	igneous			Kidane et al. (2002)	3496	T12
Mongolia, Jaran Plateau and Bogd Plateaus	30.2	30.4	30.3	44.8	100.7	13	25.1	8.4	−81.6	94.5	301	−77.9	88.7	igneous			Dupont-Nivet et al. (2010)		this study
Hillsborough Volcano	33.1	34.1	33.6	−20.98	149.00	14	32.2	7.1	−67.1	121.4	801	−80.6	68.8	igneous			Hansma and Tohver (2019)		this study
Liverpool Volcano	33.0	34.4	33.7	−31.70	150.20	36	25.7	4.8	−71.1	95.5	801	−74.8	28.5	igneous			Wellman et al. (1969)		this study
Southern Plateau volcanics, Ethiopia	30.0	38.0	34.0	9.1	41.0	22	24.4	6.4	−75.1	350.3	709	−75.3	351.8	igneous			Schult (1974)	40	T12
Tecalitlan Dikes	33.2	36.8	35.0	19.3	257.0	12	30.8	8.0	−75.7	346.6	101	−76.0	7.2	igneous			Rosas-Elguera et al. (2011)		this study
Mariscal Mountain Gabbro	35.0	39.0	37.0	29.1	256.8	18	42.5	5.4	−80.0	5.3	101	−79.1	31.6	igneous			Harlan et al. (1995)	2943	T12
Ramsay Island lavas	36.0	41.0	38.5	52.5	228.7	11	41.0	7.0	−78.2	299.9	101	−80.6	322.7	igneous			Irving et al. (2000)		T12
Talerua Member lavas	38.0	40.0	39.0	70.4	305.2	13	32.7	7.4	−76.3	21.5	102	−75.0	42.0	igneous			Schmidt et al. (2005)		T12
Mongolia, Khaton Sudal	38.8	40.0	39.4	44.5	101.3	7	45.1	9.1	−76.7	60.1	301	−70.5	65.6	igneous			Dupont-Nivet et al. (2010)		this study
Khaton Sudal, Mongolia	38.8	40.0	39.4	44.5	101.4	8	61.5	7.1	−71.9	22.6	301	−67.0	36.6	igneous			Hankard et al. (2007a)		this study
Beaver River alkalic complex	41.5	42.5	42.0	60.3	234.7	21	39.8	5.1	−79.2	325.8	101	−80.2	358.0	igneous			Symons et al. (2003)		T12
Monterey intrusives	42.0	47.0	44.5	38.4	280.6	11	12.3	13.6	−85.5	63.7	101	−81.7	84.7	igneous			Ressetar and Martin (1980)	1865	T12
Rattlesnake Hills volcanics	42.0	50.0	46.0	42.3	248.1	18	13.9	9.6	−79.4	326.2	101	−80.2	3.0	igneous			Sheriff and Shive (1980)	1712	T12
Bitterroot Dome dike swarm	44.0	51.0	47.0	46.4	245.2	11	34.9	7.8	−72.0	341.6	101	−72.0	9.0	igneous			Doughty and Sheriff (1992)	2560	T12
Eocene volcanics Patagonia	42.0	56.0	49.0	−42.6	290.0	36	18.0	5.7	−81.0	337.4	291	−74.2	34.1	igneous			Somoza (2007)		T12
Robinson Anticline intrusives	48.0	52.0	50.0	46.2	248.5	16	26.6	7.3	−77.1	325.8	101	−78.1	359.0	igneous			Harlan et al. (1988)	1348	T12

Table 2 (*continued*)

Name	Age$_{min}$	Age$_{max}$	Age	Slat	Slon	N	K	A$_{95}$	Plat	Plon	PlateID	Rlat	Rlon	Lithology	f	p$_{std}$	Authors	Refno	DB
Absoroka volcanics	45.0	55.0	50.0	44.5	249.8	42	13.5	6.2	−83.1	326.3	101	−83.5	15.9	igneous			Harlan and Morgan (2010)		T12
Combined Eocene intrusives	47.0	54.0	50.5	47.9	249.9	94	18.6	3.5	−82.7	347.2	101	−81.8	31.4	igneous			Diehl et al. (1983)	1270	T12
Ezcurra Inlet and Point Hennequin groups	47.8	56.0	51.9	−62.1	301.7	22	16.7	7.8	−79.0	48.0	803	−69.6	50.0	igneous			Watts et al. (1984)		this study
Barrington Volcano, New South Wales	52.0	54.0	53.0	−32.0	151.4	33	23.2	5.3	−70.5	125.6	801	−79.8	21.5	igneous			Wellman et al. (1969)	592	T12
Nuussuaq lavas, Kanisut Member	53.0	55.0	54.0	70.7	305.5	20	11.1	10.3	−74.6	339.4	102	−77.6	11.0	igneous			Riisager et al. (2003b)		T12
South Shetland Islands	52.2	56.5	54.4	−62.2	301.0	15	8.0	14.4	−82.1	2.6	803	−73.4	31.2	igneous			Gao et al. (2018)		this study
Kangerdlugsuaq dykes, Irminger	53.0	54.0	54.5	68.2	329.0	11	31.8	8.2	−62.9	0.4	102	−64.4	25.3	igneous			Faller and Soper (1979)	1604	T12
Skaergaard Intrusion	55.0	56.0	55.5	68.2	328.3	30	25.1	5.4	−61.0	345.0	102	−63.7	9.1	igneous			Schwarz et al. (1979)	1432	T12
Khuts Uul, Mongolia	56.3	57.9	57.1	43.2	104.6	14	34.9	6.8	−69.6	328	301	−69.2	358.8	igneous			Hankard et al. (2008)		this study
Svartenhuk lavas	54.0	61.5	57.8	71.4	305.5	30	9.3	9.1	−62.0	349.7	102	−64.2	16.0	igneous			Chauvet et al. (2019)		this study
Jacobsen Fjord dykes	53.0	60.0	59.0	68.2	329.0	22	33.3	5.5	−67.7	357.7	102	−69.2	27.7	igneous			Faller and Soper (1979)	1604	T12
East Gilf Kebir Plateau basalts	57.3	60.7	59.0	23.3	27.3	13	80.0	4.7	−71.7	23.5	715	−71.7	23.5	igneous			Lotfy and Odah (2015)		this study
Arran dikes, Scotland	58.8	60.0	59.4	55.6	354.8	413	17.8	1.7	−81.7	359.8	301	−75.1	42.8	igneous			Dagley et al. (1978)	1041	T12
Jacobsen Fjord basalts	59.0	60.0	59.5	68.2	329.0	39	11.1	7.2	−56.0	3.0	102	−57.3	27.7	igneous			Faller and Soper (1979)	1604	T12
Arran intrusives and extrusives	58.0	61.0	59.5	55.5	354.8	165	27.4	2.1	−80.2	339.6	301	−76.1	29.4	igneous			Hodgson et al. (1990)	3433	T12
Ardnamurchan complex, Scotland	59.6	60.4	60.0	56.7	353.8	62	23.8	3.8	−77.0	355.0	301	−71.7	31.3	igneous			Dagley et al. (1984)	1377	T12
Faeroe flood volcanics	59.5	60.7	60.1	61.9	353.1	43	14.2	6.0	−71.4	334.7	301	−69.6	8.4	igneous			Riisager et al. (2002)	3494	T12
Svartenhuk lavas, Vaigat Formation	60.0	61.0	60.5	71.6	305.9	10	25.1	9.8	−76.2	37.9	102	−73.7	73.2	igneous			Riisager et al. (2003b)		T12
Nuussuaq and Disko lavas, Vaigat Formation	60.0	61.0	60.5	70.3	305.1	14	19.8	9.2	−64.8	321.5	102	−69.4	345.5	igneous			Riisager et al. (2003a)		T12
Rhum and Canna igneous, Scotland	59.7	61.7	60.7	57.0	353.5	107	15.7	3.6	−81.0	359.0	301	−74.5	41.5	igneous			Dagley and Mussett (1981)	1169	T12
Mull lavas, Scotland	59.7	62.0	60.9	56.3	353.9	26	23.3	6.0	−73.3	346.2	301	−69.5	20.2	igneous			Ganerød et al. (2008)		T12
Torris, Snow, Half Moon, King George, Admirality lavas and intrusions	56.0	66.0	61.0	−62.4	300.3	10	19.8	11.1	−82.7	355.2	803	−73.4	28.0	igneous			Poblete et al. (2011)		this study
Antrim Lava, Ireland	59.6	62.6	61.1	54.9	353.9	37	15.0	6.3	−78.9	347.0	301	−74.1	30.8	igneous			Ganerød et al. (2010)		T12
Muck and Eigg igneous	60.9	61.4	61.2	56.9	353.8	133	13.0	3.5	−74.0	351.0	301	−69.5	24.7	igneous			Dagley and Mussett (1986)	1204	T12
Sumber Uul - Tulga, Mongolia	56.2	68.0	62.1	43	104	14	85.0	4.3	−85.2	272.5	301	−84.0	56.5	igneous			Hankard et al. (2008)		this study
Combined Paleocene intrusions	59.0	67.0	63.0	47.6	251.1	36	20.2	5.4	−81.8	1.4	101	−81.1	38.4	igneous			Diehl et al. (1983)	1270	T12
Mount Pavagarh Traps, Gujrat, India	60.0	68.0	64.0	22.5	73.5	16	52.5	5.1	−39.2	105.6	501	−71.6	63.1	igneous			Verma and Mital (1974)	94	T12
Deccan Traps, Mahabaleshwar, India	64.0	67.0	65.5	17.9	73.6	28	12.8	7.4	−40.0	96.0	501	−69.2	43.4	igneous			Kono et al. (1972)	107	T12

Table 2 (*continued*)

Name	Age_min	Age_max	Age	Slat	Slon	N	K	A_95	Plat	Plon	PlateID	Rlat	Rlon	Lithology	f	p_std	Authors	Refno	DB
Deccan Traps, Nagpur to Bombay traverse, India	64.0	67.0	65.5	20.0	75.0	16	37.9	6.1	−38.4	102.4	501	−71.3	57.6	igneous			Vandamme et al. (1991)	393	T12
Deccan dyke swarms, western India	64.0	67.0	65.5	21.5	74.3	11	23.0	9.7	−37.2	99.5	501	−68.9	54.3	igneous			Prasad et al. (1998)	3094	T12
Khumbarli Ghat, Mahabeleshwar Plateau, India	64.0	67.0	65.5	17.4	73.7	15	24.6	7.9	−44.7	107.8	501	−78.7	54.2	igneous			Jay et al. (2009)		T12
Varandah Ghat, Mahabeleshwar Plateau, India	64.0	67.0	65.5	18.1	73.6	15	28.8	7.2	−33.5	106.7	501	−68.7	73.6	igneous			Jay et al. (2009)		T12
Wai-Panchgani, Mahabeleshwar Plateau, India	64.0	67.0	65.5	17.9	73.8	16	14.7	10.0	−36.8	85.9	501	−61.3	35.7	igneous			Jay et al. (2009)		T12
Kelgar, Mahabeleshwar Plateau, India	64.0	67.0	65.5	17.9	73.7	16	21.2	8.2	−42.3	96.6	501	−71.1	39.3	igneous			Jay et al. (2009)		T12
Tapola, Mahabeleshwar Plateau, India	64.0	67.0	65.5	17.8	73.7	17	17.1	8.9	−38.2	95.5	501	−67.7	46.0	igneous			Jay et al. (2009)		T12
Matheran Ghat, Mahabeleshwar Plateau, India	64.0	67.0	65.5	19.0	73.3	17	36.0	6.0	−36.6	108.4	501	−72.1	73.6	igneous			Jay et al. (2009)		T12
Ambenali Ghat, Mahabeleshwar Plateau, India	64.0	67.0	65.5	17.9	73.6	34	16.8	6.2	−38.8	104.5	501	−72.5	61.2	igneous			Jay et al. (2009)		T12
Nandurbar-Dhule dykes, India	63.0	68.4	65.7	21.3	74.3	13	13.5	11.7	−40.5	104.5	501	−74.2	57.7	igneous			Das et al. (2021)		this study
Western Ghats, Deccan Traps, India	64.0	68.5	66.3	19.0	73.5	50	28.7	3.8	−37.8	102.6	501	−71.7	57.9	igneous			Chenet et al. (2009)		this study
Late Cretaceous mafic dikes in Kerala	65.0	70.0	67.5	10.2	76.1	10	56.8	6.5	−37.7	107.0	501	−74.8	66.1	igneous			Radhakrishna and Joseph (2012)		this study
Central Kerala dykes, India	68.0	70.0	69.0	9.7	76.7	6	33.4	11.8	−34.6	94.0	501	−67.1	42.7	igneous			Radhakrishna et al. (1994)	2754	T12
Itatiaia and Passa Quatro Complexes, Brazil	67.0	74.0	70.5	−22.4	315.2	18	37.8	5.7	−79.5	0.0	201	−69.6	46.7	igneous			Montes-Lauar et al. (1995)	3261	T12
Patagonian Plateau basalts, Chile, Argentina	64.0	79.0	71.5	−45.3	288.7	18	31.6	6.3	−78.7	358.4	291	−68.8	45.4	igneous			Butler et al. (1991)	2374	T12
Lisbon Basalts 1969, Portugal	70.0	74.0	72.0	38.83	−9.18	5	72.3	9.1	−73.7	19.6	304	−69.3	35.6	igneous			Van der Voo (1969)		this study
Monchique Syenite I	70.0	74.0	72.0	37.06	−8.82	8	104.9	5.4	−73.5	344.6	304	−71.9	7.0	igneous			Van der Voo (1969)		this study
Monchique Syenite II	70.0	74.0	72.0	37.06	−8.82	27	47.8	4.1	−77.1	347.1	304	−75.1	13.9	igneous			Storetvedt et al. (1990)		this study
Adel Mountain volcanics	71.0	81.0	76.0	47.5	248.1	26	16.7	7.2	−83.4	20.9	101	−80.0	61.7	igneous			Gunderson and Sheriff (1991)	2370	T12
Minusa trough intrusions, Siberia	74.0	79.0	76.5	55.0	99.2	16	37.5	6.1	−82.8	8.5	301	−73.3	55.1	igneous			Metelkin et al. (2007)		this study
Doherty Mountain sills	76.5	77.5	77.0	45.9	248.1	5	33.6	13.4	−80.8	358.1	101	−78.2	42.6	igneous			Harlan et al. (2008)		T12
Elkhorn Mountains	77.0	83.0	80.0	46.1	248.0	15	16.8	9.6	−80.3	9.5	101	−76.2	52.7	igneous			Diehl (1991)	2382	T12
Maudlow Formation welded tuffs	75.0	85.0	80.0	46.1	248.9	11	22.7	9.8	−69.8	27.8	101	−65.1	60.3	igneous			Swenson and McWilliams (1989)	2397	T12
Sao Sabastiao Island Intrusions, Brazil	78.0	84.0	81.0	−23.8	314.7	18	50.7	4.9	−79.4	331.9	201	−69.4	40.5	igneous			Montes-Lauar et al. (1995)	3261	T12
Pocos de Caldas Alkaline Complex, Brazil	78.0	90.0	84.0	−21.8	313.5	47	60.3	2.7	−83.2	320.1	201	−71.9	48.5	igneous			Montes-Lauar et al. (1995)	3261	T12
Volcanics, Massif d'Androy Andria	84.0	90.0	87.0	−24.2	46.0	6	36.0	11.3	−64.0	63.0	702	−63.5	63.1	igneous			Andriamirado and Roche (1969)	547	T12

Table 2 (*continued*)

Name	Age$_{min}$	Age$_{max}$	Age	Slat	Slon	N	K	A$_{95}$	Plat	Plon	PlateID	Rlat	Rlon	Lithology	f	p$_{std}$	Authors	Refno	DB
Volcanics, Mailaka Andria	84.0	90.0	87.0	−18.0	44.4	10	35.2	8.3	−70.3	63.1	702	−69.8	63.4	igneous			Andriamirado (1971)	708	T12
Volcanics, Mangoky–Anilahy Andria	84.0	90.0	87.0	−22.8	44.3	11	21.8	10.0	−73.7	73.1	702	−73.2	73.3	igneous			Andriamirado (1971)	708	T12
Volcanics, Antanimena Andria	84.0	90.0	87.0	−16.4	46.0	12	48.7	6.3	−66.1	49.7	702	−65.7	50.1	igneous			Andriamirado (1971)	708	T12
Volcanics, Southeast Coast Andria	84.0	90.0	87.0	−21.8	48.0	14	42.1	6.2	−65.8	35.6	702	−65.5	36.2	igneous			Andriamirado (1971)	708	T12
Volcanics, Southwest Madagascar	84.0	90.0	87.0	−23.2	44.3	41	68.1	2.7	−76.8	68.2	702	−76.3	68.8	igneous			Torsvik et al. (1998)	3210	T12
Dolerites, east Madagascar	84.0	90.0	87.0	−18.0	47.0	16	38.8	6.0	−65.5	38.0	702	−65.2	38.5	igneous			Storetvedt et al. (1992)	3211	T12
Late Cretaceous mafic dikes in Kerala	85.0	90.0	87.5	10.2	76.1	6	42.1	10.4	−26.8	113.1	501	−72.7	67.6	igneous			Radhakrishna and Joseph (2012)		this study
Yongtai	87.9	88.6	88.3	25.7	119.0	19	76.5	3.9	−83.1	332.6	602	−73.4	62.3	igneous			Huang et al. (2013)		this study
St. Mary Islands, western India	91.0	91.4	91.2	13.4	74.7	7	42.1	9.4	−14.2	117.8	501	−61.8	84.2	igneous			Torsvik et al. (2000)		T12
d'Analava complex	91.3	91.9	91.6	−14.5	50.1	5	41.6	12.0	−66.7	43.5	702	−66.4	44.0	igneous			Meert and Tamrat (2006)		T12
Amma Fatma section, Morocco	89.4	93.9	91.7	28.2	348.2	88	38.7	2.5	−64.3	76.3	707	−65.0	75.1	sedimentary	0.70	4.0	Ruiz-Martínez et al. (2011)		this study
Wadi Natash volcanics, Egypt	86.0	100.0	93.0	24.4	34.3	15	44.4	5.8	−69.3	78.1	715	−69.4	78.3	igneous			Schult et al. (1982)	1500	T12
Khurmun Uul - Shovon basalts, Mongolia	90.8	96.0	93.4	44.2	103.4	23	22.2	6.6	−84.7	15.0	301	−66.5	73.5	igneous			Hankard et al. (2007b)		this study
Mount Dromedary Intrusion	92.0	96.0	94.0	−36.30	150.70	22	11.5	9.5	−55.9	138.6	801	−68.6	76.4	igneous			Robertson (1963)		this study
Axel Heiberg lavas	93.2	97.2	95.2	79.4	267.6	36	15.0	6.4	−70.4	17.0	101	−58.9	64.9	igneous			Tarduno et al. (2002)		this study
Magnet Cove and other intrusions	98.0	102.0	100.0	34.3	267.5	20	34.0	5.7	−74.1	12.5	101	−61.5	68.3	igneous			Globerman and Irving (1988)	1322	T12
Cuttingsville	99.7	100.3	100.0	43.5	287.1	5	50.2	10.9	−72.1	17.0	101	−59.2	69.7	igneous			McEnroe (1996a)	3087	T12
Tsost Magmatic Field, Mongolia	94.7	107.0	100.9	44.3	102.2	7	19.2	14.1	−82.1	324.9	301	−68.1	68.4	igneous			Van Hinsbergen et al. (2008b)		this study
Little Rattlesnake Complex	108.0	114.0	111.0	43.0	288.9	12	71.2	5.2	−71.5	2.6	101	−56.6	69.3	igneous			McEnroe (1996a)	3087	T12
Pleasant Mountain	111.7	112.5	112.1	44.0	289.2	5	88.5	8.2	−77.4	5.0	101	−61.3	75.8	igneous			McEnroe (1996a)	3087	T12
Suhongtu	110.6	114.1	112.4	41.2	104.1	31	64.4	3.2	−80.3	20.3	601	−56.4	81.4	igneous			Ren et al. (2004); Zhu et al. (2008)		this study
Burnt Meadow Mountains	112.4	112.8	112.6	43.9	289.1	10	51.9	6.8	−75.7	28.5	101	−57.7	85.1	igneous			McEnroe (1996a)	3087	T12
Cretaceous Lamproites	109.1	116.6	112.9	23.8	87.0	11	30.5	8.4	−14.9	107.6	501	−58.8	62.7	igneous			Radhakrishna et al. (2017)		this study
Rajmahal Traps, West Bengal and Bihar, India	115.0	117.0	116.0	24.8	87.7	16	91.0	6.0	−3.2	117.5	501	−51.3	86.6	igneous			McDougall and McElhinny (1970)	633	T12
Rajmahal Traps, Bihar, India	115.0	117.0	116.0	24.6	87.7	25	29.8	5.4	−7.0	117.0	501	−54.9	84.3	igneous			Klootwijk (1971)	678	T12
Rajmahal Traps, West Bengal, India	115.0	117.0	116.0	25.0	87.4	19	10.6	10.8	−9.3	124.8	501	−58.5	97.5	igneous			Das et al. (1996)	2977	T12
Rajamahal Traps, North Rajmahal Hills, India	115.0	117.0	116.0	24.7	87.5	8	52.8	7.7	−6.5	120.2	501	−55.1	89.9	igneous			Tarduno et al. (2001)		T12
Hongyan	114.0	118.0	116.0	36.9	121.2	11	27.3	8.9	−86.5	341.1	601	−61.9	88.1	igneous			Charles et al. (2013)		this study
Rajmahal Traps, Bihar, India	116.0	118.0	117.0	24.7	87.7	34	53.7	3.4	−9.4	116.6	501	−57.0	82.5	igneous			Rao and Rao (1996)	3095	T12

Table 2 (*continued*)

Name	Age$_{min}$	Age$_{max}$	Age	Slat	Slon	N	K	A$_{95}$	Plat	Plon	PlateID	Rlat	Rlon	Lithology	f	p$_{std}$	Authors	Refno	DB
South-East Artz Bogd, Mongolia	115.4	119.3	117.4	44.4	102.5	24	38.1	4.9	−75.6	312.3	301	−64.8	64.2	igneous			Van Hinsbergen et al. (2008b)		this study
Weideshan	116.0	120.0	118.0	37.2	122.4	9	33.7	9.0	−80.1	0.1	601	−56.7	79.1	igneous			Charles et al. (2011)		this study
Jianchang	117.0	121.0	119.0	40.9	119.8	5	31.5	7.6	−81.1	44.2	601	−52.9	90.3	igneous			Qin et al. (2011)		this study
Alfred Complex	118.0	122.0	120.0	43.5	289.3	14	64.1	5.0	−74.0	29.8	101	−53.5	87.8	igneous			McEnroe (1996b)	3036	T12
Cape Neddick	120.2	121.0	120.6	43.2	291.4	12	67.5	5.3	−74.8	354.8	101	−57.1	73.3	igneous			McEnroe (1996b)	3036	T12
Vulcanitas Cerro Colorado Formation, Cordoba, Argentina	115.0	127.0	121.0	−32.0	−64.0	6	27.5	13.0	−81.0	14.0	202	−49.6	71.3	igneous			Valencio (1972)	123	T12
South-East ih Bogd, Mongolia	118.2	124.3	121.3	44.8	100.7	21	34.3	5.7	−83.7	16.4	301	−56.0	88.2	igneous			Van Hinsbergen et al. (2008b)		this study
Tatnic Complex	120.0	124.0	122.0	43.3	289.3	10	65.2	6.0	−65.9	27.8	101	−44.8	86.0	igneous			McEnroe (1996b)	3036	T12
Florianopolis dyke swarm, Santa Catarina Island, Brazil	119.0	128.3	123.7	−27.7	311.5	65	47.3	2.6	−89.1	3.3	201	−56.5	76.0	igneous			Raposo et al. (1998)	3190	T12
South-East Baga Bogd, Mongolia	122.7	124.7	123.7	44.8	101.9	29	18.8	6.3	−79.9	339.9	301	−57.9	79.0	igneous			Van Hinsbergen et al. (2008b)		this study
El Salto–Almafuerte lavas, Cordoba, Argentina	119.0	129.0	124.0	−32.2	−64.2	15	39.4	6.2	−72.0	25.0	202	−39.3	73.3	igneous			Mendía (1978)	1087	T12
Lebanon diorite	122.0	128.0	125.0	43.4	289.2	5	70.9	9.1	−71.0	16.9	101	−50.1	83.5	igneous			McEnroe (1996b)	3036	T12
Notre Dame Bay dikes	122.0	136.0	129.0	49.5	304.6	10	99.5	4.9	−67.2	30.8	101	−44.6	91.6	igneous			Lapointe (1979)	1854	T12
Ponta Grossa dykes, Brazil	129.2	131.4	130.3	−24.5	310.0	115	43.8	2.0	−82.4	30.3	201	−47.0	77.7	igneous			Raposo and Ernesto (1995)	2958	T12
Ponta Grossa dykes	129.2	131.4	130.3	−23.8	310.0	24	35.7	5.0	−88.1	222.0	201	−56.2	78.0	igneous			Cervantes Solano et al. (2015)		this study
Serra Geral basalts, Brazil	131.0	135.0	133.0	−29.0	310.0	37	40.4	3.7	−84.6	115.4	202	−52.0	86.8	igneous			Pacca and Hiodo (1976)	765	T12
Kaoko lavas, Namibia	131.0	136.0	133.5	−20.0	14	40	59.3	3.0	−48.3	86.6	701	−48.3	86.6	igneous			Gidskehaug et al. (1975)	126	T12
Etendeka, Namibia	131.0	136.0	133.5	−20.0	14.1	21	26.1	6.3	−47.5	88.9	701	−47.5	88.9	igneous			Owen-Smith et al. (2019)		this study
Etendeka LIP (upper), Namibia	131.0	136.0	133.5	−19.9	14.1	33	30.3	4.6	−47.2	84.2	701	−47.2	84.2	igneous			Dodd et al. (2015)		this study
Etendeka LIP (lower), Namibia	131.0	136.0	133.5	−21.3	14.2	37	26.2	4.7	−52.3	91.7	701	−52.3	91.7	igneous			Dodd et al. (2015)		this study
Parana flood basalt, Alto Paraguay Formation, Paraguay	132.0	136.0	134.0	−25.6	−54.9	18	65.0	4.3	−86.2	359.2	201	−52.3	75.6	igneous			Goguitchaichvili et al. (2013)		this study
Posadas Formation, Parana flood basalts	132.0	136.0	134.0	−26.4	−54.3	26	45.6	4.2	−89.7	339.1	201	−55.3	78.8	igneous			Mena et al. (2011)		this study
Arapey volcanics, Uruguay	132.0	136.0	134.0	−31.0	303.0	29	42.0	4.2	−84.8	95.8	202	−50.2	85.2	igneous			Cervantes-Solano et al. (2010)		this study
Central Parana Magmatic Province	132.0	136.0	134.0	−26.0	308.0	96	34.3	2.5	−84.1	69.2	201	−50.4	84.4	igneous			Owen-Smith et al. (2019)		this study
Northern Parana Magmatic Province, Brazil	132.0	136.0	134.0	−22.0	308.0	128	48.0	1.8	−82.7	84.5	201	−50.3	87.9	igneous			Ernesto et al. (2021)		this study
Franz Josef Land LIP	125.0	145.0	135.0	80.7	56.0	40	26.2	4.5	−68.9	357.5	301	−46.3	73.4	igneous			Abashev et al. (2018)		this study
Southwest Greenland dykes	144.2	151.0	147.6	62.3	310.2	40	25.1	4.6	−69.3	5.0	102	−50.9	85.9	igneous			Kulakov et al. (2021)		this study
La Negra south	151.2	154.4	152.8	−22.2	289.8	18	11.2	10.8	−84.5	76.4	290	−48.0	84.1	igneous			Fu et al. (2020)		this study

Table 2 (*continued*)

Name	Age$_{min}$	Age$_{max}$	Age	Slat	Slon	N	K	A$_{95}$	Plat	Plon	PlateID	Rlat	Rlon	Lithology	f	p$_{std}$	Authors	Refno	DB
Posades and Sierra Colorado ignimbrites, Argentina	153.0	157.0	155.0	−47.4	−71.8	16	24.5	7.6	−81.0	172.0	291	−57.9	90.4	igneous			Iglesia Llanos et al. (2003)	3535	T12
Chon Aike Formation, Argentina	151.5	158.5	155.0	−47.2	−69.0	23	13.3	8.6	−84.3	191.3	291	−56.9	83.0	igneous			Ruiz González et al. (2019)		this study
La Mathilde Formation, Patagonia	156.7	158.1	157.4	−47.8	291.2	10	13.6	13.6	−84.1	179.2	291	−56.4	85.1	igneous			Ruiz González et al. (2022)		this study
Nico Perez dykes, Uruguay	154.6	160.6	157.6	−33.3	−55.6	8	30.0	10.2	−87.0	197.3	202	−55.7	79.8	igneous			Lossada et al. (2014)		this study
Zapican dike swarm, Uruguay	154.6	160.6	157.6	−33.5	−55.0	19	22.7	7.2	−86.4	178.9	202	−58.2	83.4	igneous			Cervantes-Solano et al. (2020)		this study
Intrusive rocks, Nigeria	150.0	170.0	160.0	9.0	8.6	6	27.8	13.0	−62.5	61.6	714	−61.3	65.8	igneous			Marton and Marton (1976)	1081	T12
La Negra north	162.2	169.4	165.8	−22.2	289.8	28	13.8	7.6	−84.3	180.9	290	−56.8	84.4	igneous			Fu et al. (2020)		this study
Chon Aike Formation, Patagonia	166.0	170.0	168.0	−48.0	292.6	13	10.3	13.5	−81.2	207.7	291	−59.7	81.4	igneous			Vizán (1998)		this study
Gingenbullen Dolerite	167.0	177.0	172.0	−34.5	150.3	7	9.2	21.0	−52.0	153.0	801	−46.3	66.2	igneous			Thomas et al. (2000)		this study
West Maranhao Basalts, Brazil	173.0	177.0	175.0	−6.4	−47.4	15	31.8	6.9	−85.3	262.5	201	−58.5	72.7	igneous			Schult and Guerreiro (1979)	1431	T12
Garrawilla volcanics and Nombi extrusives	177.0	183.0	180.0	−31.0	150.0	14	16.8	10.0	−46.1	175.2	801	−59.7	77.2	igneous			Schmidt (1976)	780	T12
Batoka basalts, northern Zimbabwe	177.5	183.3	180.4	−17.9	26.2	5	27.4	14.9	−63.9	80.6	701	−63.9	80.6	igneous			Jones et al. (2001)		T12
Northern Victoria Land - Kirkpatrick Basalts	179.5	182.5	181.0	−71.8	162.0	8	28.0	9.3	−72.0	236.0	802	−51.3	54.0	igneous			Rolf and Henjes-Kunst (2003)		this study
Gair Mesa, Kirkpatrick basalts	179.5	182.5	181.0	−73.3	162.9	22	22.9	7.0	−66.4	222.7	802	−55.2	64.3	igneous			Lemna et al. (2016)		this study
Marifil Complex, Patagonia	177.0	185.0	181.0	−44.8	−65.7	25	12.2	8.7	−80.5	203.5	291	−58.9	83.4	igneous			Vizán (1998)		this study
Naude's Nek section, Karoo LIP	180.1	182.8	181.5	−30.76	28.04	15	30.8	7.0	−76.0	88.8	701	−76.0	88.8	igneous			Moulin et al. (2011)		this study
Oxbow-Moteng Pass section, Karoo LIP	180.1	182.8	181.5	−28.8	28.7	29	27.9	5.2	−65.3	87.9	701	−65.3	87.9	igneous			Moulin et al. (2017)		this study
Karroo dolerites combined, South Africa, Zimbabwe	179.0	187.0	183.0	−24.0	31.0	10	16.4	12.3	−65.4	75.1	701	−65.4	75.1	igneous			McElhinny and Jones (1965)	317	T12
Karroo lavas, Central Africa, Zimbabwe, Mozambique	179.0	187.0	183.0	−18.0	30.0	9	42.4	8.0	−57.0	84.0	701	−57.0	84.0	igneous			McElhinny et al. (1968)	635	T12
Tasmanian dolerite	179.0	187.0	183.0	−42.0	147.5	21	38.3	5.2	−50.7	174.5	801	−59.0	68.2	igneous			Schmidt and McDougall (1977)	1113	T12
Ferrar dolerites, Northern Prince Albert Mountains	179.0	187.0	183.0	−74.5	342.0	15	59.5	5.5	−47.8	225.5	802	−71.4	85.7	igneous			Lanza and Zanella (1993)	2721	T12
Stormberg lavas (Lesotho basalts), South Africa	179.0	187.0	183.0	−29.3	28.6	47	32.6	3.7	−71.6	93.5	701	−71.6	93.5	igneous			Kosterov and Perrin (1996)	3090	T12
Marifil Formation, North Patagonia, Argentina	178.0	188.0	183.0	−44.8	−65.6	10	19.2	11.3	−83.0	138.0	290	−53.3	90.1	igneous			Iglesia Llanos et al. (2003)	3535	T12
Lesotho basalts	179.0	187.0	183.0	−29.4	27.8	15	15.2	10.1	−63.7	88.5	701	−63.7	88.5	igneous			Prévot et al. (2003)		this study
Scania basalts	178.0	191.0	184.5	55.5	14.0	21	16.4	8.1	−69.0	283.0	301	−63.2	84.8	igneous			Bylund and Halvorsen (1993)	2720	T12
Diabase dykes and sills, Liberia	183.5	188.1	185.8	6.5	349.5	25	31.0	5.3	−68.5	62.4	714	−67.3	67.4	igneous			Dalrymple et al. (1975)	140	T12
Marangudzi Ring Complex, Zimbabwe	183.0	189.0	186.0	−22.1	30.7	8	47.5	8.1	−70.7	106.7	701	−70.7	106.7	igneous			Brock (1968)	470	T12

Table 2 (*continued*)

Name	Age$_{min}$	Age$_{max}$	Age	Slat	Slon	N	K	A$_{95}$	Plat	Plon	PlateID	Rlat	Rlon	Lithology	f	p$_{std}$	Authors	Refno	DB
Combined dikes	189.0	193.0	191.0	46.8	294.0	8	36.4	9.3	−74.9	256.0	101	−67.6	87.8	igneous			Hodych and Hayatsu (1988)	1932	T12
Kerforne dykes, France	190.0	196.0	193.0	48.3	355.5	7	36.0	10.2	−61.3	258.8	301	−75.4	87.8	igneous			Sichler and Perrin (1993)	2743	T12
Freetown Complex, Sierra Leone	190.0	196.0	193.0	8.3	346.8	13	55.8	5.6	−82.9	32.7	714	−82.4	48.7	igneous			Hargraves et al. (1999)	3287	T12
Piedmont dikes	190.0	198.0	194.0	34.5	278.5	20	24.5	6.8	−67.9	275.3	101	−63.0	68.7	igneous			Dooley and Smith (1982)	1796	T12
French Guyana dikes, Brazil	190.3	200.3	195.3	3.5	307.5	26	50.7	4.0	−81.2	235.1	201	−63.6	72.7	igneous			Nomade et al. (2000)	3378	T12
Cassipore dykes, Brazil	192.7	202.0	197.4	2.5	308.5	17	48.0	5.2	−79.8	208.6	201	−65.5	82.3	igneous			Ernesto et al. (2003)		this study
Roraima dykes, CAMP, Brazil	197.4	201.1	199.3	2.1	−63.3	7	84.6	6.6	−80.1	235.0	201	−64.6	71.7	igneous			Ernesto et al. (2003)		this study
Ighrem and Foum Zguid dykes, Morocco	198.0	202.0	200.0	30.2	7.5	23	55.0	4.1	−73.0	64.7	707	−72.4	68.8	igneous			Palencia-Ortas et al. (2011)		T12
North Mountain basalt	199.5	201.4	200.5	45.3	295.3	9	26.0	10.3	−66.4	251.9	101	−71.9	68.9	igneous			Hodych and Hayatsu (1988)	1932	T12
Hartford basin	199.6	202.0	200.8	42.0	287.4	315	12.9	2.3	−66.6	268.2	101	−65.4	66.7	sedimentary	0.5	1.15	Kent and Olsen (2008)		T12
Morrocan Intrusives, Morocco	199.0	203.0	201.0	32.0	352.5	27	16.7	7.0	−71.0	36.0	707	−71.0	40.3	igneous			Bardon et al. (1973)	148	T12
Central Atlantic Magmatic Province, Morocco	199.0	203.0	201.0	31.2	7.3	5	16.9	19.1	−73.0	61.3	707	−72.5	65.5	igneous			Knight et al. (2004)		T12
Argana Flows. Morocco	199.0	203.0	201.0	30.7	350.8	13	48.0	6.0	−69.2	55.5	707	−68.8	59.2	igneous			Ruiz-Martínez et al. (2012)		T12
Central Atlantic Magmatic Province, Morocco	199.0	203.0	201.0	31.4	7.5	99	31.4	2.6	−60.0	61.6	707	−59.5	64.2	igneous			Font et al. (2011)		this study
Newark Martinsville core	199.3	209.5	204.4	40.6	285.4	302	8.8	2.9	−67.8	276.1	101	−62.3	70.1	sedimentary	0.5	1.45	Kent and Tauxe (2005)		T12
Newark Westonville	205.4	208.6	207.0	40.2	285.4	246	10.6	2.9	−66.6	266.5	101	−66.0	67.2	sedimentary	0.5	1.43	Kent and Tauxe (2005)		T12
Gipsdalen and Fleming Fjord Formations	207.0	211.0	209.0	71.5	337.3	222	16.1	2.4	−52.5	279.0	102	−67.6	36.5	sedimentary	0.5	4.95	Kent and Tauxe (2005)		T12
Andesites, Ukraine	202.6	217.7	210.2	47.3	37.4	12	47.9	6.3	−50.0	286.4	301	−66.4	40.7	igneous			Yuan et al. (2011)		T12
Newark Somerset core	208.6	213.4	211.0	40.5	285.4	309	17.0	2.0	−61.7	275.3	101	−61.6	57.1	sedimentary	0.6	1.0	Kent and Tauxe (2005)		T12
Newark Rutgers core	213.0	215.0	214.0	40.5	285.6	336	31.0	1.4	−60.1	277.1	101	−60.3	54.5	sedimentary	0.7	0.7	Kent and Tauxe (2005)		T12
Newark Titusville core	215.0	219.0	217.0	40.3	285.1	308	23.2	1.7	−59.9	279.5	101	−59.2	54.9	sedimentary	0.6	0.83	Kent and Tauxe (2005)		T12
Newark Nursery core	218.5	224.0	221.0	40.3	285.2	194	17.3	2.5	−60.5	281.6	101	−58.4	56.7	sedimentary	0.4	1.23	Kent and Tauxe (2005)		T12
Dan River–Danville Basin	217.0	225.0	221.0	36.5	280.5	333	25.2	1.6	−59.0	279.6	101	−58.8	53.3	sedimentary	0.5	0.76	Kent and Tauxe (2005)		T12
Newark Princeton core	221.0	233.0	227.0	40.4	285.4	148	34.6	2.0	−54.2	286.6	101	−53.2	48.7	sedimentary	0.6	1.03	Kent and Tauxe (2005)		T12
Taimyr Sills, Siberia	227.0	229.2	228.1	74.8	100.6	11	74.7	5.3	−47.1	301.6	301	−57.8	39.2	igneous			Walderhaug et al. (2005)		T12
Gezira, Egypt	224.0	234.0	229.0	22.3	33.6	10	75.5	5.6	−54.6	46.2	715	−55.1	46.0	igneous			Lotfy and Elaal (2018)		this study
Dolerite dykes, Suriname	227.0	237.0	232.0	4.0	305.0	10	61.3	6.2	−82.0	320.0	201	−52.7	66.4	igneous			Veldkamp et al. (1971)	701	T12
Udzha, Siberian Platform	232.0	245.0	238.5	71.4	115.3	18	10.5	11.2	−60.3	332.4	301	−46.3	70.7	igneous			Veselovskiy et al. (2012)		this study

Table 2 (*continued*)

Name	Age$_{min}$	Age$_{max}$	Age	Slat	Slon	N	K	A$_{95}$	Plat	Plon	PlateID	Rlat	Rlon	Lithology	f	p$_{std}$	Authors	Refno	DB
Alto Paraguay Province, Paraguay/Brazil	240.2	242.8	241.5	−21.5	−57.9	26	23.0	6.0	−78.0	319.0	201	−51.1	60.5	igneous			Ernesto et al. (2015)		this study
Brisbane Tuffs	237.0	247.1	242.1	−27.47	153.0	6	31.7	12.1	−56.5	153.1	801	−46.3	59.1	igneous			Robertson (1963)		this study
Puesto Viejo Formation Volcanics, Mendoza	235.3	254.7	245.0	−34.6	−68.3	14	30.6	7.3	−76.7	312.4	290	−48.6	58.5	igneous			Domeier et al. (2011b)		T12
Taimyr basalts, Siberia	242.5	254.5	248.5	74.9	100.5	10	12.0	14.5	−59.3	325.8	301	−49.0	67.4	igneous			Walderhaug et al. (2005)		T12
Kotuy River Siberian Traps, Siberia	248.4	251.6	250.0	73.0	102.4	5	31.0	13.9	−52.7	328.4	301	−44.8	59.6	igneous			Veselovsky et al. (2003)		T12
Siberian Traps Mean recalculated, Siberia	248.4	251.6	250.0	66.1	111.6	5	19.5	17.7	−52.8	334.4	301	−41.8	62.3	igneous			Kravchinsky et al. (2002)		T12
Siberian Traps, YG locality	250.4	252.4	251.4	64.0	115.0	9	36.2	8.7	−65.2	320.9	301	−52.9	75.3	igneous			Konstantinov et al. (2014)		this study
Siberian Traps, Nizhneudinsk-Octyabrskiy group	250.4	252.4	251.4	56.8	99.4	9	14.9	13.8	−44.5	329.1	301	−40.0	50.6	igneous			Latyshev et al. (2018)		this study
Siberian Traps, Tura lavas	250.4	252.4	251.4	56.8	99.4	12	11.5	13.4	−45.5	312.8	301	−50.2	42.9	igneous			Latyshev et al. (2018)		this study
Siberian Traps, RD locality	250.4	252.4	251.4	63.5	112.5	19	15.4	8.8	−53.0	313.5	301	−53.1	54.1	igneous			Konstantinov et al. (2014)		this study
Kulumber river intrusions, Siberia	250.4	252.4	251.4	68.9	86.4	33	13.4	7.1	−47.4	323.1	301	−45.1	50.7	igneous			Latyshev et al. (2021b)		this study
Siberian Traps, Nizhnyaya Tunguska river	250.4	252.4	251.4	64.6	94.4	35	24.5	5.0	−56.2	313.6	301	−54.1	59.2	igneous			Latyshev et al. (2018)		this study
Siberian Traps, Norilsk-Maymecha-Kotuy	250.4	252.4	251.4	70.0	90.0	49	23.2	4.3	−52.9	327.1	301	−45.6	59.3	igneous			Pavlov et al. (2019)		this study
Norils region intrusions, Siberia	251.3	252.3	251.8	69.3	88.5	31	24.7	5.3	−54.5	320.8	301	−49.7	59.0	igneous			Latyshev et al. (2021a)		this study
East European Platform, Zhukov	246.7	259.5	253.1	56.2	42.6	106	17.3	3.4	−53.2	349.5	301	−34.7	69.5	sedimentary	0.9	3.0	Fetisova et al. (2017)		this study
East European Platform, Puchezh	246.7	259.5	253.1	57.0	43.2	157	19.7	2.6	−41.0	326.3	301	−39.6	45.3	sedimentary	0.9	3.0	Fetisova et al. (2017)		this study
East European Platform, Oskii S″ezd	246.7	259.5	253.1	56.2	44.0	108	8.7	4.9	−59.6	322.1	301	−50.9	66.8	sedimentary	0.4	3.0	Fetisova et al. (2018)		this study
Araguainha impact structure, Brazil	252.2	257.2	254.7	−16.8	−53.0	28	83.5	3.6	−84.2	326.6	201	−53.0	70.2	igneous			Yokoyama et al. (2014)		this study
East European Platform, Sukhona	251.9	259.5	255.7	61.0	45.0	210	13.9	2.7	−49.2	345.9	301	−33.8	64.0	sedimentary	0.7	3.0	Fetisova et al. (2018)		this study
East European Platform, Nelben	251.9	259.5	255.7	51.7	11.7	82	34.5	2.7	−57.3	341.7	301	−40.7	70.3	sedimentary	0.7	3.0	Fetisova et al. (2018)		this study
SW England, Aylesbeare Mudstone	254.2	264.3	259.3	50.6	−3.4	81	22.4	3.4	−65.6	325.9	301	−50.9	76.7	sedimentary	0.49	3.82	Hounslow et al. (2017)		this study
Gonfaron 1, Lodeve	259.4	264.3	261.9	43.3	6.3	118	69.1	1.6	−54.0	348.9	301	−35.5	70.0	sedimentary	0.8	0.97	Evans et al. (2014)		this study
Sierra Chica, La Pampa	261.0	264.6	263.0	−37.5	−65.3	35	54.9	3.3	−80.1	349.0	290	−44.8	68.6	igneous			Domeier et al. (2011a)		T12
Upper Choiyoi Group, Mendoza	261.5	265.5	263.5	−34.7	−68.3	40	31.4	4.1	−73.7	315.6	290	−46.6	55.0	igneous			Domeier et al. (2011b)		T12
Gerrigong Volcanics	263.5	265.1	264.3	−34.6	150.8	17	16.3	9.1	−56.9	154.8	801	−47.2	58.5	igneous			Belica et al. (2017)		this study
Werrie Basalt	263.4	269.4	266.4	−31.9	151.0	9	10.8	16.4	−61.2	128.7	801	−34.9	49.7	igneous			Klootwijk (2003)		this study
Tambillos, Uspallate Basin, Argentina	259.6	274.4	267.0	−32.2	290.5	16	33.5	6.5	−78.9	319.6	290	−48.2	62.4	igneous			Rapalini and Vilas (1991)	2475	T12

Table 2 (*continued*)

Name	Age$_{min}$	Age$_{max}$	Age	Slat	Slon	N	K	A$_{95}$	Plat	Plon	PlateID	Rlat	Rlon	Lithology	f	p$_{std}$	Authors	Refno	DB
Lunner dikes, Norway	268.3	274.7	271.0	60.3	10.5	8	103.8	5.5	−52.9	344.4	301	−36.9	66.8	igneous			Torsvik et al. (1988)	3188	T12
Lunner dikes, Norway	268.3	274.7	271.0	60.3	10.5	25	68.7	3.5	−50.9	343.6	301	−36.0	64.5	igneous			Dominguez et al. (2011)		T12
Dome de Barrot, France	269.2	274.4	271.8	44.0	6.6	206	41.8	1.5	−47.2	324.5	301	−44.2	51.2	sedimentary	1	0	Haldan et al. (2009)		this study
Lodeve basin redbeds	264.3	283.3	273.8	43.7	3.4	146	33.3	2.1	−41.7	336.7	301	−33.9	52.1	sedimentary	0.8	0.79	Haldan et al. (2009)		this study
Bohemian Massif igneous, Germany	275.0	280.0	277.5	49.8	12.0	9	65.4	6.4	−42.3	345.9	301	−29.2	58.0	igneous			Soffel and Harzer (1991)	2356	T12
Scania melaphyre dikes, Sweden	274.0	282.0	278.0	55.7	13.7	8	35.9	9.4	−54.0	351.5	301	−34.3	71.2	igneous			Bylund (1974)	2222	T12
Jebel Nehoud Ring Complex, Kordofan, Sudan	278.0	282.0	280.0	14.9	30.5	8	102.7	5.5	−40.8	71.3	715	−41.2	71.2	igneous			Bachtadse et al. (2002)	3504	T12
Trachytes, Ukraine	280.0	285.2	282.6	37.2	37.8	19	54.9	4.6	−49.4	359.7	301	−27.4	71.4	igneous			Yuan et al. (2011)		T12
Exeter Lavas, UK	280.0	291.0	285.5	51.0	356.0	9	62.5	6.6	−48.0	343.0	301	−34.5	61.4	igneous			Cornwell (1967)	411	T12
Western Meseta, Morocco	277.0	294.6	285.8	33.0	353.6	18	27.1	6.8	−41.4	52.1	707	−41.1	53.9	igneous			Domeier et al. (2021)		this study
Black Forest volcanics, Germany	281.0	291.0	286.0	48.0	8.0	7	82.1	6.7	−51.6	359.6	301	−29.1	73.1	igneous			Konrad and Nairn (1972)	170	T12
Mauchline lavas, Scotland	279.0	293.0	286.0	55.5	−4.6	5	36.4	12.8	−46.2	348.0	301	−30.8	62.5	igneous			Harcombe-Smee et al. (1996)	3093	T12
Mount Leyshon Intrusive Complex, Australia	280.0	292.0	286.0	−20.3	146.3	34	16.4	6.3	−43.2	137.3	801	−33.0	72.2	igneous			Clark and Lackie (2003)		this study
Tuckers Igneous Complex, Australia	280.0	292.0	286.0	−20.1	146.5	42	11.5	6.8	−47.5	143.0	801	−38.3	69.2	igneous			Clark and Lackie (2003)		this study
NE Kazakhstan lavas 1	282.8	289.8	286.3	47.5	80.7	65	48.8	2.5	−33.2	338.2	301	−27.3	45.8	igneous			Bazhenov et al. (2014)		this study
NE Kazakhstan lavas 2	283.8	290.8	287.3	47.5	80.7	88	48.0	2.2	−44.1	340.6	301	−33.3	56.5	igneous			Bazhenov et al. (2016)		this study
Oslo Graben, Krokskogen and Vestfold	284.0	292.0	288.0	59.4	10.2	104	52.2	1.9	−48.2	335.5	301	−38.6	57.8	igneous			Haldan et al. (2014)		this study
Lodeve basin redbeds	283.3	293.5	288.4	43.7	3.4	143	98.2	1.2	−47.1	333.9	301	−38.9	55.9	sedimentary	0.8	0.68	Haldan et al. (2009)		this study
Saar–Nahe volcanics, Germany	288.0	293.0	290.5	49.5	7.0	11	20.8	10.2	−41.1	349.2	301	−26.6	59.0	igneous			Berthold et al. (1975)	712	T12
Nahe volcanics, Germany	288.0	293.0	290.5	50.0	8.0	5	104.8	7.5	−46.0	347.0	301	−31.2	61.8	igneous			Nijenhuis (1961)	940	T12
Itarare Group, Parana Basin, Brazil	283.3	298.9	291.1	−27.2	310.4	119	32.7	2.3	−63.2	347.5	201	−34.4	55.2	sedimentary	0.8	6.0	Franco et al. (2012)		this study
Scania dolerite dikes, Sweden	287.0	300.0	293.5	55.5	13.5	6	85.6	7.3	−37.0	354.0	301	−21.1	58.9	igneous			Mulder (1971)	2211	T12
Alnwick Sill, High Green and St. Oswalds Chapel Dyke (Whin Sill), UK	292.0	296.0	294.0	55.4	−1.6	17	47.1	7.7	−47.1	337.1	301	−37.1	57.5	igneous			Liss et al. (2004)		T12
Holy Island Sill and Dyke (Whin Sill), UK	292.0	296.0	294.0	55.7	−1.8	20	36.2	5.5	−35.4	346.8	301	−23.9	53.1	igneous			Liss et al. (2004)		T12

Table 2 (*continued*)

Name	Age$_{min}$	Age$_{max}$	Age	Slat	Slon	N	K	A$_{95}$	Plat	Plon	PlateID	Rlat	Rlon	Lithology	f	P$_{std}$	Authors	Refno	DB
Silesia volcanics, Poland	285.0	305.0	295.0	50.6	16.1	8	41.0	8.8	−43.0	354.0	301	−25.5	63.3	igneous			Birkenmajer et al. (1968)	465	T12
Glenshaw Formation	298.9	307.0	303.0	40.5	280.0	23	16.1	7.8	−27.9	294.5	101	−31.0	27.6	sedimentary	0.7	0.58	Kodama (2009)		T12
Mafra Formation, Brazil	298.9	307.0	303.0	−26.1	310.2	111	55.9	1.8	−51.9	344.3	201	−25.4	47.0	sedimentary	1	0.0	Brandt et al. (2019)		this study
Moscovian, Murzuq basin, Algeria	307.0	315.2	311.1	23.6	11.9	113	25.4	2.7	−22.3	53.5	715	−22.8	53.1	sedimentary	0.6	3.1	Amenna et al. (2014)		this study
Tashkovska Donbas, Ukraine	315.2	323.4	319.3	48.8	38.6	84	35.4	2.6	−38.4	339.5	301	−30.1	50.9	sedimentary	0.7	1.7	Meijers et al. (2010)		T12
Newcastle range volcanics	315.6	328.2	321.9	−18.4	143.8	15	26.2	7.6	−63.4	125.0	801	−33.9	45.9	igneous			Anderson et al. (2003)	3561	T12
Magdalen Basin	315.2	330.3	322.8	46.2	298.7	262	12.4	2.6	−27.9	299.5	101	−28.3	31.6	sedimentary	0.60	1.5	Opdyke et al. (2014)		this study

authors only provided the grand mean paleomagnetic direction, we used the mean sampling location to determine the position of the associated paleopole. We have listed the statistical parameters that underlie our sampling approach in Table 2, which include the number of sites, the Fisher precision parameter K and the A$_{95}$ cone of confidence about the paleopole. These parameters were either obtained from the original publication or from other reported statistical parameters from which the missing values may be determined. If the number of sites and either the Fisher precision parameter K or the 95% cone of confidence (A$_{95}$) is provided, the other parameter was calculated if it was not reported (see e.g., Ch. 11 in Tauxe et al., 2010). For studies in which Fisher statistics have been applied to the site-level paleomagnetic directions instead of the VGPs – yielding a mean paleomagnetic direction with an $\alpha95/k$ and an elliptical confidence region on the paleopole described by the parameters dp/dm (e.g., Butler, 1992) - we use the analytical formula of Cox (1970) to convert the *k* (and associated a95) to K (and A95), after estimating the paleolatitude using the reported mean paleomagnetic inclination (see Deenen et al. (2011) for more details).

For each paleomagnetic dataset, we have listed an age range that describes the uncertainty of the age determination of the sampled rocks, whereby we mostly follow the age assignment of the original authors. This may correspond to the uncertainty of an individual radiometric age, to the mean computed from multiple radiometric age determinations, or to a certain age interval from which the rocks are derived. For bio-stratigraphically or magnetostratigraphically dated sediments, we have updated the numerical ages using the most recent geological timescale, of Gradstein et al. (2020), which was also used for the plate model. When new age constraints were available, we have updated the ages of individual database entries, e.g., for data from LIPs. We emphasize here that not all age determinations are without controversy and that there are likely revised age determinations that we were not aware of during the compilation of our database. Finally, we note that additional details on the age determination, statistical parameters and the dominant lithology of the sampled rocks are provided in the extended database in Table S2.

5.2. Selection criteria

We applied a number of selection criteria during the compilation of the paleomagnetic datasets that were used for construction of the global APWP. First, we re-compiled the data that were included in the compilation of Torsvik et al. (2012) from the original publications. We excluded data for which evidence was reported that it does not represent a reliable estimate of the time-averaged field at the time of formation of the sampled rocks, as concluded by the original authors or by others in more recent work that evaluated that particular dataset. We also rejected datasets for which no modern demagnetization techniques were used, as is common procedure (Van der Voo, 1990a; Meert et al., 2020). In addition, we removed duplicates: in some cases, the paleomagnetic data used to compute a paleopole that was included in the Torsvik et al. (2012) database were also used (and combined with other or newer data) to compute more recently published paleopoles. Reasons for exclusion are provided in Table S2 and include, for instance, evidence for remagnetization or unremoved magnetic overprints, local or regional vertical-axis rotations, erroneous structural corrections, or poor age control. We note that paleomagnetic datasets that were not originally compiled by Torsvik et al. (2012) and that did not satisfy the above criteria, were immediately rejected, and are not included in Table 2.

We then applied the following criteria to all paleomagnetic datasets:

1) We exclude datasets derived from <5 sites that are interpreted as independent spot readings of the past geomagnetic field. This number is essentially arbitrary but establishing whether such small datasets accurately represent PSV is difficult, and in our site-level computation of the APWP, the impact of such small datasets is negligible. We do not require that sites are based on averages of multiple samples, as this was shown to have minor effects on paleopole position or precision

(Gerritsen et al., 2022).

2) We exclude paleomagnetic datasets from igneous rocks if their A_{95} values fall outside of the N-dependent reliability envelope of Deenen et al. (2011). This criterion evaluates whether the dispersion of VGPs is consistent with what may be expected from secular variation. If the reported A_{95} cone of confidence of the paleopole falls outside of the $A_{95, \text{ min-max}}$ reliability envelope, this suggests that the dataset is likely affected by one or more sources of additional scatter that are unrelated to PSV (if $A_{95} > A_{95, \text{ max}}$), or that PSV was insufficiently sampled by the dataset (if $A_{95} < A_{95, \text{ min}}$), for instance, due to the limited temporal coverage of the sampled sites (see Deenen et al. (2011) for a detailed explanation).

3) We only include sediment-derived datasets whereby the paleopole and statistical parameters were calculated from a collection of paleomagnetic directions that approximately represent independent readings of the past geomagnetic field, and whereby these directions were corrected for potential inclination shallowing. To select such datasets, we use the reliability criteria formulated by Vaes et al. (2021), which assess under which conditions sedimentary datasets may be reliably corrected for inclination shallowing by the E/I correction, while satisfying the underlying assumption of that method that each of the paleomagnetic directions may be considered an independent reading of the past geomagnetic field. We only include E/I-corrected sedimentary datasets that would receive a grade 'A' or 'B' according to the evaluation scheme of Vaes et al. (2021). In addition, we have included two datasets that satisfy these criteria but were corrected for inclination shallowing using an anisotropy-based approach (Kodama, 2009; Brandt et al., 2019). We note that these criteria for sedimentary rocks are far more stringent than in previous compilations for the computation of APWPs, and only 29 sediment-derived datasets are used in the computation of the global APWP.

4) As a final selection criterion, we only include datasets with an age uncertainty range of <20 Ma: datasets with larger age uncertainties would lead to needless smoothing of the global APWP.

6. Results

We computed a global APWP for the last 320 Ma using a 10 Ma time interval and a 20 Ma sliding window. The APWP is based on a total of 13,737 simulated VGPs that are derived from 350 different paleomagnetic datasets (Table 2), yielding a mean and median number of sites per dataset of ~39 and 19, respectively. Of these datasets, 162 were included in the compilation of Torsvik et al. (2012), 71 in the PSV10 database (Cromwell et al., 2018) and 117 were added during our data compilation (most of which were published post-2011).

The new global APWP is shown in Fig. 5 as reference poles per 10 Ma that are plotted as south poles in South African coordinates (see also Table 3). The global APWP in the coordinate frame of other major tectonic plates, including North America, South America, Eurasia, India, Australia, Antarctica and the Pacific is given in Table 4. Because the simulated VGPs are not necessarily evenly distributed around the center age of the sliding window, we also report the average age of the simulated VGPs behind each reference pole in Table 3. In the following, we describe the geometry and statistical parameters of the global APWP as calculated for a South African coordinate frame (see also Figs. 5 and 6).

The reference poles of the global APWP in South African coordinates plot along smooth path segments intervened by sharp cusps (Fig. 5). The APWP shows a relatively smooth path from the present back to an Early Cretaceous (140 Ma) cusp that was also observed in previous global APWPs in South Africa coordinates (Besse and Courtillot, 2002; Schettino and Scotese, 2005; Torsvik et al., 2008, 2012). The reference poles of the 140–230 Ma segment of the APWP form another relatively smooth path, except for the 170 Ma pole which defines a minor 'kink' in the path. Notably, the reference poles at 230 and 240 Ma (Early Triassic) show a large angular difference of ~10.4°. This is in large contrast to the 250 and 260 Ma reference poles which are separated by only ~0.8° and
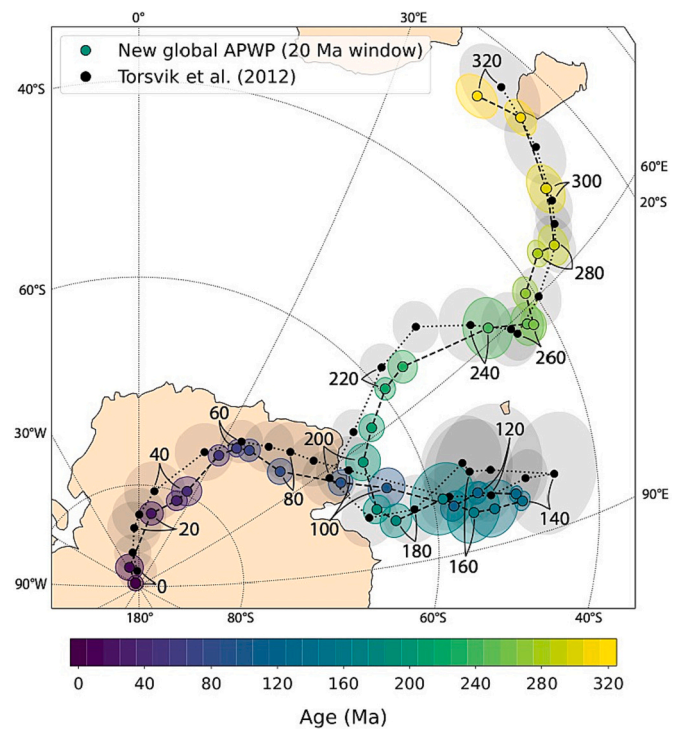
Fig. 5. Orthographic plot of the new global APWP for the last 320 Ma in South African coordinates, calculated using a 20 Ma sliding window. Reference poles and 95% confidence regions are colored by their age. Global APWP of Torsvik et al. (2012) is plotted with black circles (and light grey A95 confidence circles). Numbers indicate the center age of the time windows and are shown per 20 Ma.

define another 'cusp' in our global APWP. The oldest (320–260 Ma) part of the APWP forms two segments that are separated by a kink defined by the 290 Ma reference pole, although we note that the oldest 320–300 Ma segment has the largest uncertainties of our APWP.

The 95% confidence regions of the global APWP are defined by the circle that includes 95% of the *pseudo*-poles computed for 2000 iterations (the P_{95}). The size of the confidence regions ranges from 0.7° to 3.5° (for the 0 and 170 Ma reference poles, respectively), with an average (and standard deviation) of 1.6° (0.7°) (Table 3). The reference poles of the APWP are computed from, on average, 813 parametrically simulated VGPs. The lowest data density is observed for the Late Jurassic, with only ~110–150 sites per time window. As expected, the highest data density is obtained for the last 10 Ma, provided by the large number of sites included in the PSV10 dataset. Additionally, the early Cenozoic (50–60 Ma) and Late Triassic (200–220 Ma) segments of the APWP are also based on large datasets of simulated VGPs.

For each time window, we computed the mean values of the Fisher precision parameter (K), the circular standard deviation (CSD) and elongation (E) for each iteration from the distribution of simulated VGPs that were included in that window (Table 3, Fig. 6b). The values for K are on average 20.9, ranging between 12.4 and 34.7. We obtain an average angular standard deviation for all time windows of 18.3°, with minimum and maximum values of 13.8° and 23.1°. The elongation ranges from 1.07 to 1.42 (Table 3), with an average value of 1.16, indicating that the distribution of simulated VGPs that fall within the same time window is approximately circularly symmetric (see also Fig. 2a).

We calculated the rate of apparent polar wander per 10 Ma time period from the great-circle distance between reference poles of successive age (Fig. 6a). We obtain an average APW rate of 0.40 ± 0.21°/ Ma (one standard deviation). Except for a notable spike in APW rate of 1.04°/Ma between 230 and 240 Ma and two peaks of ~0.8°/Ma at 100–110 Ma and 300–310 Ma, all APW rates are ~0.6°/Ma or lower.

Table 3

Global APWP for the last 320 Ma in South African coordinates, calculated using a 20 Ma window. The center age of the window and the mean age of the re-sampled VGPs in that window are listed. N and P$_{95}$ are the average number of re-sampled VGPs that fall within the time window and the 95% confidence region of the reference pole (in degrees). Mean K, CSD and E are the average Fisher (1953) precision parameter, circular standard deviation and elongation of the re-sampled VGPs.

Window	Age	N	P$_{95}$	Longitude	Latitude	Mean K	Mean CSD	Mean E
0	1.3	1811.5	0.7	313.2	−89.6	19.1	18.5	1.07
10	4.4	2609.7	1.3	334.1	−87.9	17.8	19.2	1.06
20	21.7	1156.7	1.1	9.4	−82.7	17.0	19.7	1.10
30	28.2	1091.0	1.0	23.2	−80.8	17.9	19.1	1.09
40	37.5	475.0	1.4	26.1	−79.6	19.6	18.3	1.14
50	56.1	1101.3	1.0	31.0	−75.2	16.3	20.1	1.11
60	60.0	1707.5	0.8	35.2	−73.7	16.4	20.0	1.08
70	64.7	896.5	1.1	39.1	−73.1	17.5	19.4	1.12
80	82.0	350.1	1.3	51.5	−72.6	29.9	14.8	1.16
90	89.7	412.9	1.2	64.9	−68.2	25.5	16.1	1.17
100	94.6	217.3	1.9	71.5	−64.2	22.8	17.0	1.21
110	114.7	259.5	1.5	80.7	−57.9	29.6	14.9	1.26
120	120.2	458.1	1.1	80.0	−55.0	29.3	15.0	1.18
130	131.0	798.2	0.8	82.7	−50.7	33.6	14.0	1.10
140	134.2	621.8	0.9	84.1	−50.0	34.7	13.8	1.12
150	152.4	144.3	2.8	83.7	−53.4	17.5	19.4	1.24
160	158.7	148.9	3.0	83.1	−55.8	14.6	21.2	1.24
170	172.6	112.5	3.5	78.6	−58.9	14.7	21.2	1.28
180	182.1	319.5	1.7	79.5	−64.2	19.0	18.6	1.29
190	189.7	470.1	1.4	75.3	−65.8	18.9	18.7	1.18
200	203.7	1399.0	1.8	63.5	−65.4	12.4	23.1	1.09
210	209.7	2287.7	1.3	58.1	−62.9	14.8	21.0	1.06
220	217.5	1583.0	1.1	53.8	−59.5	22.2	17.2	1.07
230	224.4	543.6	1.6	53.1	−56.7	23.0	16.9	1.12
240	242.5	215.4	2.9	58.3	−46.8	14.5	21.4	1.21
250	253.3	1017.2	2.1	61.7	−42.7	13.5	22.1	1.08
260	257.2	1200.3	1.6	62.4	−42.1	15.6	20.5	1.08
270	268.6	637.2	1.6	58.5	−41.0	26.6	15.7	1.13
280	281.3	819.1	1.3	56.2	−36.9	28.4	15.2	1.11
290	288.4	763.9	2.0	57.0	−34.6	28.4	15.2	1.18
300	297.8	405.8	2.5	52.1	−30.8	25.1	16.2	1.26
310	311.1	368.0	1.9	45.3	−26.6	18.6	18.8	1.42
320	320.3	427.9	2.4	39.8	−28.2	13.6	22.0	1.33

There seems to be no clear correlation between the APW rate and age, and age bins with relatively low APW rates alternate with slightly faster APW throughout the studied time span of the pole path. On the other hand, the observed APW rates and position of the reference poles may be influenced by an uneven temporal distribution of the simulated VGPs. For example, a large dataset with relatively tight age constraints may 'pull' a reference pole towards the paleopole with large N. This temporal bias may be identified from a relatively large difference between the center age of the window and the mean age of the simulated VGPs that fall within that time window (see Fig. 6c). For example, the high APW rate between 230 and 240 Ma may be explained by the difference in mean age of the simulated VGPs of ~18 Ma. To correct for this effect, we have also computed the APW rates between successive reference poles by dividing their angular distance by the difference in mean age of the simulated VGPs (Fig. 6a). In this calculation, we do not account for the uncertainty associated with these mean ages, which are found to be small (on average, the 95% confidence bounds are ±0.27 Ma). Although the average APW rate (with one standard deviation) remains similar (0.42 ± 0.18°/Ma), all the peaks in APW rate mentioned above disappear. Instead, we now observe a single peak in the APW rate of 0.8–1.0°/Ma between 82 to ~95 Ma. Whether the observed spikes in APW rate are robust features of our global APWP will be discussed in section 7.2.

7. Discussion

7.1. Robustness of the global APWP

Our approach to compute a global APWP from site-level paleomagnetic data critically builds on the assumption that the dominant sources of uncertainty in paleomagnetism are (more) effectively averaged by assigning equal weight to each paleomagnetic site rather than to a paleopole that is an average of an arbitrary collection of those sites (Vaes et al., 2022). On the one hand, our approach allows us to straightforwardly propagate uncertainties in the age of the sampled rocks and the uncertainty caused by paleosecular variation of the past magnetic field. On the other hand, there are multiple sources of uncertainty and error that are independent of the number of sites, e.g., due to unremoved magnetic overprints or remagnetization, dating errors, or non-rigidity of assumed rigid plates. Besse and Courtillot (2002) suspected that because some degree of deformation is often necessary for rocks to be exposed at the surface, unrecognized local deformation (such as local rotations caused by plunging fold axes) may be an important source of noise in APWPs. In the conventional approach in which each paleopole is assigned equal weight, the bias resulting from a single dataset that is affected by one or more of the above artifacts is unlikely to be large. However, if such a dataset has a large number of sites, its relatively large weight may cause considerable bias in the APWP calculated from site-level data.

We first evaluate the influence of large datasets on the global APWP by parametrically re-sampling only 50 VGPs for all paleomagnetic datasets that are based on >50 sites. The resulting APWP is very similar to the one presented in the previous section (Fig. 7). As expected, the confidence regions for many reference poles are larger, as they are based on fewer sites. We observe two main differences. First, we observe that the reference poles with time windows centered at 50 and 70 Ma are at a larger angular distance from the 60 Ma reference pole, as they are pulled less towards the larger number of simulated VGPs derived from paleopoles with ages of ~60 Ma. Second, the 240–300 Ma segment of the APWP becomes a smoother path. This shows that although no major differences are observed, large datasets indeed alter some segments of the APWP. However, since we do not know the 'true' APWP, it is difficult to assess whether the influence of a large datasets represents a bias in the

Table 4

Global APWP (20 Ma window) rotated into the coordinate frame of other major tectonic plates. Each pole position is obtained by rotating the poles listed in Table 3 with an Euler rotation pole computed for its effective age using the global plate circuit (Table S1). Plon/Plat = pole longitude and latitude.

Window	Age	P95	North America		South America		Eurasia		India		Australia		Antarctica		Pacific		Iberia	
			Plon	Plat	Plon	Plat	Plon	Plat	Plon	Plat	Plon	Plat	Plon	Plat	Plon	Plat	Plon	Plat
0	1.3	0.7	311.7	−89.5	291.0	−89.5	297.9	−89.5	65.7	−89.9	155.5	−89.6	292.4	−89.5	241.7	−89.4	297.9	−89.5
10	4.4	1.3	331.3	−87.8	315.2	−88.0	321.4	−87.8	21.5	−88.9	110.4	−89.3	317.0	−87.9	268.1	−88.3	321.4	−87.8
20	21.7	1.1	355.6	−82.2	326.9	−84.6	348.7	−83.5	69.2	−81.4	102.2	−80.6	343.3	−84.3	270.6	−85.8	350.6	−83.4
30	28.2	1.0	4.9	−80.8	334.4	−84.4	0.6	−82.6	84.2	−77.3	105.6	−75.8	357.0	−84.0	262.2	−86.5	5.9	−82.4
40	37.5	1.4	358.1	−80.2	319.4	−83.7	350.2	−82.5	98.9	−73.5	113.2	−71.7	346.2	−84.2	241.2	−83.5	357.8	−82.0
50	56.1	1.0	2.0	−75.8	326.6	−81.1	348.4	−79.8	96.2	−58.5	114.4	−68.5	354.2	−83.9	226.3	−78.1	7.2	−78.8
60	60.0	0.8	7.1	−74.5	337.2	−80.8	354.2	−79.3	96.3	−52.5	112.9	−66.8	9.4	−83.8	220.6	−78.3	14.3	−77.8
70	64.7	1.1	10.5	−74.1	343.1	−81.1	357.0	−79.5	99.4	−44.5	114.2	−65.6	20.0	−84.4	209.6	−76.6	20.6	−77.6
80	82.0	1.3	9.4	−77.2	328.2	−84.3	351.9	−81.7	104.4	−30.5	127.6	−63.4	130.8	−89.8	186.3	−63.7	34.4	−78.7
90	89.7	1.2	18.4	−77.7	9.9	−85.6	0.9	−83.0	111.5	−23.3	130.4	−58.9	147.9	−85.7				
100	94.6	1.9	24.9	−76.1	39.0	−83.2	17.4	−82.5	113.8	−18.1	130.7	−55.5	142.3	−82.7				
110	114.7	1.5	16.7	−75.8	66.5	−83.8	5.8	−81.4	115.9	−10.3	143.7	−52.2	181.6	−77.4				
120	120.2	1.1	11.7	−74.4	66.3	−85.6	3.7	−79.6	114.6	−8.2	145.8	−52.2	187.8	−76.8				
130	131.0	0.8	7.3	−71.8	69.1	−85.4	4.3	−76.5	116.1	0.1	146.4	−46.9	179.3	−72.8				
140	134.2	0.9	8.0	−72.0	66.4	−83.9	4.7	−76.7	117.8	1.9	147.2	−45.2	178.6	−71.2				
150	152.4	2.8	347.2	−74.4	89.7	−86.7	337.9	−75.6	125.8	−2.9	161.5	−44.6	199.4	−64.5				
160	158.7	3.0	332.0	−75.8	137.6	−87.8	322.1	−74.6	128.5	−5.5	167.1	−44.5	205.7	−61.8				
170	172.6	3.5	299.2	−73.8	221.2	−86.5	300.7	−69.0	130.0	−9.9	173.4	−45.8	213.9	−59.5				
180	182.1	1.7	274.8	−73.7	215.1	−81.2	283.6	−66.7	133.8	−14.6	181.8	−45.0	220.3	−54.6				
190	189.7	1.4	268.0	−71.0	224.5	−79.4	280.2	−63.7	133.1	−17.0	184.3	−46.7	224.4	−54.5				
200	203.7	1.8	268.1	−65.1	247.2	−77.4	287.1	−58.7	128.6	−19.8	185.2	−51.6	231.8	−57.1				
210	209.7	1.3	273.0	−62.5	262.4	−76.9	293.9	−56.8	125.0	−19.7	182.6	−54.6	234.9	−60.1				
220	217.5	1.1	278.5	−59.5	278.6	−75.8	302.1	−54.7	120.8	−19.0	178.2	−57.7	238.3	−63.8				
230	224.4	1.6	283.2	−58.1	289.9	−75.4	307.5	−53.7	118.3	−17.4	173.4	−59.0	238.8	−66.6				
240	242.5	2.9	301.7	−55.8	330.2	−74.4	324.8	−52.9	113.4	−8.4	154.2	−57.0	222.3	−75.5				
250	253.3	2.1	310.1	−55.1	346.6	−73.0	332.7	−53.0	112.5	−3.7	147.4	−54.1	203.6	−77.6				
260	257.2	1.6	311.5	−55.0	349.2	−72.7	334.0	−53.0	112.4	−3.0	146.6	−53.5	199.9	−77.7				
270	268.6	1.6	309.6	−52.1	343.8	−70.2	333.0	−50.0	109.5	−4.1	143.6	−56.1	207.1	−80.5				
280	281.3	1.3	312.1	−48.0	345.9	−65.8	336.4	−46.2	105.4	−2.4	135.7	−56.9	196.1	−84.8				
290	288.4	2.0	315.2	−46.8	350.1	−64.2	339.6	−45.3	104.3	−0.2	132.1	−55.5	168.6	−85.3				
300	297.8	2.5	314.3	−41.2	346.5	−58.8	339.8	−39.7	98.7	−0.4	122.9	−57.8	72.4	−87.5				
310	311.1	1.9	311.9	−34.1	341.3	−52.1	338.5	−32.4	91.4	−1.8	109.8	−60.9	20.4	−81.4				
320	320.3	2.4	306.0	−32.4	333.2	−50.8	333.0	−30.1	89.4	−6.6	106.9	−65.9	354.2	−78.7				
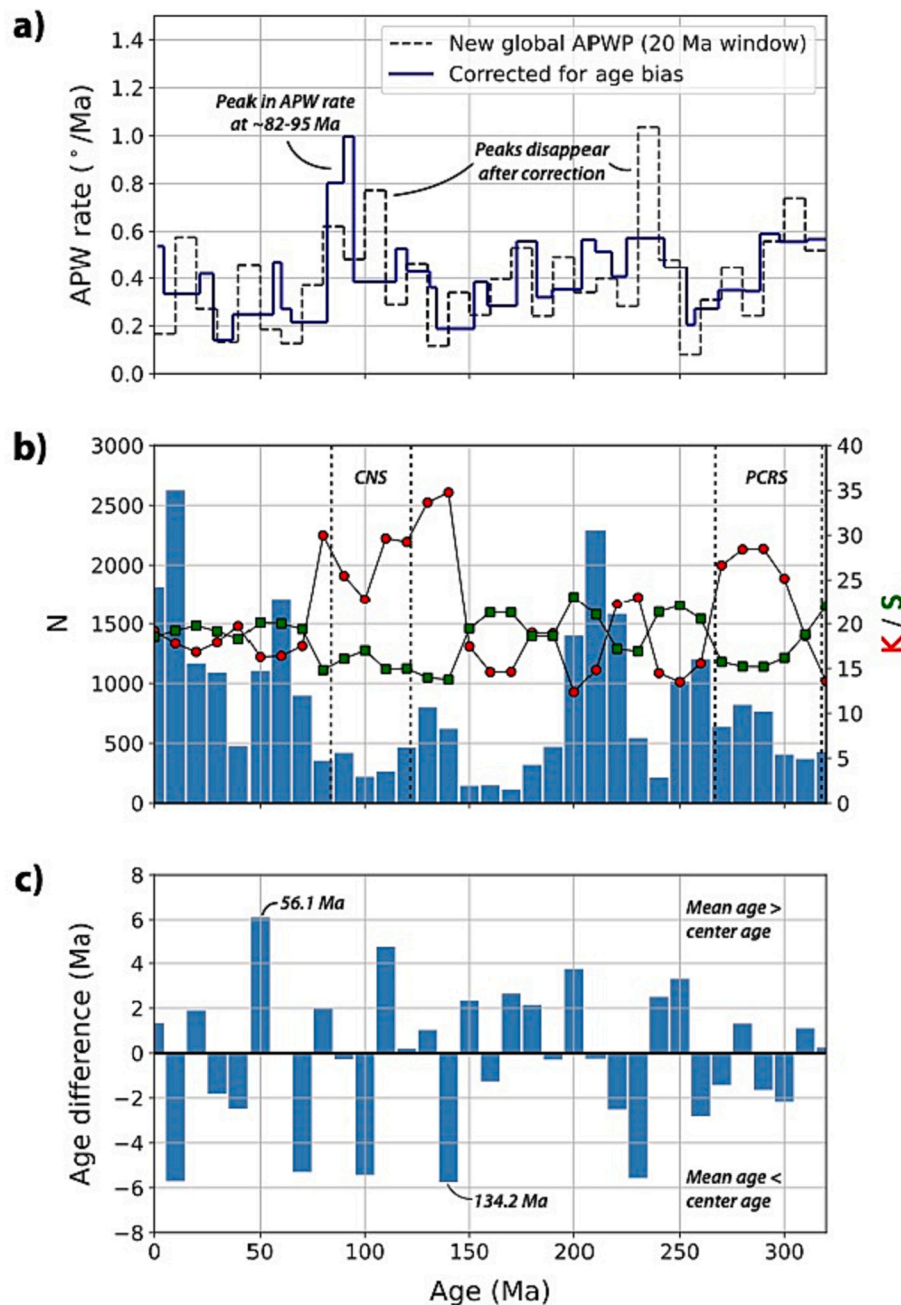
Fig. 6. a) APW rates derived from the new global APWP per 10 Ma age interval (black, dashed line). Rates computed using the mean ages of the *pseudo*-VGPs are shown by the blue line. **b)** Mean number of sites (N), K and VGP dispersion (S) of the *pseudo*-VGPs that fall within each time window. The age range of the Cretaceous Normal Superchron (CNS) and Permo-Carboniferous Reversed Superchron (PCRS) are indicated. **c)** Age difference between the mean age of the *pseudo*-VGPs and the center age of the time window. (For interpretation of the references to colour in this figure legend, the reader is referred to the web version of this article.)

path or provides improved constraints on the position of the 'true' time-average pole. The most straightforward way of testing the robustness of these features of the global APWP is by collecting more large high-quality datasets for these time intervals.

In addition, we evaluate the new global APWP using a set of statistical parameters that describe the distribution of the simulated VGPs per time window (see Table 4, Fig. 6b). The dispersion of the simulated VGPs – as quantified by K or CSD – is shown to be similar to what may be expected from 'normal' PSV. Typical values for K range from 10 to 70 (e. g., Deenen et al., 2011; Meert et al., 2020) and for CSD (or VGP scatter, S) from 10 to 25 (e.g., Butler, 1992; Cromwell et al., 2018; Doubrovine et al., 2019). The mean K and CSD values obtained for each time window of the global APWP all fall within these ranges (Fig. 6b). In addition, the mean elongation of the simulated VGPs that fall within each age bin show that the re-sampled VGPs have a nearly circular symmetric distribution (Table 3), similar to what may be expected from PSV (e.g.,

Tauxe and Kent, 2004). Interestingly, the time intervals with the lowest dispersion of pseudo-VGPs approximately coincide with the Cretaceous Normal Superchron (~83–121 Ma, Gradstein et al., 2020) and Permo-Carboniferous Reversed Superchron (~267–318 Ma, Gradstein et al., 2020). Even though these dispersion values are not obtained from real VGP-level data, we hypothesize that this lower dispersion may reflect a suppression in the magnitude of PSV during these intervals with stable magnetic field polarity, as was previously proposed (e.g., Brandt et al., 2019; Handford et al., 2021). We note, however, that the lowest dispersion of simulated VGPs is observed for the age windows centered at 130 and 140 Ma, whereby the majority of the input data is derived from large igneous datasets of South America and southern African that are associated with the Parana-Etendeka LIP. This low dispersion of simulated VGPs may be explained by the fact that the data is obtained from rocks of a relatively short age interval and is likely less affected by noise resulting from unrecognized local deformation or plate
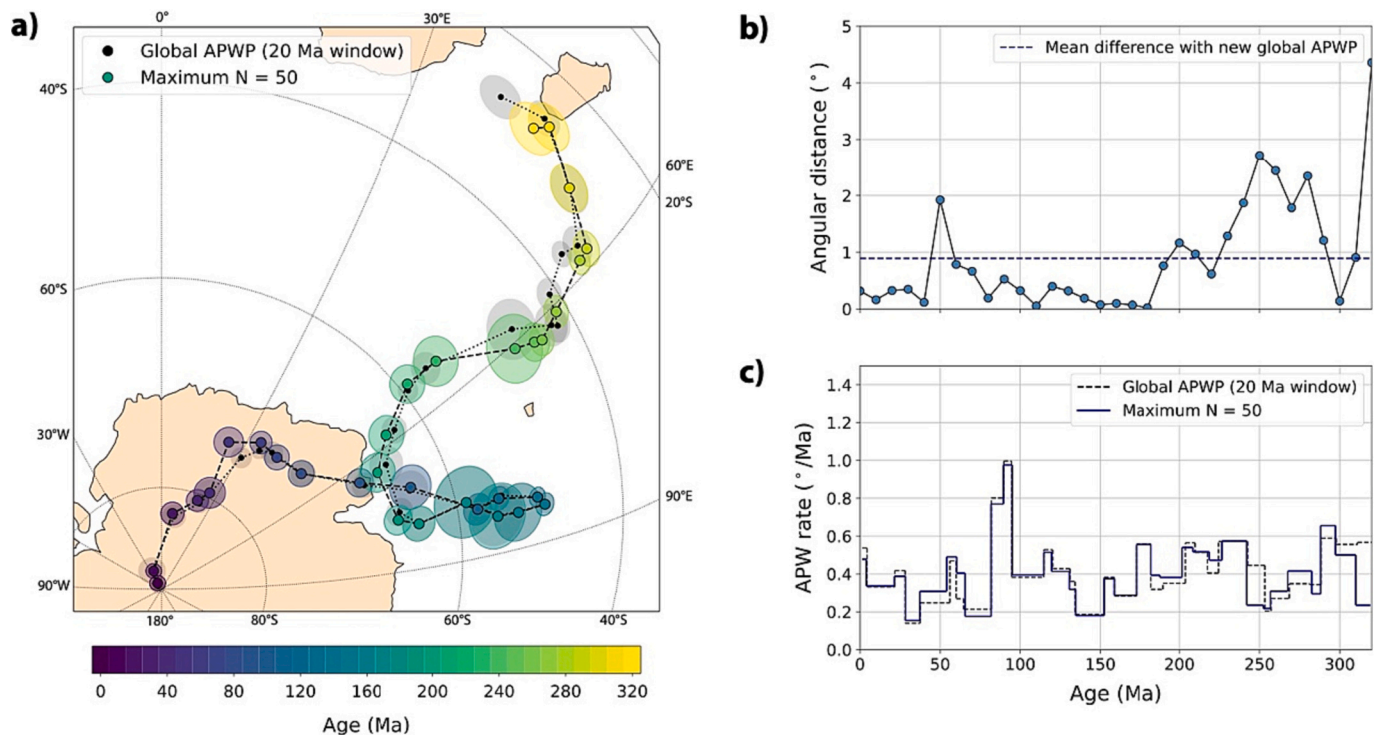
Fig. 7. a) Global APWP calculated with a maximum of *N* = 50 per dataset. The global APWP of Fig. 5 is plotted with the black circles. **b)** Angular difference between the two APWPs shown in (a). **c)** Comparison of APW rates of these two APWPs.

reconstruction errors.

In summary, the statistical parameters obtained for the global APWP indicate that the dispersion of simulated VGPs used to compute the APWP is similar to that what would be expected from PSV alone. This shows that the errors that undoubtedly exist in our dataset due to e.g., unresolved overprints, unrecognized tectonic deformation, plate circuit errors, or age errors, do not form a major contribution to the scatter of the simulated VGPs that fall within the same time window, which would drive the dispersion beyond values that typically represent PSV and/or lead to an elongation of the distribution of simulated VGPs. This suggests that the global APWP presented here is robust and that it represents the time-averaged paleomagnetic field for each interval.

7.2. Comparison to previous global APWPs

Because of the fundamentally different approach used here, it is interesting to evaluate how the site-level-based path compares to previous global APWPs that were computed using the conventional running mean approach applied to paleopoles. We find that our new global APWP has a mean angular difference (with one standard deviation) of $2.5 \pm 1.1°$ when compared to the global APWP of Torsvik et al. (2012) (Fig. 8a). This difference is similar to the mean angular difference of 2.6° between the global APWP (in South African coordinates) of Besse and Courtillot (2002) and Torsvik et al. (2012), but notably smaller than the difference between the APWP of Torsvik et al. (2012) and those of Torsvik et al. (2008) and Kent and Irving (2010), which yielded average angular differences of 3.9° and 4.1°, respectively. These APWPs were all computed using the same running mean approach with a time step of 10 Ma and a sliding window of 20 Ma, and the observed differences thus resulted from differences between the compilations of paleopoles and plate reconstruction parameters. But even though we constructed our path using (i) simulated VGPs instead of paleopoles, (ii) an updated paleomagnetic database obtained with more stringent selection criteria and (iii) an updated global plate circuit, we obtain a path that is, to first-order, similar to the most recent pole-based APWP of Torsvik et al.

(2012) (see Fig. 5a). This clearly shows that the overall geometry of the path is well-constrained, and strengthens confidence that paleomagnetism provides a reliable and reproducible reference frame as basis for paleogeography and paleoclimate for the last 320 Ma.

One of the main differences between our VGP-based APWP and the pole-based APWP of Torsvik et al. (2012) is the size of the 95% confidence regions (Fig. 5a). Particularly for time intervals with high data density, such as for the Cenozoic, Early Cretaceous and Late Triassic, the confidence regions of the new global APWP are <1.5°, compared to A_{95} values of ~2–3° of the Torsvik et al. (2012) path for those intervals. The smaller confidence regions may seem surprising, since the approach used for the VGP-based path incorporates both temporal and spatial uncertainties that were set to zero in the computation of the APWP of Torsvik et al. (2012). We interpret this as simply the result of the significant increase in data points from dozens of paleopoles to hundreds or even thousands of simulated VGPs. The increase in independent data points thus outweighs the larger dispersion of simulated VGPs (with a K of ~15–35) compared to that of coeval paleopoles (with K values of ~100, see Rowley, 2019; Vaes et al., 2022). The smaller confidence regions obtained from using site-level data instead of paleopoles was previously observed for the PSV10 dataset by Vaes et al. (2022). This suggests that the resolution and precision obtained with paleomagnetic data has long been underestimated by artificially decreasing the number of data points underlying APWPs due to the averaging of arbitrarily defined collections of sites into paleopoles.

Although the first-order geometry of our new global APWP is similar to that of Torsvik et al. (2012), there are several time intervals for which there are notable differences. For instance, the reference poles of the 30–40, 90–100 and 310–320 Ma segments of the path, as well as the poles at 200 and 230 Ma, are at an angular distance of >3° (Fig. 8a). We interpret these differences as being mainly caused by our site-level approach and the updated paleomagnetic database, to which we added recently published data but from which we also excluded many paleomagnetic datasets due to the application of our more stringent selection criteria. In addition, we note that differences in the effective
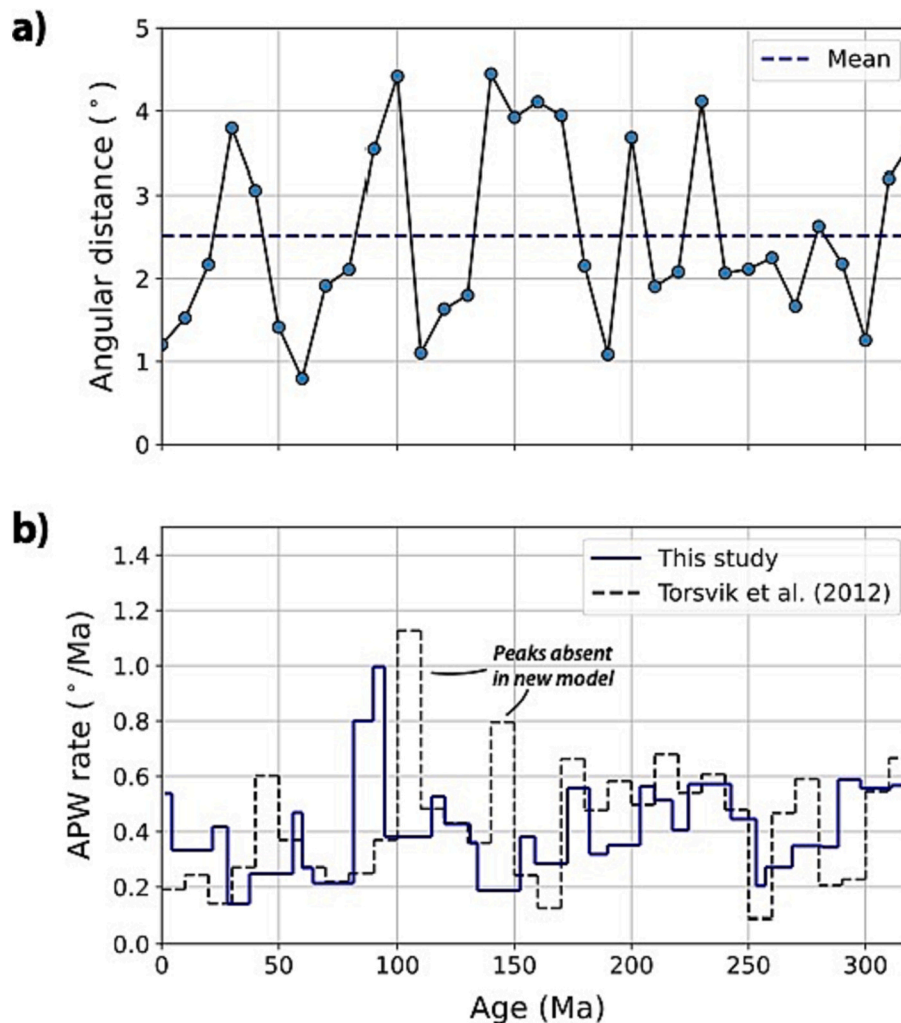
Fig. 8. a) Angular difference between the new VGP-based global APWP and the pole-based APWP of Torsvik et al. (2012), both in South African coordinates. The dashed blue line is the mean angular distance of 2.5°. **b)** APW rates determined in this study compared to those derived from the global APWP of Torsvik et al. (2012). (For interpretation of the references to colour in this figure legend, the reader is referred to the web version of this article.)

age of the reference poles computed for the same time window may contribute to observed differences in pole position.

The largest difference between our new global APWP and that of Torsvik et al. (2012) is observed for the 140–170 Ma segment, yielding an angular difference of ~4° (Fig. 5, 8a). This segment of the APWP of Torsvik et al. (2012) was based on relatively few paleopoles (<20 per time window), and the observed differences may partly be explained by the inclusion of recently published datasets in our database, e.g., those from Cervantes-Solano et al. (2020) and Kulakov et al. (2021). Despite these differences, our new APWP is similar to that of Torsvik et al. (2012) in that it does not include a phase of rapid polar wander between ~165 and 140 Ma as shown in the APWP of Kent and Irving (2010). This rapid polar shift is often referred to as the 'Jurassic monster polar shift' and has been interpreted as fast true polar wander (e.g., Kent et al., 2015; Muttoni and Kent, 2019; Yi et al., 2019). Our new global APWP does not support such anomalously fast polar wander in the Late Jurassic, consistent with recently published paleomagnetic results (Kulakov et al., 2021; Gao et al., 2021). We note, however, that our APWP does not rule out the occurrence of a phase of relatively 'slow' TPW in the late Jurassic.

Another notable difference is the ~4° angular distance between our reference pole at 100 Ma and that of Torsvik et al. (2012), yielding a very different estimate of the APW rate at mid-Cretaceous times. The 110–100 Ma spike in APW rate observed by Torsvik et al. (2012) is much

less pronounced in our global APWP and disappears entirely when correcting for the 'effective' age difference between successive reference poles (Fig. 8b). We find that the simulated VGPs that fall in the age windows centered on 100 Ma and 110 Ma have mean ages of ~95 Ma and ~ 115 Ma, respectively (Fig. 6c, Table 3), indicating that the spike in uncorrected APW rate may be the result from an uneven age distribution of the input data. This suggests that previous estimates of APW rate based on the center ages of each time window may be influenced by temporal biases and shows the importance of taken into account the uncertainties in ages and their distribution.

Intriguingly, after applying a correction for the effective age difference between successive reference poles, the APW rates calculated for South Africa for the last 320 Ma show only a single spike at ~82–95 Ma. Although a detailed analysis of this phase of rapid APW is beyond the scope of this paper, we note that this spike coincides with a ~ 80–92 Ma peak in the convergence rate during a counterclockwise rotation of Africa relative to Eurasia, as part of a recently proposed tectonic chain reaction (Gürer et al., 2022). The spike in APW rate observed in our APWP may thus be related to a phase of relatively rapid plate motion of (South) Africa.

Finally, we note that there are a number of previously inferred and long-debated 'anomalies' in paleomagnetic data, such as those between the major continents of Gondwana, Laurentia, and Baltica for ~320–250 Ma which underpin the Pangea A vs B controversy (e.g.,

Domeier et al., 2012, 2021; Gallo et al., 2017; Kent and Muttoni, 2020, Kent et al., 2021; Pastor-Galán, 2022), or the 'east Asian inclination anomaly' in the Paleogene (e.g., Cogné et al., 2013). The observed mismatches between paleomagnetic data and APWPs of different continents and tectonic plates have generally been based on analyses using pole-level data. These discrepancies may be re-evaluated using a site-level approach, in which spatial and temporal uncertainties are explicitly incorporated, which have often been omitted in comparative analyses. Evaluating whether previously inferred anomalies still exist when using our site-level approach requires a detailed review of the underlying data, which is beyond the scope of this paper. We note, however, that there is no systematic increase in the dispersion of simulated VGPs that underlie our site-based global APWP in the time intervals of the long-standing debates. We thus find no reason to infer a significant error in the relative plate motion model in these time intervals (e.g., Muttoni et al., 2003; Cogné et al., 2013), or a systematic time-dependent non-dipole field (e.g., Torsvik and van der Voo, 2002; Dupont-Nivet et al., 2010).

7.3. Resolution of the global APWP

We calculated the reference poles of the global APWP at a resolution of 10 Ma using a sliding window of 20 Ma, similar to previously published global APWPs of Besse and Courtillot (2002), Kent and Irving (2010) and Torsvik et al. (2008, 2012). The use of such overlapping time windows results in the smoothing of the pole path and is expected to increase the extent to which random biases and noise in the underlying data are averaged. On the other hand, too much smoothing could cause the removal of short-duration features in the APWP that may be real (e.g., Muttoni et al., 2005; Dupont-Nivet et al., 2010), as illustrated, for instance, by the spherical spline path of Torsvik et al. (2008) that smoothed 'away' a peak in APW rate. To assess the influence of the temporal resolution on the shape of the global APWP, we also computed the path at a higher resolution, using a time step of 5 Ma and a sliding window of 10 Ma (Fig. 9). The geometry of the path is notably more irregular than the APWP calculated using a 20 Ma sliding window,

showing more distinct features such as relative standstills and cusps that separate segments of the path covering shorter time intervals. For example, while the 10 Ma-resolution-APWP showed a relative smooth path for the last 140 Ma, the 5 Ma-resolution-APWP shows a relative stand-still during the 30–50 Ma interval (Fig. 9a). For time intervals with relatively high APW rates, such as from 180 to 230 Ma, the 5 Ma-resolution-path is nearly identical to the 10 Ma-resolution-path. This finding is consistent with that of Besse and Courtillot (2002) who also computed their global APWP at a 5 Ma resolution (with a 10 Ma window) and who illustrated the large similarities between both paths in the coordinate frame of the relatively fast-moving Indian plate, noting that all the 'essential' features were captured by both paths. The use of a smaller time window leads to a decrease in the degree of smoothing of the path, resulting in ~40% higher APW rates with an average of $0.58 \pm 0.30°/$ Ma (after correcting for the effective age) and seven intervals of 5 Ma that yield an APW rate of $>1.0°$/Ma (Fig. 9b). Notably, the peak in APW rate observed for the 10 Ma-resolution-APWP between 82 and ~ 95 Ma is also identified for the 5-Ma-resolution-APWP, which shows a ~ $1.2°/$ Ma APW rate between 86 and ~ 94 Ma.

The reference poles of the 5 Ma-resolution-APWP are, unsurprisingly, based on about half as many simulated VGPs ($N = 417$ versus $N = 813$) compared to the 10 Ma-resolution-APWP. Notably, ~17% of the reference poles have a mean number of sites of <100 (see Fig. 9c, Table S3). The reduced number of simulated VGPs behind each reference pole leads to larger confidence regions that have an average (and standard deviation) of $2.5°$ ($1.2°$) compared to $1.6°$ ($0.7°$) for the 10 Ma-resolution-APWP (Fig. 9a). Intriguingly, the distribution of simulated VGPs shows a very similar mean dispersion, with a K value of 22.2 for the 5 Ma-resolution-APWP compared to 20.9 for the 10 Ma-resolution-APWP, further supporting that the distributions of simulated VGPs underpinning our global APWP provide a robust approximation of the dispersion expected from PSV (Fig. 9c). But because of the lower number of simulated VGPs per time window, the APWP and associated APW rates are more likely to be biased by random noise or an uneven temporal distribution of the simulated VGPs.
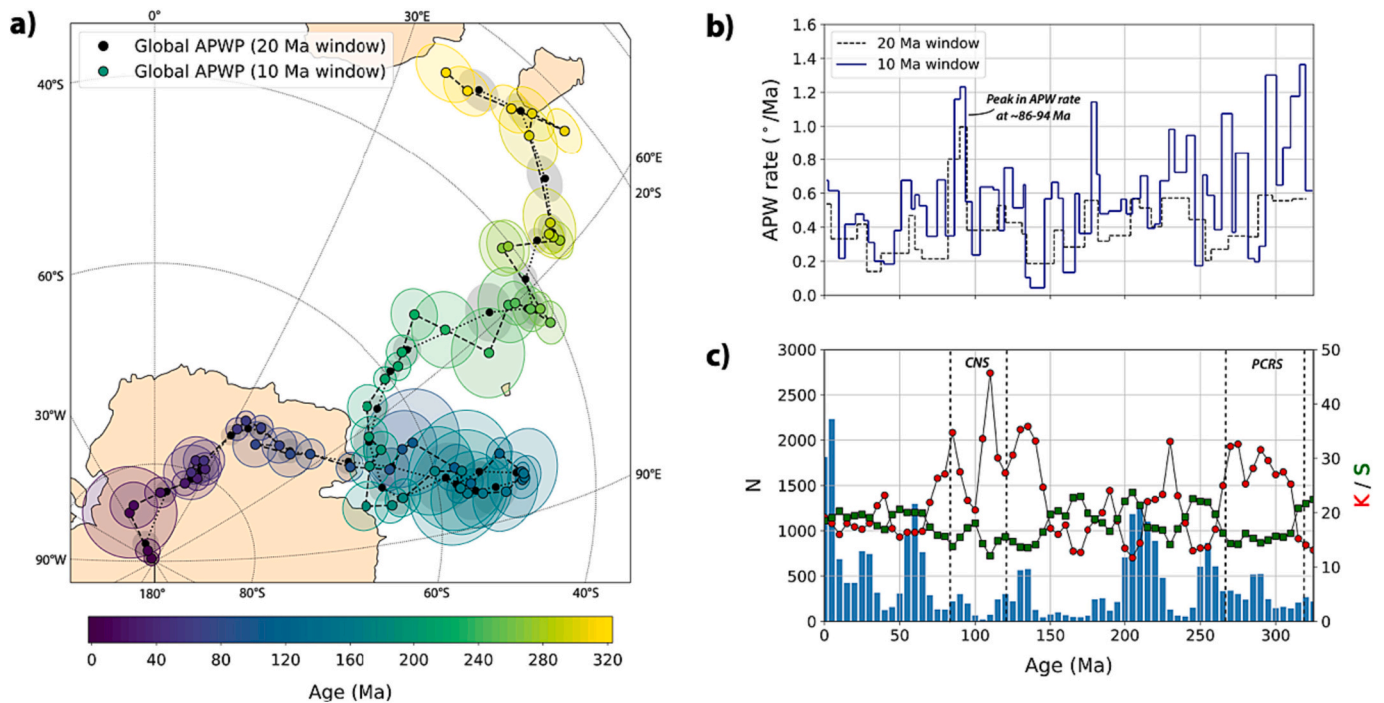
Fig. 9. a) Global APWP for the last 325 Ma (in South African coordinates) computed at a 5 Ma resolution with a 10 Ma window. The path calculated using a 20 Ma window is plotted with the black circles. **b)** Comparison of APW rates of the two APWPs shown in a). **c)** Statistical parameters for the 5 Ma-resolution-APWP; see Fig. 6 for more information.

7.4. Outlook

The calculation of a global APWP based on simulated VGPs provides a next step in the propagation of key sources of uncertainty in the computation of APWPs, building on previous efforts and approaches aimed to incorporate uncertainties in paleopoles or APWPs (e.g., McFadden and McElhinny, 1995; Swanson-Hysell et al., 2019; Hansma and Tohver, 2020; Gallo et al., 2021; Vaes et al., 2022; Pierce et al., 2022). Future improvements in the propagation of errors may concentrate on some of the following aspects. First, errors in the Euler rotation poles that are used to rotate the simulated VGPs to a common coordinate frame are not yet propagated. Although methods have been developed to propagate such uncertainties throughout a plate circuit (Doubrovine and Tarduno, 2008), the uncertainties of many Euler rotation poles computed from ocean floor anomalies have not been reported and the size of error ellipses of marine magnetic anomaly-derived are typically an order of magnitude smaller than uncertainties induced by PSV (e.g., DeMets and Merkouriev, 2021). We foresee that the propagation of these errors will provide only marginal gains.

Second, a statistical framework for the full propagation of the errors through the hierarchical levels of paleomagnetic data, that is from the individual demagnetization steps to the VGP or paleopole - has yet to be developed. Recent advances in the statistical treatments of paleomagnetic data (Heslop and Roberts, 2016, 2020) or directional statistics (e. g., Scealy et al., 2022) may provide promising avenues for improved propagation of these fundamental uncertainties behind paleomagnetic data. Ideally, future APWPs could be computed from real site-level data rather than from simulated VGPs (e.g., Gallo et al., 2023). Such an approach would avoid the necessity of adopting a pre-defined distribution of VGPs, such as the assumed Fisher distribution used here, which is a useful but not entirely accurate approximation of the distribution of VGPs (e.g., Tauxe and Kent, 2004; Deenen et al., 2011). When using a parametric re-sampling approach, the Fisher distribution is essentially the only option, however, for the simple reason that statistical parameters describing the paleomagnetic data distributions have traditionally been reported in the framework of Fisher (1953). An important advantage of using the published site-level data is that it allows the systematic application of selection criteria and data filters on the site-level. Building the database from the real VGPs would also enable the propagation of age uncertainties that are defined at the site level, provided by numerical age determinations of individual sites as well as by relative temporal relationships between sites (Gallo et al., 2023). Temporal biases in VGP-based APWPs, caused by an uneven distribution of VGP ages, may then be mitigated by assigning more weight to sites that have an age closer to the center age of the moving time window, as recently proposed by Gallo et al. (2023). Apart from the fact that not all site-level data is available for the studies included in the data compilations that underlie global APWPs, the compilation of more than ten thousand sites from hundreds of publications would require an enormous effort. Whether the calculation of a global APWP from the published VGPs would yield different results from our re-sampling approach remains to be investigated. To enable the computation of VGP-based APWPs in the future, we strongly recommend paleomagnetists to archive their published data at the site, sample, and measurement level, e.g., in the MagIC database (Jarboe et al., 2012) or the Paleomagnetism.org data library (Koymans et al., 2020).

We emphasize that the calculation of a reference APWP from site-level data provides opportunities to significantly improve intervals of the global APWP by collecting large datasets of independent readings of the past geomagnetic field (e.g., from thick sequences of lava flows or sedimentary rocks), particularly for time intervals that have a relative low data coverage. Moreover, Dupont-Nivet et al. (2010) already argued that the precision and temporal resolution of reference APWPs provides a limiting factor in the analysis of detailed tectonic problems, such as the estimation of convergence rates between tectonic terranes that are not included in a plate circuit. They therefore tried to stimulate the paleomagnetic community to focus part of their efforts on collecting datasets from stable plate interiors that may improve the accuracy and precision of the global APWP. We suggest here that rock formations that have provided reliable paleomagnetic data in the past but that include, as of yet, only a relatively limited number of sites may provide particularly useful sampling locations for this purpose. In addition, we highlight that our new approach allows the comparison of independent paleomagnetic datasets against the global APWP at the site-level, which may improve the robustness of future determinations of relative tectonic displacements such as paleolatitudinal motions and vertical-axis rotations (see Vaes et al., 2022). Finally, we note the site-level approach holds great promise to optimize the resolution of APWPs for key time intervals, such as those containing mass extinctions or climate crises: collecting data from such well-dated intervals allows computing a high-resolution paleomagnetic reference frame that may be used as input for detailed studies of such events. We foresee that the continuous improvement of the global APWP, both in terms of data coverage and uncertainty incorporation, will enable Earth Scientists to place better quantitative constraints on, for instance, orogenic evolution, the rate and magnitude of TPW, plate tectonic reconstructions and the paleogeographical influence on paleoclimate, paleoenvironment and paleobiology.

8. Conclusions

In this study, we presented a global apparent polar wander path for the last 320 Ma calculated from simulated site-level paleomagnetic data, using an updated paleomagnetic database and relative plate motion model. Based on our new APWP, we conclude the following:

- A parametric re-sampling approach allows the straightforward incorporation of both spatial and temporal uncertainties in the paleomagnetic data, as well as uncertainty in the widely used E/I correction for inclination shallowing. Even though these uncertainties are taken into account in our approach, the 95% confidence regions of the site-level APWP are smaller than that of previously computed global APWPs because the much larger number of simulated VGPs per time window compared to the number of paleopoles in the conventional approach outweighs the larger dispersion of simulated VGPs compared to paleopoles.
- The distributions of simulated VGPs that fall within a given age bin resemble the dispersion of VGPs expected for normal geomagnetic field behavior (that is, PSV) in the last few hundred Ma. We interpret this as that there are no major sources of noise that significantly enhance the dispersion beyond expected values for PSV and that would bias the global APWP.
- The first-order geometry of the new global APWP is similar to the most recent pole-based APWP of Torsvik et al. (2012), with an average angular difference of 2.8° between the reference poles computed for the same time window. The average APW rate for South Africa is 0.38° ± 0.23° (1σ), slightly lower than the 0.43° ± 0.22° obtained by Torsvik et al. (2012). The similarity between the previous pole-based global APWP and our APWP computed from simulated site-level data, using more stringent selection criteria, an updated database and global plate model, indicates that the global APWP is robust and reproducible.
- Peaks in APW rate may result from a temporal bias in paleomagnetic data. By correcting for the mean age of the simulated VGPs that underlie each reference pole, we observe that previously identified spikes in APW rate (for South Africa) disappear, while a new peak in APW rate is identified between 100 and 80 Ma.
- The calculation of the global APWP at a higher resolution using a time step of 5 Ma and a sliding window of 10 Ma results in a more irregular path with time intervals that show standstills that alternate with segments with relatively high APW rates. We find that the data coverage is certainly high enough to compute a reliable path at this

resolution for some time intervals, but not for the entire 320–0 time period.

- Calculating APWPs from site-level data provides opportunities to significantly improve the temporal resolution and quality of the global APWP by collecting large high-quality paleomagnetic datasets from stable plate interiors, particularly from rocks derived from age intervals and/or tectonic plates that are underrepresented in the current database. Finally, we emphasize that such datasets may also contribute to future re-assessments of previously observed systematic differences between similarly aged paleomagnetic data from different tectonic plates (e.g., the Pangea controversy), or provide a better-constrained paleomagnetic reference frame for time intervals of rapid Earth system change, such as climate crises and mass extinctions.

Declaration of Competing Interest

The authors declare that they have no known competing financial interests or personal relationships that could have appeared to influence the work reported in this paper.

Data availability

No new paleomagnetic and marine magnetic anomaly data is used in this study. The paleomagnetic data compilation includes datasets from previously published peer-reviewed articles and builds on compilations by Torsvik et al. (2012) and Cromwell et al. (2018). The complete database can be found in Table S2. The global plate circuit presented in this study consists of previously published Euler rotation poles that are provided in Table S1. The calculations and analyses performed here benefitted from the functions of the freely available PmagPy software package (Tauxe et al., 2016). The Python codes used for the computation of the global APWP, its statistical parameters and the associated figures are publicly available on Github (https://https://github.com/bramvaes/GlobalAPWP) and archived on Zenodo (https://doi.org/10.5281/zenodo.8356344).

Appendix A. Supplementary data

Supplementary data to this article can be found online at https://doi.org/10.1016/j.earscirev.2023.104547.

References

Abashev, V.V., Metelkin, D.V., Mikhaltsov, N.E., Vernikovsky, V.A., Bragin, V.Y., 2018. Paleomagnetism of traps of the Franz Josef Land archipelago. Russ. Geol. Geophys. 59 (9), 1161–1181.

Abdul Aziz, H., van Dam, J., Hilgen, F.J., Krijgsman, W., 2004. Astronomical forcing in Upper Miocene continental sequences: implications for the Geomagnetic Polarity Time Scale. Earth Planet. Sci. Lett. 222 (1), 243–258. https://doi.org/10.1016/j.epsl.2004.02.018.

Abels, H.A., Aziz, H.A., Ventra, D., Hilgen, F.J., 2009. Orbital climate Forcing in Mudflat to marginal Lacustrine Deposits in the Miocene Teruel Basin (Northeast Spain). J. Sediment. Res. 79 (11), 831–847. https://doi.org/10.2110/jsr.2009.081.

Ade-Hall, J.M., Reynolds, P.H., Dagley, P., Mussett, A.E., Hubbard, T.P., 1975. Geophysical studies of North African Cenozoic volcanic areas: II. Jebel Soda, Libya. Can. J. Earth Sci. 12 (8), 1257–1263.

Ahn, H.-S., Kidane, T., Otofuji, Y.-I., Yamamoto, Y., Ishikawa, N., Yoshimura, Y., 2021. High-resolution palaeomagnetic results of ethiopian trap series from Lima Limo section: implications for the Oligocene geomagnetic field behaviour and timing of volcanism. Geophys. J. Int. 225 (1), 311–328.

Alvey, A.D., 2009. Using crustal thickness and continental lithosphere thinning factors form gravity inversion to refine plate reconstruction models for the Arctic & North Atlantic (Doctoral dissertation, University of Liverpool).

Amenna, M., Derder, M.E.M., Henry, B., Bayou, B., Maouche, S., Bouabdallah, H., Beddiaf, M., 2014. Improved Moscovian part of the Gondwana APWP for paleocontinental reconstructions, obtained from a first paleomagnetic pole, age-constrained by a fold test, from in Ezzane area in the Murzuq basin (Algeria, stable Africa). J. Afr. Earth Sci. 99, 342–352.

Anderson, K.L., Lackie, M.A., Clark, D.A., Schmidt, P.W., 2003. Paleomagnetism of the Newcastle range, northern Queensland: Eastern Gondwana in the late Paleozoic. J. Geophys. Res. Solid Earth 108 (B6).

Andriamirado, C.R., 1971. In: Recherches paléomagnétiques sur Madagascar. résultats et interprétations dans le cadre de la dislocation de la partie occidentale du Gondwana. PhD Thesis. University of Strasbourg, pp. 1–350.

Andriamirado, R., Roche, A., 1969. Etude paléomagnetique de formations volcaniques crétacées de Madagascar. CR Hebd. Séanc. Acad. Sci. Paris 269, 16–19.

Arkula, C., Lom, N., Wakabayashi, J., Rea-Downing, G., Qayyum, A., Dekkers, M.J., van Hinsbergen, D.J., 2023. The forearc ophiolites of California formed during trench-parallel spreading: kinematic reconstruction of the western USA Cordillera since the Jurassic. Earth Sci. Rev. 237, 104275.

Bachtadse, V., Zänglein, R., Tait, J., Soffel, H.C., 2002. Palaeomagnetism of the Permo/Carboniferous (280 Ma) Jebel Nehoud ring complex, Kordofan, Central Sudan. J. Afr. Earth Sci. 35 (1), 89–97.

Bardon, C., Bossert, A., Hamzeh, R., WestphalL, M., 1973. Paleomagnetic study on formation of Triassic and Jurassic of Morocco and Sahara. Comptes Rendus Hebdomadaires des Seances de l'Acadeia des Sciences Serie D 276 (16), 2357–2360.

Bazhenov, M.L., Van der Voo, R., Meert, J.G., Levashova, N.M., Ipat'eva, I.S., 2014. Late Paleozoic geomagnetic-field estimates from studies of Permian lavas in northeastern Kazakhstan. Russian Geol. Geophys. 55 (1), 108–117.

Bazhenov, M.L., Van der Voo, R., Menzo, Z., Dominguez, A.R., Meert, J.G., Levashova, N. M., 2016. Paleomagnetism and dating of a thick lava pile in the Permian Bakaly formation of eastern Kazakhstan: Regularities and singularities of the paleomagnetic record in thick lava series. Phys. Earth Planet. Inter. 253, 5–20.

Belica, M.E., Tohver, E., Pisarevsky, S.A., Jourdan, F., Denyszyn, S., George, A.D., 2017. Middle Permian paleomagnetism of the Sydney Basin, Eastern Gondwana: Testing Pangea models and the timing of the end of the Kiaman reverse Superchron. Tectonophysics 699, 178–198.

Berthold, G., Nairn, A.E.M., Negendank, J.F.W., 1975. A palaeomagnetic investigation of some igneous rocks of the Saar-Hahe basin. N. Jb. Geol. Paliionth. Mh. 3, 134–150.

Besse, J., Courtillot, V., 1991. Revised and synthetic apparent polar wander paths of the African, Eurasian, North American and Indian plates, and true polar wander since 200 Ma. J. Geophys. Res. Solid Earth 96 (B3), 4029–4050.

Besse, J., Courtillot, V., 2002. Apparent and true polar wander and the geometry of the geomagnetic field over the last 200 Myr. Journal of Geophysical Research: SolidEarth 107 (B11), EPM-6.

Biggin, A.J., Bono, R.K., Meduri, D.G., Sprain, C.J., Davies, C.J., Holme, R., Doubrovine, P.V., 2020. Quantitative estimates of average geomagnetic axial dipole dominance in deep geological time. Nat. Commun. 11 (1), 1–9.

Bilardello, D., Kodama, K.P., 2010a. Palaeomagnetism and magnetic anisotropy of Carboniferous red beds from the Maritime Provinces of Canada: evidence for shallow palaeomagnetic inclinations and implications for North American apparent polar wander. Geophys. J. Int. 180 (3), 1013–1029.

Bilardello, D., Kodama, K.P., 2010b. Rock magnetic evidence for inclination shallowing in the early Carboniferous deer Lake Group red beds of western Newfoundland. Geophys. J. Int. 181 (1), 275–289.

Bilardello, D., Jezek, J., Kodama, K.P., 2011. Propagating and incorporating the error in anisotropy-based inclination corrections. Geophys. J. Int. 187 (1), 75–84.

Birkenmajer, K., Krs, M., Nairn, A.M., 1968. A paleomagnetic study of Upper Carboniferous rocks from the Inner Sudetic Basin and the Bohemian Massif. Geol. Soc. Am. Bull. 79 (5), 589–608.

Bono, R.K., Biggin, A.J., Holme, R., Davies, C.J., Meduri, D.G., Bestard, J., 2020. Covariant giant Gaussian process models with improved reproduction of palaeosecular variation. Geochem. Geophys. Geosyst. 21 (8) e2020GC008960.

Boschman, L.M., van Hinsbergen, D.J.J., Torsvik, T.H., Spakman, W., Pindell, J.L., 2014. Kinematic reconstruction of the Caribbean region since the early Jurassic. Earth Sci. Rev. 138, 102–136.

Brandt, D., Ernesto, M., Constable, C., Franco, D.R., Carlos Weinschutz, L., de Oliveira Carvalho Rodrigues, P., Zhao, X., 2019. New late Pennsylvanian paleomagnetic results from Paraná Basin (Southern Brazil): is the recent giant Gaussian process model valid for the Kiaman superchron? J. Geophys. Res. Solid Earth 124 (7), 6223–6242.

Brock, A., 1968. Paleomagnetism of the Nuanetsi igneous province and its bearing upon the sequence of Karroo igneous activity in Southern Africa. J. Geophys. Res. 73 (4), 1389–1397.

Bronner, A., Sauter, D., Manatschal, G., Péron-Pinvidic, G., Munschy, M., 2011. Magmatic breakup as an explanation for magnetic anomalies at magma-poor rifted margins. Nat. Geosci. 4 (8), 549–553.

Brown, L.L., Golombek, M.P., 1997. Tectonic stability of the San Luis Hills, northern Rio Grande rift, Colorado: evidence from paleomagnetic measurements. Geophys. Res. Lett. 24 (4), 473–476.

Bryan, P., Gordon, R.G., 1990. Rotation of the Colorado Plateau: an updated analysis of paleomagnetic poles. Geophys. Res. Lett. 17 (10), 1501–1504.

Bull, J.M., DeMets, C., Krishna, K.S., Sanderson, D.J., Merkouriev, S., 2010. Reconciling plate kinematic and seismic estimates of lithospheric convergence in the Central Indian Ocean. Geology 38 (4), 307–310.

Butler, R.F., 1992. Paleomagnetism: Magnetic Domains to Geologic Terranes, Vol. 319. Blackwell Scientific Publications, Boston.

Butler, R.F., Hervé, F., Munizaga, F., Beck, M.E., Burmester, R.F., Oviedo, E.S., 1991. Paleomagnetism of the Patagonian Plateau Basalts, southern Chile and Argentina. J. Geophys. Res. Solid Earth 96 (B4), 6023–6034. https://doi.org/10.1029/90jb02698.

Bylund, G., 1974. Palaeomagnetism of dykes along the southern margin of the Baltic Shield. Geologiska Föreningen i Stockholm Förhandlingar 96 (3), 231–235.

Bylund, G., Halvorsen, E., 1993. Palaeomagnetic study of Mesozoic basalts from Scania, southernmost Sweden. Geophys. J. Int. 114 (1), 138–144.

Camps, P., Henry, B., Nicolaysen, K., Plenier, G., 2007. Statistical properties of paleomagnetic directions in Kerguelen lava flows: Implications for the late Oligocene paleomagnetic field. J. Geophys. Res. 112 (B6) https://doi.org/10.1029/2006jb004648.

Cande, S.C., Patriat, P., 2015. The anticorrelated velocities of Africa and India in the Late Cretaceous and early Cenozoic. Geophys. J. Int. 200 (1), 227–243.

Cande, S.C., Stock, J.M., 2004. Pacific—Antarctic—Australia motion and the formation of the Macquarie Plate. Geophys. J. Int. 157 (1), 399–414.

Cervantes Solano, M., Goguitchaichvili, A., Mena, M., Alva-Valdivia, L., Morales Contreras, J., Cejudo Ruiz, R., Urrutia-Fucugauchi, J., 2015. Paleomagnetic pole positions and geomagnetic secular variation from the cretaceous Ponta Grossa Dike Swarm (Brazil). Geofísica Internacional 54 (2), 167–178.

Cervantes-Solano, M., Goguitchaichvili, A., Bettucci, L.S., Morales-Contreras, J., Gogorza, C., Núñez, P., 2020. An integrated paleomagnetic and multispecimen paleointensity study from the late Jurassic Zapicán dike swarm (Uruguay). J. S. Am. Earth Sci. 104, 102815.

Cervantes-Solano, M., Goguitchaichvili, A., Bettucci, L.S., Ruiz, R.C., Calvo-Rathert, M., Ruiz-Martinez, V.C., Alva-Valdivia, L.M., 2010. Paleomagnetism of early cretaceous arapey formation (Northern Uruguay). Stud. Geophys. Geod. 54, 533–546.

Channell, J.E.T., Muttoni, G., Kent, D.V., 2022. Adria in Mediterranean paleogeography, the origin of the Ionian Sea, and Permo-Triassic configurations of Pangea. Earth Sci. Rev. 230, 104045.

Charles, N., Augier, R., Gumiaux, C., Monié, P., Chen, Y., Faure, M., Zhu, R., 2013. Timing, duration and role of magmatism in wide rift systems: Insights from the Jiaodong Peninsula (China, East Asia). Gondwana Res. 24 (1), 412–428.

Charles, N., Chen, Y., Augier, R., Gumiaux, C., Lin, W., Faure, M., Wang, Q., 2011. Palaeomagnetic constraints from granodioritic plutons (Jiaodong Peninsula): new insights on late Mesozoic continental extension in Eastern Asia. Phys. Earth Planet. Inter. 187 (3–4), 276–291.

Chauvet, F., Geoffroy, L., Guillou, H., Maury, R.C., Le Gall, B., Agranier, A., Viana, A., 2019. Eocene continental breakup in Baffin Bay. Tectonophysics 757, 170–186.

Chenet, A.-L., Courtillot, V., Fluteau, F., Gérard, M., Quidelleur, X., Khadri, S.F.R., et al., 2009. Determination of rapid Deccan eruptions across the Cretaceous-Tertiary boundary using paleomagnetic secular variation: 2. Constraints from analysis of eight new sections and synthesis for a 3500-m-thick composite section. J. Geophys. Res. 114 (B6).

Clark, D.A., Lackie, M.A., 2003. Palaeomagnetism of the early Permian Mount Leyshon intrusive complex and tuckers igneous complex, North Queensland,Australia. Geophys. J. Int. 153 (3), 523–547.

Cogné, J.P., Besse, J., Chen, Y., Hankard, F., 2013. A new late cretaceous to present APWP for Asia and its implications for paleomagnetic shallow inclinations in Central Asia and Cenozoic Eurasian plate deformation. Geophys. J. Int. 192 (3), 1000–1024.

Cornwell, J.D., 1967. Palaeomagnetism of the Exeter lavas, Devonshire. Geophys. J. Int. 12 (2), 181–196.

Cox, A., 1970. Latitude dependence of the angular dispersion of the geomagnetic field. Geophys. J. Int. 20 (3), 253–269.

Creer, K.M., Irving, E., Runcorn, S.K., 1954. The direction of the geomagnetic field in remote epochs in Great Britain. J. Geomagn. Geoelectr. 6 (4), 163–168.

Cromwell, G., Johnson, C.L., Tauxe, L., Constable, C.G., Jarboe, N.A., 2018. PSV10: a global data set for 0–10 Ma time-averaged field and paleosecular variation studies. Geochem. Geophys. Geosyst. 19 (5), 1533–1558.

Croon, M.B., Cande, S.C., Stock, J.M., 2008. Revised Pacific-Antarctic plate motions and geophysics of the Menard Fracture Zone. Geochem. Geophys. Geosyst. 9 (7).

Dagley, P., Mussett, A.E., 1981. Palaeomagnetism of the British Tertiary igneous province: Rhum and Canna. Geophys. J. Int. 65 (2), 475–491.

Dagley, P., Mussett, A.E., 1986. Palaeomagnetism and radiometric dating of the British Tertiary igneous province: muck and Eigg. Geophys. J. Int. 85 (1), 221–242.

Dagley, P., Mussett, A.E., Skelhorn, R.R., 1984. The palaeomagnetism of the Tertiary igneous complex of Ardnamurchan. Geophys. J. Int. 79 (3), 911–922.

Dagley, P., Mussett, A.E., Wilson, R.L., Hall, J.M., 1978. The British Tertiary igneous province: palaeomagnetism of the Arran dykes. Geophys. J. Int. 54 (1), 75–91.

Dalrymple, G.B., Grommé, C.S., White, R.W., 1975. Potassium-argon age and paleomagnetism of diabase dikes in Liberia: initiation of Central Atlantic rifting. Geol. Soc. Am. Bull. 86 (3), 399–411.

Das, A.K., Piper, J.D.A., Bandyopadhyay, G., Mallik, S.B., 1996. Polarity inversion in the Rajmahal lavas, north-East India: trap emplacement near commencement of the cretaceous Normal Superchron. Geophys. J. Int. 124 (2), 427–432.

Das, A., Mallik, J., Shajahan, R., 2021. Geodynamics related to late-stage Deccan volcanism: insights from paleomagnetic studies on Dhule-Nandurbar (DND) dyke swarm. J. Ind. Geophys. Union 25 (6), 28–44.

Deenen, M.H., Langereis, C.G., van Hinsbergen, D.J., Biggin, A.J., 2011. Geomagnetic secular variation and the statistics of palaeomagnetic directions. Geophys. J. Int. 186 (2), 509–520.

Demarest Jr., H.H., 1983. Error analysis for the determination of tectonic rotation from paleomagnetic data. J. Geophys. Res. Solid Earth 88 (B5), 4321–4328.

DeMets, C., Merkouriev, S., 2016. High-resolution estimates of Nubia-Somalia plate motion since 20 Ma from reconstructions of the Southwest Indian Ridge, Red Sea and Gulf of Aden. Geophys. J. Int. 207 (1), 317–332.

DeMets, C., Merkouriev, S., 2019. High-resolution reconstructions of South America plate motion relative to Africa, Antarctica and North America: 34 Ma to present. Geophys. J. Int. 217 (3), 1821–1853.

DeMets, C., Merkouriev, S., 2021. Detailed reconstructions of India-Somalia Plate motion, 60 Ma to present: implications for Somalia Plate absolute motion and India-Eurasia Plate motion. Geophys. J. Int. 227 (3), 1730–1767.

DeMets, C., Iaffaldano, G., Merkouriev, S., 2015. High-resolution Neogene and quaternary estimates of Nubia-Eurasia-North America plate motion. Geophys. J. Int. 203 (1), 416–427.

DeMets, C., Merkouriev, S., Sauter, D., 2021. High resolution reconstructions of the Southwest Indian Ridge, 52 Ma to present: implications for the breakup and absolute motion of the Africa plate. Geophys. J. Int. 226 (3), 1461–1497.

Diehl, J.F., 1991. The Elkhorn Mountains revisited: New data for the late cretaceous paleomagnetic field of North America. J. Geophys. Res. 96 (B6) https://doi.org/10.1029/91jb00959.

Diehl, J.F., Beck, M.E., Beske-Diehl, S., Jacobson, D., Hearn, B.C., 1983. Paleomagnetism of the late Cretaceous-early Tertiary north-Central Montana Alkalic Province. J. Geophys. Res. Solid Earth 88 (B12), 10593–10609. https://doi.org/10.1029/JB088iB12p10593.

Diehl, J.F., McClannahan, K.M., Bornhorst, T.J., 1988. Paleomagnetic results from the Mogollon-Datil Volcanic Field, southwestern New Mexico, and a refined Mid-Tertiary Reference Pole for North America. J. Geophys. Res. Solid Earth 93 (B5), 4869–4879. https://doi.org/10.1029/JB093iB05p04869.

Dodd, S.C., Mac Niocaill, C., Muxworthy, A.R., 2015. Long duration (> 4 Ma) and steady-state volcanic activity in the early cretaceous Paraná-Etendeka large Igneous Province: New palaeomagnetic data from Namibia. Earth Planet. Sci. Lett. 414, 16–29.

Domeier, M., Font, E., Youbi, N., Davies, J., Nemkin, S., Van der Voo, R., Torsvik, T.H., 2021. On the early Permian shape of Pangea from paleomagnetism at its core. Gondwana Res. 90, 171–198.

Domeier, M., Van der Voo, R., Tohver, E., Tomezzoli, R.N., Vizan, H., Torsvik, T.H., Kirshner, J., 2011a. New late Permian paleomagnetic data from Argentina: Refinement of the apparent polar wander path of Gondwana. Geochem. Geophys. Geosyst. 12 (7).

Domeier, M., Van der Voo, R., Tomezzoli, R.N., Tohver, E., Hendriks, B.W., Torsvik, T.H., Dominguez, A., 2011b. Support for an "A-type" Pangea reconstruction from high-fidelity late Permian and early to Middle Triassic paleomagnetic data from Argentina. J. Geophys. Res. Solid Earth 116 (B12).

Domeier, M., Van der Voo, R., Torsvik, T.H., 2012. Paleomagnetism and Pangea: the road to reconciliation. Tectonophysics 514, 14–43.

Dominguez, A.R., Van der Voo, R., Torsvik, T.H., Hendriks, B.W., Abrajevitch, A., Domeier, M., Rousse, S., 2011. The~ 270 Ma palaeolatitude of Baltica and its significance for Pangea models. Geophys. J. Int. 186 (2), 529–550.

Dooley, R.E., Smith, W.A., 1982. Age and magnetism of diabase dykes and tilting of the Piedmont. Tectonophysics 90 (3–4), 283–307.

Doubrovine, P.V., Veikkolainen, T., Pesonen, L.J., Piispa, E., Ots, S., Smirnov, A.V., et al., 2019. Latitude dependence of geomagnetic paleosecular variation and its relation to the frequency of magnetic reversals: observations from the Cretaceous and Jurassic. Geochem. Geophys. Geosyst. 20 (3), 1240–1279.

Doubrovine, P.V., Tarduno, J.A., 2008. Linking the Late Cretaceous to Paleogene Pacific plate and the Atlantic bordering continents using plate circuits and paleomagnetic data. J. Geophys. Res. 113 (B7).

Doughty, P.T., Sheriff, S.D., 1992. Paleomagnetic evidence for en echelon crustal extension and crustal rotations in western Montana and Idaho. Tectonics 11 (3), 663–671.

Duarte, A.V., Böhnel, H., Yutsis, V., 2015. Paleomagnetism of the Miocene Jantetelco Granodiorites and Tepexco Volcanic Group and inferences for crustal block rotations in Central Mexico—Reevaluation. Tectonophysics 658, 117–127.

Dupont-Nivet, G., Van Hinsbergen, D.J., Torsvik, T.H., 2010. Persistently low Asian paleolatitudes: implications for the India-Asia collision history. Tectonics 29 (5).

Ernesto, M., Bellieni, G., Piccirillo, E.M., Marques, L.S., De Min, A., Pacca, I.G., Macedo, J.W.P., 2003. Paleomagnetic and geochemical constraints on the timing and duration of the CAMP activity in northeastern Brazil. Geophysical Monograph-American Geophysical Union 136, 129–150.

Ernesto, M., Comin-Chiaramonti, P., Gomes, C.D.B., 2015. The Early Triassic magmatism of the Alto Paraguay Province, Central South America: Paleomagneticand ASM data. Open Geosci. 7 (1) https://doi.org/10.1515/geo-2015-0022.

Ernesto, M., Zaffani, L.A., Caminha-Maciel, G., 2021. New paleomagnetic data from the Paraná Magmatic Province: Brief emplacement time and tectonism. J. S. Am. Earth Sci. 106 https://doi.org/10.1016/j.jsames.2020.102869.

Evans, D.A., 2003. True polar wander and supercontinents. Tectonophysics 362 (1–4), 303–320.

Evans, M.E., Pavlov, V., Veselovsky, R., Fetisova, A., 2014. Late Permian paleomagnetic results from the Lodève, Le Luc, and Bas-Argens Basins (southern France): Magnetostratigraphy and geomagnetic field morphology. Phys. Earth Planet. Inter. 237, 18–24.

Faller, A.M., Soper, N.J., 1979. Palaeomagnetic evidence for the origin of the coastal flexure and dyke swarm in central E Greenland. J. Geol. Soc. 136 (6), 737–744.

Fetisova, A.M., Veselovskiy, R.V., Balabanov, Y.P., Sal'naya, N.V., 2017. Inclination shallowing in the Permian/Triassic boundary sedimentary sections of the Middle Volga region in light of the new paleomagnetic data. Izvestiya. Phys. Solid Earth 53, 635–644.

Fetisova, A.M., Veselovskiy, R.V., Scholze, F., Balabanov, Y.P., 2018. The new Permian-Triassic paleomagnetic pole for the east European Platform corrected for inclination shallowingIzvestiya. Phy. Solid Earth 54, 150–162.

Fisher, R.A., 1953. Dispersion on a sphere. Proc. Roy. Soc. Lond. Ser. A. Math. Phys. Sci. 217 (1130), 295–305.

Font, E., Youbi, N., Fernandes, S., El Hachimi, H., Kratinova, Z., Hamim, Y., 2011. Revisiting the magnetostratigraphy of the Central Atlantic Magmatic Province (CAMP) in Morocco. Earth Planet. Sci. Lett. 309 (3–4), 302–317.

Fournier, M., Chamot-Rooke, N., Petit, C., Huchon, P., Al-Kathiri, A., Audin, L., Merkouriev, S., 2010. Arabia-Somalia plate kinematics, evolution of the Aden-Owen-Carlsberg triple junction, and opening of the Gulf of Aden. Journal of Geophysical Research: SolidEarth 115 (B4).

Franco, D.R., Ernesto, M., Ponte-Neto, C.F., Hinnov, L.A., Berquó, T.S., Fabris, J.D., Rosière, C.A., 2012. Magnetostratigraphy and mid-palaeolatitude VGP dispersion during the Permo-Carboniferous Superchron: results from Paraná Basin (Southern Brazil) rhythmites. Geophys. J. Int., no-no. https://doi.org/10.1111/j.1365-246X.2012.05670.x.

Fu, R.R., Kent, D.V., Hemming, S.R., Gutiérrez, P., Creveling, J.R., 2020. Testing the occurrence of late Jurassic true polar wander using the La Negra volcanics of northern Chile. Earth Planet. Sci. Lett. 529.

Gaina, C., Jakob, J., 2019. Global eocene tectonic unrest: possible causes and effects around the North American plate. Tectonophysics 760, 136–151.

Gaina, C., Torsvik, T.H., van Hinsbergen, D.J., Medvedev, S., Werner, S.C., Labails, C., 2013. The African Plate: a history of oceanic crust accretion and subduction since the Jurassic. Tectonophysics 604, 4–25.

Gallo, L.C., Farjat, A.D., Tomezzoli, R.N., Calvagno, J.M., Hernández, R.M., 2021. Sedimentary evolution of a Permo-Carboniferous succession in southern Bolivia: responses to icehouse-greenhouse transition from a probabilistic assessment of paleolatitudes. J. S. Am. Earth Sci. 106, 102923.

Gallo, L.C., Tomezzoli, R.N., Cristallini, E.O., 2017. A pure dipole analysis of the G ondwana apparent polar wander path: Paleogeographic implications in the evolution of P angea. Geochem. Geophys. Geosyst. 18 (4), 1499–1519.

Gallo, L.C., Domeier, M., Sapienza, F., Swanson-Hysell, N.L., Vaes, B., Zhang, Y., van der Boon, A., 2023. Embracing uncertainty to Resolve Polar Wander: a Case Study of Cenozoic North America. Geophys. Res. Lett. 50 (11).

Ganerød, M., Smethurst, M.A., Rousse, S., Torsvik, T.H., Prestvik, T., 2008. Reassembling the Paleogene-Eocene North Atlantic igneous province: New paleomagnetic constraints from the Isle of Mull,Scotland. Earth Planet. Sci. Lett. 272 (1–2), 464–475. https://doi.org/10.1016/j.epsl.2008.05.016.

Ganerød, M., Smethurst, M.A., Torsvik, T.H., Prestvik, T., Rousse, S., McKenna, C., Hendriks, B.W.H., 2010. The North Atlantic Igneous Province reconstructed and its relation to the Plume Generation Zone: the Antrim Lava Group revisited. Geophys. J. Int., no-no. https://doi.org/10.1111/j.1365-246X.2010.04620.x.

Gao, L., Zhao, Y., Yang, Z., Liu, J., Liu, X., Zhang, S.H., Pei, J., 2018. New paleomagnetic and 40Ar/39Ar geochronological results for the South Shetland Islands, West Antarctica, and their tectonic implications. J. Geophys. Res. Solid Earth 123 (1), 4–30.

Gao, Y., Zhang, S., Zhao, H., Ren, Q., Yang, T., Wu, H., Li, H., 2021. North China block underwent simultaneous true polar wander and tectonic convergence in late Jurassic: New paleomagnetic constraints. Earth Planet. Sci. Lett. 567, 117012.

Garza, R.S.M., Acton, G.D., Geissman, J.W., 1998. Carboniferous through Jurassic paleomagnetic data and their bearing on rotation of the Colorado Plateau. J. Geophys. Res. Solid Earth 103 (B10), 24179–24188.

Gerritsen, D., Vaes, B., van Hinsbergen, D.J., 2022. Influence of data filters on the position and precision of paleomagnetic poles: what is the optimal sampling strategy? Geochem. Geophys. Geosyst. e2021GC010269.

Gibbons, A.D., Whittaker, J.M., Müller, R.D., 2013. The breakup of East Gondwana: Assimilating constraints from Cretaceous ocean basins around India into a best-fit tectonic model. J. Geophys. Research Solid Earth 118 (3), 808–822.

Gidskehaug, A., Creer, K.M., Mitchell, J.G., 1975. Palaeomagnetism and K-Ar ages of the South-West african basalts and their bearing on the time of initial rifting of the South Atlantic Ocean. Geophys. J. Int. 42 (1), 1–20.

Globerman, B.R., Irving, E., 1988. Mid-cretaceous paleomagnetic reference field for North America: Restudy of 100 Ma intrusive rocks from Arkansas. J. Geophys. Res. Solid Earth 93 (B10), 11721–11733.

Goguitchaichvili, A., Cervantes Solano, M., Camps, P., Sanchez Bettucci, L., Mena, M., Trindade, R., Lopez Loera, H., 2013. The Earth's magnetic field prior to the cretaceous Normal Superchron: new palaeomagnetic results from the Alto Paraguay Formation. Int. Geol. Rev. 55 (6), 692–704.

Goguitchaichvili, A., González, J.A., Pluhar, C.J., Alva-Valdivia, L., Rosas Elguera, J., Ruiz-Martínez, V.C., Caballero, C., 2011. A comprehensive rock-magnetic, paleomagnetic, paleointensity and geochronologic study along the western Trans-Mexican Volcanic Belt: geodynamic and geomagnetic implications. Geofísica internacional 50 (2), 227–254.

Goldreich, P., Toomre, A., 1969. Some remarks on polar wandering. J. Geophys. Res. 74 (10), 2555–2567.

González-Naranjo, G.A., Molina-Garza, R.S., Aranda-Gómez, J.J., Tristán-González, M., Aguillón-Róbles, A., Iriondo, A., Bellón, H., 2012. Paleomagnetismo y edad de la Ignimbrita Panalillo Superior, Campo Volcánico de San Luis Potosí, México. Bol. Soc. Geol. Mex. 64 (3), 387–409.

González, V.R., Renda, E., Vizán, H., Ganerød, M., Puigdomenech, C., Zaffarana, C., 2022. Deformation along the Deseado Massif (Patagonia, Argentina) during the Jurassic Period and its relationship with the Gondwana breakup: paleomagnetic and geochronological constraints. Tectonophysics 834, 229389.

Gordon, R.G., Livermore, R.A., 1987. Apparent polar wander of the mean-lithosphere reference frame. Geophys. J. Int. 91 (3), 1049–1057.

Gradstein, F.M., Ogg, J.G., Schmitz, M.D., Ogg, G.M., 2020. Geologic Time Scale 2020. Elsevier.

Granot, R., Dyment, J., 2015. The cretaceous opening of the South Atlantic Ocean. Earth Planet. Sci. Lett. 414, 156–163.

Granot, R., Dyment, J., 2018. Late Cenozoic unification of East and West Antarctica. Nat. Commun. 9 (1), 1–10.

Granot, R., Cande, S., Stock, J., Damaske, D., 2013. Revised Eocene-Oligocene kinematics for the West Antarctic rift system. Geophys. Res. Lett. 40 (2), 279–284.

Gunderson, J.A., Sheriff, S.D., 1991. A new late cretaceous paleomagnetic pole from the Adel Mountains, west Central Montana. J. Geophys. Res. Solid Earth 96 (B1), 317–326.

Gürer, D., Granot, R., van Hinsbergen, D.J., 2022. Plate tectonic chain reaction revealed by noise in the Cretaceous quiet zone. Nat. Geosci. 15 (3), 233–239.

Hagstrum, J.T., Johnson, C.M., 1986. A paleomagnetic and stable isotope study of the pluton at Rio Hondo near Questa, New Mexico: implications for CRM related to hydrothermal alteration. Earth Planet. Sci. Lett. 78 (2–3), 296–314.

Hagstrum, J.T., Lipman, P.W., 1986. Paleomagnetism of the structurally deformed Latir volcanic field, northern New Mexico: Relations to formation of the Questa caldera and development of the Rio Grande rift. J. Geophys. Res. Solid Earth 91 (B7), 7383–7402. https://doi.org/10.1029/JB091iB07p07383.

Haldan, M.M., Langereis, C.G., Biggin, A.J., Dekkers, M.J., Evans, M.E., 2009. A comparison of detailed equatorial red bed records of secular variation during the Permo-Carboniferous Reversed Superchron. Geophys. J. Int. 177 (3), 834–848.

Haldan, M.M., Meijers, M.J.M., Langereis, C.G., Larsen, B.T., Heyer, H., 2014. New palaeomagnetic results from the Oslo Graben, a Permian Superchron lava province. Geophys. J. Int. 199 (3), 1554–1571.

Handford, B., Biggin, A., Haldan, M., Langereis, C., 2021. Analyzing Triassic and Permian Geomagnetic Paleosecular Variation and the Implications for Ancient Field Morphology. Geochem. Geophys. Geosyst. 22 (11) e2021GC009930.

Hankard, F., Cogné, J.P., Kravchinsky, V.A., Carporzen, L., Bayasgalan, A., Lkhagvadorj, P., 2007a. New Tertiary paleomagnetic poles from Mongolia and Siberia at 40, 30, 20, and 13 Ma: Clues on the inclination shallowing problem in Central Asia. J. Geophys. Res. Solid Earth 112 (B2).

Hankard, F., Cogné, J.P., Lagroix, F., Quidelleur, X., Kravchinsky, V.A., Bayasgalan, A., Lkhagvadorj, P., 2008. Palaeomagnetic results from Palaeocene basalts from Mongolia reveal no inclination shallowing at 60 Ma in Central Asia. Geophys. J. Int. 172 (1), 87–102.

Hankard, F., Cogné, J.P., Quidelleur, X., Bayasgalan, A., Lkhagvadorj, P., 2007b. Palaeomagnetism and K—Ar dating of cretaceous basalts from Mongolia. Geophys. J. Int. 169 (3), 898–908.

Hansma, J., Tohver, E., 2018. Palaeomagnetism of mid-Miocene leucitite volcanics in eastern Australia. Geophys. J. Int. 215 (1), 303–313.

Hansma, J., Tohver, E., 2019. Paleomagnetism of Oligocene hot spot volcanics in Central Queensland, Australia. J. Geophys. Res. Solid Earth 124 (7), 6280–6296.

Hansma, J., Tohver, E., 2020. Southward drift of eastern Australian hotspots in the paleomagnetic reference frame is consistent with global true polar wander estimates. Front.Earth Sci. 489.

Harcombe-Smee, B.J., Piper, J.D.A., Rolph, T.C., Thomas, D.N., 1996. A palaeomagnetic and palaeointensity study of the Mauchline lavas, south-West Scotland. Phys. Earth Planet. Inter. 94 (1–2), 63–73.

Hargraves, R.B., Briden, J.C., Daniels, B.A., 1999. Palaeomagnetism and magnetic fabric in the Freetown complex.Sierra Leone. Geophys. J. Int. 136 (3), 705–713.

Harlan, S.S., Morgan, L.A., 2010. Paleomagnetic results from Tertiary volcanic strata and intrusions, Absaroka Volcanic Supergroup, Yellowstone National Park and vicinity: Contributions to the north american apparent polar wander path. Tectonophysics 485 (1–4), 245–259. https://doi.org/10.1016/j.tecto.2009.12.025.

Harlan, S.S., Geissman, J.W., Henry, C.D., Onstott, T.C., 1995. Paleomagnetism and 40Ar/39Ar geochronology of gabbro sills at Mariscal Mountain anticline, southern big Bend National Park, Texas: Implications for the timing of Laramide tectonism and vertical axis rotations in the southern Cordilleran orogenic belt. Tectonics 14 (2), 307–321.

Harlan, S.S., Geissman, J.W., Lageson, D.R., Snee, L.W., 1988. Paleomagnetic and isotopic dating of thrust-belt deformation along the eastern edge of the Helena salient, northern Crazy Mountains Basin,Montana. Geol. Soc. Am. Bull. 100 (4), 492–499.

Harlan, S.S., Geissman, J.W., Whisner, S.C., Schmidt, C.J., 2008. Paleomagnetism and geochronology of sills of the Doherty Mountain area, southwestern Montana: Implications for the timing of fold-and-thrust belt deformation and vertical-axis rotations along the southern margin of the Helena salient. Geol. Soc. Am. Bull. 120 (9–10), 1091–1104. https://doi.org/10.1130/b26313.1.

Harrison, C.G.A., Lindh, T., 1982. A polar wandering curve for North America during the Mesozoic and Cenozoic. J. Geophys. Res. Solid Earth 87 (B3), 1903–1920.

Heslop, D., Roberts, A.P., 2016. Estimation and propagation of uncertainties associated with paleomagnetic directions. J. Geophys. Res. Solid Earth 121 (4), 2274–2289.

Heslop, D., Roberts, A.P., 2020. Uncertainty propagation in hierarchical paleomagnetic reconstructions. Journal of Geophysical Research: SolidEarth 125 (6) e2020JB019488.

Hodgson, B.D., Dagley, P., Mussett, A.E., 1990. Magnetostratigraphy of the Tertiary igneous rocks of Arran. Scott. J. Geol. 26 (2), 99–118.

Hodych, J.P., Hayatsu, A., 1988. Paleomagnetism and K-Ar isochron dates of early Jurassic basaltic flows and dikes of Atlantic Canada. Can. J. Earth Sci. 25 (12), 1972–1989.

Hospers, J., 1954. Rock magnetism and polar wandering. Nature 173 (4416), 1183–1184.

Hounslow, M.W., McIntosh, G., Edwards, R.A., Laming, D.J., Karloukovski, V., 2017. End of the Kiaman Superchron in the Permian of SW England: magnetostratigraphy of the Aylesbeare Mudstone and Exeter groups. J. Geol. Soc. 174 (1), 56–74.

Huang, S., Pan, Y., Zhu, R., 2013. Paleomagnetism of the late Cretaceous volcanic rocks of the Shimaoshan Group in Yongtai County, Fujian Province. Sci. China Earth Sci. 56, 22–30.

Iglesia Llanos, M.P., Lanza, R., Riccardi, A.C., Geuna, S., Laurenzi, M.A., Ruffini, R., 2003. Palaeomagnetic study of the El Quemado complex and Marifil formation, Patagonian Jurassic igneous province,Argentina. Geophys. J. Int. 154 (3), 599–617.

Irving, E., 1964. Paleomagnetism and Its Application to Geological and Geophysical Problems. Wiley, New York.

Irving, E., 1977. Drift of the major continental blocks since the Devonian. Nature 270 (5635), 304–309.

Irving, E., 1979. Paleopoles and paleolatitudes of North America and speculations about displaced terrains. Can. J. Earth Sci. 16 (3), 669–694.

Irving, E., Irving, G., 1982. Apparent polar wander paths Carboniferous through Cenozoic and the assembly of Gondwana. Geophys. Surv. 5 (2), 141–188.

Irving, E., Baker, J., Wynne, P.J., Hamilton, T.S., Wingate, M.T.D., 2000. Evolution of the Queen Charlotte Basin; further paleomagnetic evidence of Tertiary extension and tilting. Tectonophysics 326 (1–2), 1–22.

Jarboe, N.A., Koppers, A.A., Tauxe, L., Minnett, R., Constable, C., 2012. The online MagIC Database: data archiving, compilation, and visualization for the geomagnetic, paleomagnetic and rock magnetic communities. In: AGU Fall Meeting Abstracts, Vol. 2012. GP31A-1063.

Jay, A.E., Niocaill, C.M., Widdowson, M., Self, S., Turner, W., 2009. New palaeomagnetic data from the Mahabaleshwar Plateau, Deccan Flood Basalt Province, India: implications for the volcanostratigraphic architecture of continental flood basalt provinces. J. Geol. Soc. 166 (1), 13–24.

Johnson, C.L., McFadden, P., 2007. Time-averaged field and paleosecular variation. Geomagnetism 5, 417–453.

Jones, D.L., Duncan, R.A., Briden, J.C., Randall, D.E., MacNiocaill, C., 2001. Age of the Batoka basalts, northern Zimbabwe, and the duration of Karoo large Igneous Province magmatism. Geochem. Geophys. Geosyst. 2 (2).

Kent, D.V., Olsen, P.E., 2008. Early Jurassic magnetostratigraphy and paleolatitudes from the Hartford continental rift basin (eastern North America): Testing for polarity bias and abrupt polar wander in association with the Central Atlantic magmatic province. J. Geophys. Res. Solid Earth 113 (B6).

Kent, D.V., Tauxe, L., 2005. Corrected late Triassic latitudes for continents adjacent to the North Atlantic. Science 307 (5707), 240–244.

Kent, D.V., Witte, W.K., 1993. Slow apparent polar wander for North America in the late Triassic and large Colorado Plateau rotation. Tectonics 12 (1), 291–300.

Kent, D.V., Irving, E., 2010. Influence of inclination error in sedimentary rocks on the Triassic and Jurassic apparent pole wander path for North America and implications for Cordilleran tectonics. J. Geophys. Res. Solid Earth 115 (B10).

Kent, D.V., Muttoni, G., 2020. Pangea B and the late paleozoic ice age. Palaeogeogr. Palaeoclimatol. Palaeoecol. 553, 109753.

Kent, D.V., Kjarsgaard, B.A., Gee, J.S., Muttoni, G., Heaman, L.M., 2015. Tracking the late Jurassic apparent (or true) polar shift in U-Pb-dated kimberlites from cratonic North America (Superior Province of Canada). Geochem. Geophys. Geosyst. 16 (4), 983–994.

Kent, D.V., Olsen, P.E., Muttoni, G., Et-Touhami, M., 2021. A late Permian paleopole from the Ikakern Formation (Argana basin, Morocco) and the configuration of Pangea. Gondwana Res. 92, 266–278.

Kidane, T., Abebe, B., Courtillot, V., Herrero, E., 2002. New paleomagnetic result from the ethiopian flood basalts in the Abbay (Blue Nile) and Kessem gorges. Earth Planet. Sci. Lett. 203 (1), 353–367.

Klootwijk, C.T., 1971. Palaeomagnetism of the-Upper Gondwana-Rajmahal traps, Northeast India. Tectonophysics 12 (6), 449–467.

Klootwijk, C.T., 2003. Carboniferous palaeomagnetism of the Werrie Block, northwestern Tamworth Belt, and the New England pole path. Aust. J. Earth Sci. 50 (6), 865–902.

Knight, K.B., Nomade, S., Renne, P.R., Marzoli, A., Bertrand, H., Youbi, N., 2004. The Central Atlantic Magmatic Province at the Triassic-Jurassic boundary: paleomagnetic and 40Ar/39Ar evidence from Morocco for brief, episodic volcanism. Earth Planet. Sci. Lett. 228 (1–2), 143–160.

Kodama, K.P., 2009. Simplification of the anisotropy-based inclination correction technique for magnetite-and haematite-bearing rocks: a case study for the Carboniferous Glenshaw and Mauch Chunk Formations, North America. J. Geophys. Res. 176 (2), 467–477.

Kodama, K.P., 2012. Paleomagnetism of Sedimentary Rocks: Process and Interpretation. John Wiley and Sons.

Kono, M., Kinoshita, H., Aoki, Y., 1972. Paleomagnetism of the Deccan Trap basalts in India. J. Geomagn. Geoelectr. 24 (1), 49–67.

Konrad, H.J., Nairn, A.E.M., 1972. The palaeomagnetism of the Permian rocks of the Black Forest,Germany. Geophys. J. Int. 27 (4), 369–382.

Konstantinov, K.M., Bazhenov, M.L., Fetisova, A.M., Khutorskoy, M.D., 2014. Paleomagnetism of trap intrusions, East Siberia: Implications to flood basalt emplacement and the Permo-Triassic crisis of biosphere. Earth Planet. Sci. Lett. 394, 242–253.

Kosterov, A.A., Perrin, M., 1996. Paleomagnetism of the Lesotho basalt, southern Africa. Earth Planet. Sci. Lett. 139 (1–2), 63–78.

Koymans, M.R., van Hinsbergen, D.J.J., Pastor-Galán, D., Vaes, B., Langereis, C.G., 2020. Towards FAIR paleomagnetic data management through Paleomagnetism. Org 2.0. Geochem. Geophys. Geosyst. 21 (2) e2019GC008838.

Kravchinsky, V.A., Cogné, J.P., Harbert, W.P., Kuzmin, M.I., 2002. Evolution of the Mongol-Okhotsk Ocean as constrained by new palaeomagnetic data from the Mongol-Okhotsk suture zone,Siberia. Geophys. J. Int. 148 (1), 34–57.

Kulakov, E.V., Torsvik, T.H., Doubrovine, P.V., Slagstad, T., Ganerød, M., Silkoset, P., Werner, S.C., 2021. Jurassic fast polar shift rejected by a new high-quality paleomagnetic pole from southwest Greenland. Gondwana Res. 97, 240–262.

Labails, C., Olivet, J.L., Aslanian, D., Roest, W.R., 2010. An alternative early opening scenario for the Central Atlantic Ocean. Earth Planet. Sci. Lett. 297 (3–4), 355–368.

Lanza, R., Zanella, E., 1993. Paleomagnetism of the Ferrar dolerite in the northern Prince Albert Mountains (Victoria Land, Antarctica). Geophys. J. Int. 114 (3), 501–511.

Lapointe, P.L., 1979. Paleomagnetism of the Notre Dame Bay lamprophyre dikes, Newfoundland, and the opening of the North Atlantic Ocean. Can. J. Earth Sci. 16 (9), 1823–1831.

Latyshev, A.V., Lapkovskii, A.A., Veselovskiy, R.V., Fetisova, A.M., Krivolutskaya, N.A., 2021b. Paleomagnetism of the Permian-Triassic Siberian Traps Intrusions from the Kulumbe River Valley, Northwestern Siberian Platform,Izvestiya. Phys. Solid Earth 57 (3), 375–394.

Latyshev, A.V., Veselovskiy, R.V., Ivanov, A.V., 2018. Paleomagnetism of the Permian-Triassic intrusions from the Tunguska syncline and the Angara-Taseeva depression, Siberian Traps large Igneous Province: evidence of contrasting styles of magmatism. Tectonophysics 723, 41–55.

Latyshev, A., Krivolutskaya, N., Ulyakhina, P., Fetisova, A., Veselovskiy, R., Pasenko, A., et al., 2021a. Paleomagnetism of the Permian-Triassic intrusions from the Norilsk region (the Siberian platform, Russia): Implications for the timing and correlation of magmatic events, and magmatic evolution. J. Asian Earth Sci. 217.

Lemna, O.S., Bachtadse, V., Kirscher, U., Rolf, C., Petersen, N., 2016. Paleomagnetism of the Jurassic Transantarctic Mountains revisited—Evidence for large dispersion of apparent polar wander within less than 3 Myr. Gondwana Res. 31, 124–134.

Leroy, S., Mauffret, A., Patriat, P., Mercier de Lépinay, B., 2000. An alternative interpretation of the Cayman trough evolution from a reidentification of magnetic anomalies. Geophys. J. Int. 141 (3), 539–557.

Lhuillier, F., Gilder, S.A., 2019. Palaeomagnetism and geochronology of Oligocene and Miocene volcanic sections from Ethiopia: geomagnetic variability in the Afro-Arabian region over the past 30 Ma. Geophys. J. Int. 216 (2), 1466–1481.

Liss, D., Owens, W.H., Hutton, D.H.W., 2004. New palaeomagnetic results from the Whin Sill complex: evidence for a multiple intrusion event and revised virtual geomagnetic poles for the late Carboniferous for the British Isles. J. Geol. Soc. 161 (6), 927–938.

Lock, J., McElhinny, M.W., 1991. Database design. In: The Global Paleomagnetic Database. Springer, Dordrecht, pp. 317–327.

Lossada, A.C., Rapalini, A.E., Sánchez Betucci, L., 2014. Enjambre de diques básicos de Nico Pérez-Zapicán, Uruguay: evidencias radimétricas y paleomagnéticas sobre su edad. Rev. Asoc. Geol. Argent. 71 (3), 345–355.

Lotfy, H.I., Odah, H.H., 2015. Paleo-tectonic positions of Northeast Africa during Cretaceous–Paleocene: Paleomagnetic study on East Gilf Kebir Plateau basalts [59 Ma], Southwestern Desert,Egypt. NRIAG J. Astron. Geophys. 4 (1), 32–43.

Lotfy, H., Elaal, E.aA., 2018. Equatorial paleolatitude for Northeast Africa in the late Triassic: paleomagnetic study on the Gezira and Bir-Umhebal [229–223 Ma] ring complexes, Southeastern Desert,Egypt. Arab. J. Geosci. 11, 1–16.

Marton, E., Marton, P., 1976. A palaeomagnetic study of the Nigerian volcanic provinces. Pure Appl. Geophys. 114, 61–69.

McDougall, I., McElhinny, M.W., 1970. The Rajmahal traps of India—KAr ages and palaeomagnetism. Earth Planet. Sci. Lett. 9 (4), 371–378.

McElhinny, M.W., Jones, D.L., 1965. Palaeomagnetic measurements on some Karroo dolerites from Rhodesia. Nature 206 (4987), 921–922.

McElhinny, M.W., McFadden, P.L., 2000. Paleomagnetism: Continents and Oceans. Elsevier.

McElhinny, M.W., Briden, J.C., Jones, D.L., Brock, A., 1968. Geological and geophysical implications of paleomagnetic results from Africa. Rev. Geophys. 6 (2), 201–238.

McElhinny, M.W., Embleton, B.J.J., Wellman, P., 1974. A synthesis of Australian Cenozoic palaeomagnetic results. Geophys. J. Int. 36 (1), 141–151.

McEnroe, S.A., 1996a. North America during the lower cretaceous: New palaeomagnetic constraints from intrusions in New England. Geophys. J. Int. 126 (2), 477–494.

McEnroe, S.A., 1996b. A Barremian-Aptian (Early Cretaceous) north american paleomagnetic reference pole. J. Geophys. Res. Solid Earth 101 (B7), 15819–15835.

McFadden, P.L., McElhinny, M.W., 1995. Combining groups of paleomagnetic directions or poles. Geophys. Res. Lett. 22 (16), 2191–2194.

McIntosh, W.C., Chapin, C.E., Ratté, J.C., Sutter, J.F., 1992. Time-stratigraphic framework for the Eocene-Oligocene Mogollon-Datil volcanic field, Southwest New Mexico. Geol. Soc. Am. Bull. 104 (7), 851–871.

McQuarrie, N., Wernicke, B.P., 2005. An animated tectonic reconstruction of southwestern North America since 36 Ma. Geosphere 1 (3), 147–172.

Meert, J.G., Tamrat, E., 2006. Paleomagnetic evidence for a stationary Marion hotspot: additional paleomagnetic data from Madagascar. Gondwana Res. 10 (3–4), 340–348. https://doi.org/10.1016/j.gr.2006.04.008.

Meert, J.G., Pivarunas, A.F., Evans, D.A., Pisarevsky, S.A., Pesonen, L.J., Li, Z.X., Salminen, J.M., 2020. The magnificent seven: a proposal for modest revision of the quality index. Tectonophysics 790, 228549.

Meijers, M.J., Hamers, M.F., van Hinsbergen, D.J., van der Meer, D.G., Kitchka, A., Langereis, C.G., Stephenson, R.A., 2010. New late Paleozoic paleopoles from the Donbas Foldbelt (Ukraine): Implications for the Pangea a vs. B controversy. Earth Planet. Sci. Lett. 297 (1–2), 18–33.

Mena, M., Goguitchaichvili, A., Solano, M.C., Vilas, J.F., 2011. Paleosecular variation and absolute geomagnetic paleointensity records retrieved from the early cretaceous Posadas Formation (Misiones, Argentina). Stud. Geophys. Geod. 55, 279–309.

Mendía, J.E., 1978. Palaeomagnetism of alkaline lava flows from El Salto-Almafuerte, Cordoba Province,Argentina. Geophys. J. Int. 54 (3), 539–546.

Metelkin, D.V., Kazansky, A.Y., Bragin, V.Y., Tsel'movich, V.A., Lavrenchuk, A.V., Kungurtsev, L.V., 2007. Paleomagnetism of the late cretaceous intrusions from the Minusa trough (southern Siberia). Russ. Geol. Geophys. 48 (2), 185–198.

Molina-Garza, R.S., van Hinsbergen, D.J.J., Rogers, R.D., Ganerød, M., Dekkers, M.J., 2012. The Padre Miguel Ignimbrite Suite, Central Honduras: Paleomagnetism, geochronology, and tectonic implications. Tectonophysics 574–575, 144–157.

Montes-Lauar, C.R., Pacca, I.G., Melfi, A.J., Kawashita, K., 1995. Late cretaceous alkaline complexes, southeastern Brazil: paleomagnetism and geochronology. Earth Planet. Sci. Lett. 134 (3–4), 425–440.

Moulin, M., Fluteau, F., Courtillot, V., Marsh, J., Delpech, G., Quidelleur, X., et al., 2011. An attempt to constrain the age, duration, and eruptive history of the Karoo flood basalt: Naude's Nek section (South Africa). J. Geophys. Res. 116 (B7).

Moulin, M., Fluteau, F., Courtillot, V., Marsh, J., Delpech, G., Quidelleur, X., Gérard, M., 2017. Eruptive history of the Karoo lava flows and their impact on early Jurassic environmental change. J. Geophys. Res. Solid Earth 122 (2), 738–772.

Mueller, C.O., Jokat, W., 2019. The initial Gondwana break-up: a synthesis based on new potential field data of the Africa-Antarctica Corridor. Tectonophysics 750, 301–328.

Mulder, F.G., 1971. Paleomagnetic research in some parts of central and southern Sweden. Sver. Geol. Unders. Ser. C 653, 1–56.

Müller, R.D., Royer, J.Y., Cande, S.C., Roest, W.R., Maschenkov, S., 1999. New constraints on the late Cretaceous/Tertiary plate tectonic evolution of the Caribbean. Sedimentary Basins of the World 4, 33–59.

Müller, R.D., Sdrolias, M., Gaina, C., Roest, W.R., 2008. Age, spreading rates, and spreading asymmetry of the world's ocean crust. Geochem. Geophys. Geosyst. 9 (4).

Müller, R.D., Seton, M., Zahirovic, S., Williams, S.E., Matthews, K.J., Wright, N.M., Cannon, J., 2016. Ocean basin evolution and global-scale plate reorganization events since Pangea breakup. Annu. Rev. Earth Planet. Sci. 44 (1), 107–138.

Müller, R.D., Zahirovic, S., Williams, S.E., Cannon, J., Seton, M., Bower, D.J., Liu, S., 2019. A global plate model including lithospheric deformation along major rifts and orogens since the Triassic. Tectonics 38 (6), 1884–1907.

Muttoni, G., Kent, D.V., 2019. Jurassic monster polar shift confirmed by sequential paleopoles from Adria, promontory of Africa. J. Geophys. Res. Solid Earth 124 (4), 3288–3306.

Muttoni, G., Dallanave, E., Channell, J.E.T., 2013. The drift history of Adria and Africa from 280 Ma to present, Jurassic true polar wander, and zonal climate control on Tethyan sedimentary facies. Palaeogeogr. Palaeoclimatol. Palaeoecol. 386, 415–435.

Muttoni, G., Erba, E., Kent, D.V., Bachtadse, V., 2005. Mesozoic Alpine facies deposition as a result of past latitudinal plate motion. Nature 434 (7029), 59–63.

Muttoni, G., Kent, D.V., Garzanti, E., Brack, P., Abrahamsen, N., Gaetani, M., 2003. Early permian pangea 'B'to late permian pangea 'A'. Earth Planet. Sci. Lett. 215 (3–4), 379–394.

Nijenhuis, G.H.W., 1961. A palaeomagnetic study of the Permian volcanics in the Nahe region (SW,Germany). Geol. Mijnbouw 40 (1), 26–38.

Nomade, S., Théveniaut, H., Chen, Y., Pouclet, A., Rigollet, C., 2000. Paleomagnetic study of French Guyana early Jurassic dolerites: hypothesis of a multistage magmatic event. Earth Planet. Sci. Lett. 184 (1), 155–168.

Opdyke, N.D., Giles, P.S., Utting, J., 2014. Magnetic polarity stratigraphy and palynostratigraphy of the Mississippian-Pennsylvanian boundary interval in eastern North America and the age of the beginning of the Kiaman. Bulletin 126 (7–8), 1068–1083.

Owen-Smith, T.M., Ganerød, M., van Hinsbergen, D.J., Gaina, C., Ashwal, L.D., Torsvik, T.H., 2019. Testing early cretaceous Africa-South America fits with new palaeomagnetic data from the Etendeka Magmatic Province (Namibia). Tectonophysics 760, 23–35.

Pacca, I.G., Hiodo, F.Y., 1976. Paleomagnetic analysis of Mesozoic Serra Geral basaltic lava flows in the Southern Brazil. Ann. Acad. Br asil Cienc. 48, 207–214.

Palencia-Ortas, A., Ruiz-Martínez, V.C., Villalaín, J.J., Osete, M.L., Vegas, R., Touil, A., Torsvik, T.H., 2011. A new 200 Ma paleomagnetic pole for Africa, and paleo-secular variation scatter from Central Atlantic Magmatic Province (CAMP) intrusives in Morocco (Ighrem and Foum Zguid dykes). Geophys. J. Int. 185 (3), 1220–1234.

Pan, Y., Hill, M.J., Zhu, R., 2005. Paleomagnetic and paleointensity study of an Oligocene-Miocene lava sequence from the Hannuoba Basalts in northern China. Phys. Earth Planet. Inter. 151 (1–2), 21–35.

Pastor-Galán, D., 2022. From supercontinent to superplate: late Paleozoic Pangea's inner deformation suggests it was a short-lived superplate. Earth Sci. Rev. 226, 103918.

Patel, J.P., Raja, P.K.S., 1979. Paleomagnetic results from the Narosura and Magadi Volcanics of Kenya. Phys. Earth Planet. Inter. 19 (3), 7–14.

Pavlov, V.E., Fluteau, F., Latyshev, A.V., Fetisova, A.M., Elkins-Tanton, L.T., Black, B.A., Veselovskiy, R.V., 2019. Geomagnetic secular variations at the Permian-Triassic boundary and pulsed magmatism during eruption of the Siberian Traps. Geochem. Geophys. Geosyst. 20 (2), 773–791.

Petronis, M.S., Brister, A.R., Rapprich, V., de Vries, B.V.W., Lindline, J., Misurec, J., 2015. Emplacement history of the Trosky basanitic volcano (Czech Republic):

paleomagnetic, rock magnetic, petrologic, and anisotropy of magnetic susceptibility evidence for lingering growth of a monogenetic volcano. J. Geosci. 60 (3), 129–147.

Petronis, M.S., Hacker, D.B., Holm, D.K., Geissman, J.W., Harlan, S.S., 2004. Magmatic flow paths and palaeomagnetism of the Miocene Stoddard Mountain laccolith, Iron Axis region, Southwestern Utah, USA. Geol. Soc. Lond., Spec. Publ. 238 (1), 251–283.

Phillips, J.D., Forsyth, D., 1972. Plate tectonics, paleomagnetism, and the opening of the Atlantic. Geol. Soc. Am. Bull. 83 (6), 1579–1600.

Pierce, J., Zhang, Y., Hodgin, E.B., Swanson-Hysell, N.L., 2022. Quantifying inclination shallowing and representing flattening uncertainty in sedimentary paleomagnetic poles.

Poblete, F., Arriagada, C., Roperch, P., Astudillo, N., Hervé, F., Kraus, S., Le Roux, J.P., 2011. Paleomagnetism and tectonics of the South Shetland Islands and the northern Antarctic Peninsula. Earth Planet. Sci. Lett. 302 (3–4), 299–313.

Prasad, J.N., Patil, S.K., Venkateshwarlu, M., Saraf, P.D., Tripathi, S.C., Rao, D.R.K., 1998. Palaeomagnetic results from the cretaceous Bagh Group in the Narmada Basin, Central India: evidence of pervasive Deccan remagnetization and its implications for Deccan volcanism. Geophys. J. Int. 133 (3), 519–528.

Prévot, M., Roberts, N., Thompson, J., Faynot, L., Perrin, M., Camps, P., 2003. Revisiting the Jurassic geomagnetic reversal recorded in the Lesotho Basalt (Southern Africa). Geophys. J. Int. 155 (2), 367–378.

Qin, H., He, H., Liu, Q., Cai, S., 2011. Palaeointensity just at the onset of the Cretaceous normal superchron. Phys. Earth Planet. Inter. 187 (3–4), 199–211.

Radhakrishna, T., Joseph, M., 2012. Geochemistry and paleomagnetism of Late Cretaceous mafic dikes in Kerala, southwest coast of India in relation to large igneous provinces and mantle plumes in the Indian Ocean region. Bulletin 124 (1–2), 240–255.

Radhakrishna, T., Dallmeyer, R.D., Joseph, M., 1994. Palaeomagnetism and 36Ar40Ar vs. 39Ar40Ar isotope correlation ages of dyke swarms in Central Kerala, India: Tectonic implications. Earth Planet. Sci. Lett. 121 (1–2), 213–226.

Radhakrishna, T., Soumya, G.S., Satyanarayana, K.V.V., 2017. Palaeomagnetism of the cretaceous Lamproites from Gondwana basin of the Damodar Valley in India and migration of the Kerguelen plume in the Southeast Indian Ocean. J. Geodyn. 109, 1–9.

Rao, G.P., Rao, J.M., 1996. Palaeomagnetism of the Rajmahal Traps of India: implication to the reversal in the cretaceous Normal Superchron. J. Geomagn. Geoelectr. 48 (7), 993–1000.

Rapalini, A.E., Vilas, J.F., 1991. Tectonic rotations in the late Palaeozoic continental margin of southern South America determined and dated by palaeomagnetism. Geophys. J. Int. 107 (2), 333–351.

Raposo, M.I.B., Ernesto, M., 1995. An early cretaceous paleomagnetic pole from Ponta Grossa dikes (Brazil): Implications for the South American Mesozoic apparent polar wander path. J. Geophys. Res. Solid Earth 100 (B10), 20095–20109.

Raposo, M.I.B., Ernesto, M., Renne, P.R., 1998. Paleomagnetism and 40Ar/39Ar dating of the Early Cretaceous Florianópolis dike swarm (Santa Catarina Island), Southern Brazil. Phys. Earth Planet. Inter. 108 (4), 275–290.

Reilly, T.A., Raja, P.K.S., Mussett, A.E., Brock, A., 1976. The palaeomagnetism of late Cenozoic volcanic rocks from Kenya and Tanzania. Geophys. J. Int. 45 (3), 483–494.

Ren, S., Zhu, R., Huang, B., Zhang, F., Wang, H., 2004. Paleomagnetic study on orogenic belt: an example from early cretaceous volcanic rocks, Inner Mongolia, China. Sci. China Ser. D Earth Sci. 47, 1127–1133.

Replumaz, A., Tapponnier, P., 2003. Reconstruction of the deformed collision zone between India and Asia by backward motion of lithospheric blocks. J. Geophys. Res. Solid Earth 108 (B6).

Ressetar, R., Martin, D.L., 1980. Paleomagnetism of Eocene igneous intrusions in the valley and ridge province, Virginia and West Virginia. Can. J. Earth Sci. 17 (11), 1583–1588.

Reynolds, R.L., Hudson, M.R., Hon, K., 1986. Paleomagnetic evidence for the timing of collapse and resurgence of the Lake City Caldera, San Juan Mountains, Colorado. J. Geophys. Res. Solid Earth 91 (B9), 9599–9613.

Riisager, J., Riisager, P., Pedersen, A.K., 2003a. The C27n–C26r geomagnetic polarity reversal recorded in the West Greenland flood basalt province: how complex is the transitional field? J. Geophys. Res. Solid Earth 108 (B3).

Riisager, J., Riisager, P., Pedersen, A.K., 2003b. Paleomagnetism of large igneous provinces: case-study from West Greenland, North Atlantic igneous province. Earth Planet. Sci. Lett. 214 (3–4), 409–425.

Riisager, P., Knight, K.B., Baker, J.A., Ukstins Peate, I., Al-Kadasi, M., Al-Subbary, A., Renne, P.R., 2005. Paleomagnetism and 40Ar/39Ar Geochronology of Yemeni Oligocene volcanics: Implications for timing and duration of Afro-Arabian traps and geometry of the Oligocene paleomagnetic field. Earth Planet. Sci. Lett. 237 (3–4), 647–672. https://doi.org/10.1016/j.epsl.2005.06.016.

Riisager, P., Riisager, J., Abrahamsen, N., Waagstein, R., 2002. New paleomagnetic pole and magnetostratigraphy of Faroe Islands flood volcanics, North Atlantic igneous province. Earth Planet. Sci. Lett. 201 (2), 261–276.

Robertson, W.A., 1963. Paleomagnetism of some Mesozoic intrusives and tuffs from eastern Australia. J. Geophys. Res. 68 (8), 2299–2312.

Rochette, P., Tamrat, E., Féraud, G., Pik, R., Courtillot, V., Ketefo, E., Yirgu, G., 1998. Magnetostratigraphy and timing of the Oligocene ethiopian traps. Earth Planet. Sci. Lett. 164 (3–4), 497–510.

Roest, W.R., Srivastava, S.P., 1989. Sea-floor spreading in the Labrador Sea: a new reconstruction. Geology 17 (11), 1000–1003.

Rolf, C., Henjes-Kunst, F., 2003. Palaeomagnetic Investigations on Palaeozoic and Mesozoic Igneous and Metasedimentary Rocks from Northern Victoria Land, Antarctica. Terra Antartica 10, 157–170.

Rosas-Elguera, J., Reyes, B.A., Goguitchaichvili, A., Rocha, M., Martínez, M.L., Tostado-Plascencia, M.M., Miranda, C.C., 2011. Paleomagnetic and rock-magnetic survey of

eocene dike swarms from the Tecalitlan area (Western Mexico): Tectonic implications. Stud. Geophys. Geod. 55, 265–278.

Rose, I.R., Zhang, Y., Swanson-Hysell, N.L., 2022. Bayesian paleomagnetic Euler pole inversion for paleogeographic reconstruction and analysis. J. Geophys. Res. SolidEarth 127 (10) e2021JB023890.

Rowley, D.B., 2019. Comparing paleomagnetic pole means with apparent wander paths: a case study and paleomagnetic test of the Greater India versus Greater Indian Basin hypotheses. Tectonics 38 (2), 722–740.

Ruiz González, V., Puigdomenech, C.G., Renda, E.M., Boltshauser, B., Somoza, R., Vizán, H., Fernández, F., 2019. New paleomagnetic pole for the Upper Jurassic Chon Aike Formation of southern Argentina (South America): Testing the tectonic stability of Patagonia with respect to South America, and implications to Middle Jurassic-early cretaceous true polar wander. Tectonophysics 750, 45–55.

Ruiz González, V., Renda, E.M., Vizán, H., Ganerød, M., Puigdomenech, C.G., Zaffarana, C.B., 2022. Deformation along the Deseado Massif (Patagonia, Argentina) during the Jurassic Period and its relationship with the Gondwana breakup: paleomagnetic and geochronological constraints. Tectonophysics 834.

Ruiz-Martínez, V.C., Palencia-Ortas, A., Villalaín, J.J., McIntosh, G., Martín-Hernández, F., 2011. Palaeomagnetic and AMS study of the Tarfaya coastal basin, Morocco: an early Turonian palaeopole for the african plate. Geol. Soc. Lond., Spec. Publ. 357 (1), 211–227.

Ruiz-Martínez, V.C., Torsvik, T.H., van Hinsbergen, D.J., Gaina, C., 2012. Earth at 200 Ma: Global palaeogeography refined from CAMP palaeomagnetic data. Earth Planet. Sci. Lett. 331, 67–79.

Runcorn, S.K., 1959. On the hypothesis that the mean geomagnetic field for parts of geological time has been that of a geocentric axial multipole. J. Atmos. Terrestr. Phys. 14 (1–2), 167–174.

Sahabi, M., Aslanian, D., Olivet, J.L., 2004. A new starting point for the history of the Central Atlantic. Compt. Rendus Geosci. 336 (12), 1041–1052.

Scealy, J.L., Heslop, D., Liu, J., Wood, A.T., 2022. Directions Old and New: Palaeomagnetism and Fisher (1953) Meet Modern Statistics. Int. Stat. Rev. 90 (2), 237–258.

Schettino, A., Scotese, C.R., 2005. Apparent polar wander paths for the major continents (200 Ma to the present day): a palaeomagnetic reference frame for global plate tectonic reconstructions. Geophys. J. Int. 163 (2), 727–759.

Schmidt, A.G., Riisager, P., Abrahamsen, N., Riisager, J., Pedersen, A.K., Van der Voo, R., 2005. Palaeomagnetism of Eocene Talerua Member lavas on Hareøen, West Greenland. Bull. Geol. Soc. Den. 52 (1), 27–37.

Schmidt, P.W., 1976. The non-uniqueness of the Australian Mesozoic palaeomagnetic pole position. Geophys. J. Int. 47 (2), 285–300.

Schmidt, P.W., McDougall, I., 1977. Palaeomagnetic and potassium-argon dating studies of the Tasmanian dolerites. J. Geol. Soc. Aust. 24 (5–6), 321–328.

Schreiber, U., Rotsch, S., 1998. Cenozoic block rotation according to a conjugate shear system in Central Europe—indications from palaeomagnetic measurements. Tectonophysics 299 (1–3), 111–142.

Schult, A., 1974. Palaeomagnetism of Tertiary volcanic rocks from the Ethiopian southern plateau and the Danakil block. J. Geophys. 40 (1), 203–212.

Schult, A., Guerreiro, S.D.C., 1979. Palaeomagnetism of Mesozoic igneous rocks from the Maranhã̄o Basin, Brazil, and the time of opening of the South Atlantic. Earth Planet. Sci. Lett. 42 (3), 427–436.

Schult, A., Soffel, H., 1973. Palaeomagnetism of Tertiary basalts from Libya. Geophys. J. Int. 32 (3), 373–380.

Schult, A., Hussain, A.G., Soffel, H.C., 1982. Palaeomagnetism of Upper cretaceous volcanics and Nubian sandstones of Wadi Natash, SE Egypt and implications for the polar wander path for Africa in the Mesozoic. J. Geophys. 50 (1), 16–22.

Schwarz, E.J., Coleman, L.C., Cattroll, H.M., 1979. Paleomagnetic results from the Skaergaard intrusion, East Greenland. Earth Planet. Sci. Lett. 42 (3), 437–443.

Seton, M., Müller, R.D., Zahirovic, S., Gaina, C., Torsvik, T., Shephard, G., Chandler, M., 2012. Global continental and ocean basin reconstructions since 200 Ma. Earth Sci. Rev. 113 (3–4), 212–270.

Sheriff, S.D., Shive, P.N., 1980. The Rattlesnake Hills of Central Wyoming revisited: further paleomagnetic results. Geophys. Res. Lett. 7 (8), 589–592.

Shi, R., Zhu, R., Pan, Y., Shi, G., Hoffman, K.A., 2002. Paleointensity study of Early Miocene lavas from Pingzhuang, Inner Mongolia, China. Geophys. Res. Letters 29 (21), 22-1.

Sichler, B., Perrin, M., 1993. New early Jurassic paleopole from France and Jurassic apparent polar wander. Earth Planet. Sci. Lett. 115 (1–4), 13–27.

Soffel, H.C., Harzer, F., 1991. An Upper Carboniferous-lower Permian (280 Ma) palaeomagnetic pole from the western margin of the Bohemian Massif. Geophys. J. Int. 105 (2), 547–551.

Somoza, R., 2007. Eocene paleomagnetic pole for South America: Northward continental motion in the Cenozoic, opening of Drake Passage and Caribbean convergence. J. Geophys. Res. 112 (B3) https://doi.org/10.1029/2006jb004610.

Srivastava, S.P., Roest, W.R., 1989. Seafloor spreading history II–IV. *East Coast Basin Atlas Series.* Labrador Sea 100–109.

Srivastava, S.P., Roest, W.R., 1996. Comment on "Porcupine plate hypothesis" by MF Gerstell and JM Stock (Marine Geophysical Researches 16, pp. 315–323, 1994). Marine Geophys. Res. 18 ((5), 589–593.

Steiner, M.B., 2003. A cratonic Middle Jurassic paleopole: Callovian-Oxfordian stillstand (J-2 cusp), rotation of the Colorado Plateau, and Jurassic north american apparent polar wander. Tectonics 22 (3).

Storetvedt, K.M., Mitchell, J.G., Abranches, M.C., Oftedahl, S., 1990. A new kinematic model for Iberia; further palaeomagnetic and isotopic age evidence. Phys. Earth Planet. Inter. 62 (1–2), 109–125.

Storetvedt, K.M., Mitchell, J.G., Abranches, M.C., Maaloe, S., Robin, G., 1992. The coast-parallel dolerite dykes of East Madagascar; age of intrusion, remagnetization and tectonic aspects. J. Afr. Earth Sci. (and the Middle East) 15 (2), 237–249.

Swanson-Hysell, N.L., Ramezani, J., Fairchild, L.M., Rose, I.R., 2019. Failed rifting and fast drifting: Midcontinent Rift development, Laurentia's rapid motion and the driver of Grenvillian orogenesis. Bulletin 131 (5–6), 913–940.

Swenson, P., McWilliams, M., 1989. Paleomagnetic results from the Upper Cretaceous Maudlow and Livingston formations, Southwest Montana. Geophys. Res. Lett. 16 (7), 669–672.

Symons, D.T.A., Erdmer, P., McCausland, P.J.A., 2003. New 42 Ma cratonic North American paleomagnetic pole from the Yukon underscores another Cordilleran paleomagnetism-geology conundrum. Can. J. Earth Sci. 40 (10), 1321–1334. https://doi.org/10.1139/e03-047.

Tarduno, J.A., Cottrell, R.D., Smirnov, A.V., 2001. High geomagnetic intensity during the mid-cretaceous from Thellier analyses of single plagioclase crystals. Science 291 (5509), 1779–1783.

Tarduno, J.A., Cottrell, R.D., Smirnov, A.V., 2002. The cretaceous superchron geodynamo: observations near the tangent cylinder. Proc. Natl. Acad. Sci. 99 (22), 14020–14025.

Tauxe, L., Kent, D.V., 2004. A simplified statistical model for the geomagnetic field and the detection of shallow bias in paleomagnetic inclinations: was the ancient magnetic field dipolar? Geophys. Monogr. Ser. 145, 101–155.

Tauxe, L., Banerjee, S.K., Butler, R.F., van der Voo, R., 2010. Essentials of Paleomagnetism. University of California Press, Berkeley, CA.

Tauxe, L., Shaar, R., Jonestrask, L., Swanson-Hysell, N.L., Minnett, R., Koppers, A.A.P., et al., 2016. PmagPy: Software package for paleomagnetic data analysis and a bridge to the magnetics information Consortium (MagIC) database. Geochem. Geophys. Geosyst. 17, 2450–2463.

Tebbens, S.F., Cande, S.C., 1997. Southeast Pacific tectonic evolution from early Oligocene to present. J. Geophys. Res. Solid Earth 102 (B6), 12061–12084.

Thomas, D.N., Biggin, A.J., Schmidt, P.W., 2000. A palaeomagnetic study of Jurassic intrusives from southern New South Wales: further evidence for a pre-Cenozoic dipole low. Geophys. J. Int. 140 (3), 621–635.

Thompson, R., Clark, R.M., 1981. Fitting polar wander paths. Phys. Earth Planet. Inter. 27 (1), 1–7.

Torsvik, T.H., Eide, E.A., Redfield, T.F., Lundin, E., Smethurst, M.A., Ebbing, J., 2004. South Atlantic reconstructions: a self-consistent model. NGU Report 2004 (024), 100.

Torsvik, T.H., Müller, R.D., Van der Voo, R., Steinberger, B., Gaina, C., 2008. Global plate motion frames: toward a unified model. Rev. Geophys. 46 (3).

Torsvik, T.H., Rousse, S., Labails, C., Smethurst, M.A., 2009. A new scheme for the opening of the South Atlantic Ocean and the dissection of an Aptian salt basin. Geophys. J. Int. 177 (3), 1315–1333.

Torsvik, T.H., Smethurst, M.A., Meert, J.G., Van der Voo, R., McKerrow, W.S., Brasier, M. D., et al., 1996. Continental break-up and collision in the Neoproterozoic and Palaeozoic—a tale of Baltica and Laurentia. Earth Sci. Rev. 40 (3–4), 229–258.

Torsvik, T.H., Sturt, B.A., Ramsay, D.M., Bering, D., Fluge, P.R., 1988. Palaeomagnetism, magnetic fabrics and the structural style of the Hornelen Old Red Sandstone, Western Norway. J. Geol. Soc. 145 (3), 413–430.

Torsvik, T.H., Tucker, R.D., Ashwal, L.D., Carter, L.M., Jamtveit, B., Vidyadharan, K.T., Venkataramana, P., 2000. Late cretaceous India-Madagascar fit and timing of break-up related magmatism. Terra Nova 12 (5), 220–224.

Torsvik, T.H., Tucker, R.D., Ashwal, L.D., Eide, E.A., Rakotosolofo, N.A., De Wit, M.J., 1998. Late cretaceous magmatism in Madagascar: palaeomagnetic evidence for a stationary Marion hotspot. Earth Planet. Sci. Lett. 164 (1–2), 221–232.

Torsvik, T.H., Van der Voo, R., Preeden, U., Mac Niocaill, C., Steinberger, B., Doubrovine, P.V., et al., 2012. Phanerozoic polar wander, palaeogeography and dynamics. Earth Sci. Rev. 114 (3–4), 325–368.

Torsvik, T.H., van der Voo, R., 2002. Refining Gondwana and Pangea palaeogeography: estimates of Phanerozoic non-dipole (octupole) fields. Geophys. J. Int. 151 (3), 771–794.

Torsvik, T.H., Cocks, L.R.M., 2016. Earth History and Palaeogeography. Cambridge University Press.

Torsvik, T.H., Doubrovine, P.V., Domeier, M., 2014. Continental drift (paleomagnetism). In: Rink, W., Thompson, J. (Eds.), Encyclopedia of Scientific Dating Methods. Springer, Dordrecht.

Tucholke, B.E., Sibuet, J.-C., 2012. Problematic plate reconstruction. Nat. Geosci. 5 (10), 676–677.

Vaes, B., Gallo, L.C., van Hinsbergen, D.J., 2022. On pole position: causes of dispersion of the paleomagnetic poles behind apparent polar wander paths. Journal of Geophysical Research: SolidEarth 127 (4) e2022JB023953.

Vaes, B., Li, S., Langereis, C.G., van Hinsbergen, D.J., 2021. Reliability of palaeomagnetic poles from sedimentary rocks. Geophys. J. Int. 225 (2), 1281–1303.

Valencio, D.A., 1972. Paleomagnetism of the cretaceous Vulcanitas Cerro Colorado Formation of the Sierra de 10s Condores Group Provence of Cordoba,Argentina. Earth Planet. Sci. Lett 16–370.

Van Alstine, D.R., de Boer, J., 1978. A new technique for constructing apparent polar wander paths and the revised Phanerozoic path for North America. Geology 6 (3), 137–139.

Van de Lagemaat, S.H., Swart, M.L., Vaes, B., Kosters, M.E., Boschman, L.M., Burton-Johnson, A., Van Hinsbergen, D.J., 2021. Subduction initiation in the Scotia Sea region and opening of the Drake Passage: when and why? Earth Sci. Rev. 215, 103551.

Van der Voo, R., 1969. Paleomagnetic evidence for the rotation of the Iberian Peninsula. Tectonophysics 7 (1), 5–56.

Van der Voo, R., 1990a. The reliability of paleomagnetic data. Tectonophysics 184 (1), 1–9.

Van der Voo, R., 1990b. Phanerozoic paleomagnetic poles from Europe and North America and comparisons with continental reconstructions. Rev. Geophys. 28 (2), 167–206.

Van der Voo, R., French, R.B., 1974. Apparent polar wandering for the Atlantic-bordering continents: late Carboniferous to Eocene. Earth Sci. Rev. 10 (2), 99–119.

Van der Voo, R., van Hinsbergen, D.J.J., Domeier, M., Spakman, W., Torsvik, T.H., 2015. Latest Jurassic–earliest Cretaceous closure of the Mongol-Okhotsk Ocean: a paleomagnetic and seismological-tomographic analysis, late Jurassic margin of Laurasia–A Record of Faulting Accommodating Plate Rotation. Geol. Soc. Am. Spec. Pap. 589–606.

Van Hinsbergen, D.J.J., Straathof, G.B., Kuiper, K.F., Cunningham, W.D., Wijbrans, J., 2008b. No vertical axis rotations during Neogene transpressional orogeny in the NE Gobi Altai: coinciding Mongolian and Eurasian early cretaceous apparent polar wander paths. Geophys. J. Int. 173 (1), 105–126. https://doi.org/10.1111/j.1365-246X.2007.03712.x.

Van Hinsbergen, D.J., de Groot, L.V., van Schaik, S.J., Spakman, W., Bijl, P.K., Sluijs, A., et al., 2015. A paleolatitude calculator for paleoclimate studies. PLoS One 10 (6), e0126946.

Van Hinsbergen, D.J., Dupont-Nivet, G., Nakov, R., Oud, K., Panaiotu, C., 2008a. No significant post-Eocene rotation of the Moesian Platform and Rhodope (Bulgaria): implications for the kinematic evolution of the Carpathian and Aegean arcs. Earth Planet. Sci. Lett. 273 (3–4), 345–358.

Van Hinsbergen, D.J., Spakman, W., Vissers, R.L., van der Meer, D.G., 2017. Comment on "Assessing Discrepancies Between Previous Plate Kinematic Models of Mesozoic Iberia and Their Constraints" by Barnett-Moore Et Al. Tectonics 36 (12), 3277–3285.

Van Hinsbergen, D.J., Torsvik, T.H., Schmid, S.M., Maţenco, L.C., Maffione, M., Vissers, R.L., Spakman, W., 2020. Orogenic architecture of the Mediterranean region and kinematic reconstruction of its tectonic evolution since the Triassic. Gondwana Res. 81, 79–229.

Van Hinsbergen, D.J.J., Mensink, M., Langereis, C.G., Maffione, M., Spalluto, L., Tropeano, M., Sabato, L., 2014. Did Adria rotate relative to Africa? Solid Earth 5 (2), 611–629.

Vandamme, D., Courtillot, V., Besse, J., Montigny, R., 1991. Paleomagnetism and age determinations of the Deccan Traps (India): results of a Nagpur-Bombay Traverse and review of earlier work. Rev. Geophys. 29 (2), 159–190.

Veldkamp, J., Mulder, F.G., Zijderveld, J.D.A., 1971. Palaeomagnetism of Suriname dolerites. Phys. Earth Planet. Inter. 4 (5), 370–380.

Verma, R.K., Mital, G.S., 1974. Paleomagnetic study of a vertical sequence of traps from Mount Pavagarh, Gujrat, India. Phys. Earth Planet. Inter. 8 (1), 63–74.

Veselovskiy, R.V., Konstantinov, K.M., Latyshev, A.V., Fetisova, A.M., 2012. Paleomagnetism of the trap intrusive bodies in arctic Siberia: Geological and methodical implications. Izvestiya. Phys. Solid Earth 48, 738–750.

Veselovsky, R.V., Gallet, Y., Pavlov, V.E., 2003. Paleomagnetism of traps in the Podkamennaya Tunguska and Kotui River Valleys: implications for the post-Paleozoic relative movements of the Siberian and east European platforms. Izvestiya Phys. Solid Earth 39 (10), 856.

Vissers, R.L.M., Meijer, P.T., 2012b. Iberian plate kinematics and Alpine collision in the Pyrenees. Earth Sci. Rev. 114 (1–2), 61–83.

Vissers, R.L.M., Meijer, P.T., 2012a. Mesozoic rotation of Iberia: Subduction in the Pyrenees? Earth Sci. Rev. 110 (1–4), 93–110.

Vizán, H., 1998. Paleomagnetism of the lower Jurassic Lepáand Osta Arena formations, argentine Patagonia. J. S. Am. Earth Sci. 11 (4), 333–350.

Walderhaug, H.J., Eide, E.A., Scott, R.A., Inger, S., Golionko, E.G., 2005. Palaeomagnetism and 40Ar/39Ar geochronology from the South Taimyr igneous complex, Arctic Russia: a Middle-late Triassic magmatic pulse after Siberian flood-basalt volcanism. Geophys. J. Int. 163 (2), 501–517.

Watkins, N.D., 1973. Palaeomagnetism of the Canary Islands and Madeira. Geophys. J. Int. 32 (3), 249–267.

Watts, D.R., Watts, G.C., Bramall, A.M., 1984. Cretaceous and early Tertiary paleomagnetic results from the Antarctic Peninsula. Tectonics 3 (3), 333–346.

Wellman, P., 1975. Palaeomagnetism of two mid-Tertiary basaltic volcanoes in Queensland, Australia. In: Proceedings of the Royal Society of Queensland, 81, pp. 147–153.

Wellman, P., McElhinny, M.W., McDougall, I., 1969. On the polar-wander path for Australia during the Cenozoic. Geophys. J. Int. 18 (4), 371–395.

Whittaker, J.M., Muller, R.D., Leitchenkov, G., Stagg, H., Sdrolias, M., Gaina, C., Goncharov, A., 2007. Major Australian-Antarctic plate reorganization at Hawaiian-Emperor bend time. Science 318 (5847), 83–86.

Whittaker, J.M., Williams, S.E., Müller, R.D., 2013. Revised tectonic evolution of the Eastern Indian Ocean. Geochem. Geophys. Geosyst. 14 (6), 1891–1909.

Williams, S.E., Whittaker, J.M., Müller, R.D., 2011. Full-fit, palinspastic reconstruction of the conjugate Australian-Antarctic margins. Tectonics 30 (6).

Wright, N.M., Müller, R.D., Seton, M., Williams, S.E., 2015. Revision of Paleogene plate motions in the Pacific and implications for the Hawaiian-Emperor bend. Geology 43 (5), 455–458.

Wright, N.M., Seton, M., Williams, S.E., Mueller, R.D., 2016. The late cretaceous to recent tectonic history of the Pacific Ocean basin. Earth Sci. Rev. 154, 138–173.

Wu, L., Murphy, J.B., Quesada, C., Li, Z.X., Waldron, J.W., Williams, S., et al., 2021. The amalgamation of Pangea: Paleomagnetic and geological observations revisited. Bulletin 133 (3–4), 625–646.

Yang, Y.-T., Guo, Z.-X., Song, C.-C., Li, X.-B., He, S., 2015. A short-lived but significant Mongol-Okhotsk collisional orogeny in latest Jurassic–earliest cretaceous. Gondwana Res. 28 (3), 1096–1116.

Yi, Z., Liu, Y., Meert, J.G., 2019. A true polar wander trigger for the Great Jurassic East Asian Aridification. Geology 47 (12), 1112–1116.

Yokoyama, E., Brandt, D., Tohver, E., Trindade, R.I., 2014. Palaeomagnetism of the Permo-Triassic Araguainha impact structure (Central Brazil) and implications for Pangean reconstructions. Geophys. J. Int. 198 (1), 154–163.

Yonkee, W.A., Weil, A.B., 2015. Tectonic evolution of the Sevier and Laramide belts within the north American Cordillera orogenic system. Earth Sci. Rev. 150, 531–593.

Yuan, K., Van der Voo, R., Bazhenov, M.L., Bakhmutov, V., Alekhin, V., Hendriks, B.W. H., 2011. Permian and Triassic palaeolatitudes of the ukrainian shield with implications for Pangea reconstructions. Geophys. J. Int. 184 (2), 595–610.

Zhao, X., Robert, C., Yaoxiu, Z., Siyi, H., Haoruo, W., Guodun, K., Jie, W., 1994. Tertiary paleomagnetism of North and South China and a reappraisal of late Mesozoic paleomagnetic data from Eurasia: implications for the Cenozoic tectonic history of Asia. Tectonophysics 235 (1–2), 181–203.

Zheng, Z., Kono, M., Tsunakawa, H., Kimura, G., Wei, Q., Zhu, X., Hao, T., 1991. The apparent polar wander path for the North China Block since the Jurassic. Geophys. J. Int. 104 (1), 29–40.

Zhu, R., Pan, Y., He, H., Qin, H., Ren, S., 2008. Palaeomagnetism and 40Ar/39Ar age from a cretaceous volcanic sequence, Inner Mongolia, China: Implications for the field variation during the Cretaceous normal superchron. Phys. Earth Planet. Inter. 169 (1–4), 59–75.